Physical, Chemical, Biological, and Optical Oceanographic Conditions in the Labrador Sea in 2025

Stephanie Clay, Marc Ringuette, Emmanuel Devred, Kumiko Azetsu-Scott, Zeliang Wang, Blair Greenan, Chris Gordon, Carrie-Ellen Gabriel, Darlene Childs, Chantelle Layton, Guoqi Han

Bedford Institute of Oceanography
Fisheries and Oceans Canada
1 Challenger Drive
Dartmouth, Nova Scotia, Canada
B2Y 4A2

2026

Canadian Technical Report of Fisheries and Aquatic Sciences 3830

Fisheries and Oceans Canada | Pêches et Océans Canada

Canada

Canadian Technical Report of Fisheries and Aquatic Sciences

Technical reports contain scientific and technical information that contributes to existing knowledge but which is not normally appropriate for primary literature. Technical reports are directed primarily toward a worldwide audience and have an international distribution. No restriction is placed on subject matter and the series reflects the broad interests and policies of Fisheries and Oceans Canada, namely, fisheries and aquatic sciences.

Technical reports may be cited as full publications. The correct citation appears above the abstract of each report. Each report is abstracted in the data base *Aquatic Sciences and Fisheries Abstracts*.

Technical reports are produced regionally but are numbered nationally. Requests for individual reports will be filled by the issuing establishment listed on the front cover and title page.

Numbers 1-456 in this series were issued as Technical Reports of the Fisheries Research Board of Canada. Numbers 457-714 were issued as Department of the Environment, Fisheries and Marine Service, Research and Development Directorate Technical Reports. Numbers 715-924 were issued as Department of Fisheries and Environment, Fisheries and Marine Service Technical Reports. The current series name was changed with report number 925.

Rapport technique canadien des sciences halieutiques et aquatiques

Les rapports techniques contiennent des renseignements scientifiques et techniques qui constituent une contribution aux connaissances actuelles, mais qui ne sont pas normalement appropriés pour la publication dans un journal scientifique. Les rapports techniques sont destinés essentiellement à un public international et ils sont distribués à cet échelon. II n'y a aucune restriction quant au sujet; de fait, la série reflète la vaste gamme des intérêts et des politiques de Pêches et Océans Canada, c'est-à-dire les sciences halieutiques et aquatiques.

Les rapports techniques peuvent être cités comme des publications à part entière. Le titre exact figure au-dessus du résumé de chaque rapport. Les rapports techniques sont résumés dans la base de données *Résumés des sciences aquatiques et halieutiques.*

Les rapports techniques sont produits à l'échelon régional, mais numérotés à l'échelon national. Les demandes de rapports seront satisfaites par l'établissement auteur dont le nom figure sur la couverture et la page du titre.

Les numéros 1 à 456 de cette série ont été publiés à titre de Rapports techniques de l'Office des recherches sur les pêcheries du Canada. Les numéros 457 à 714 sont parus à titre de Rapports techniques de la Direction générale de la recherche et du développement, Service des pêches et de la mer, ministère de l'Environnement. Les numéros 715 à 924 ont été publiés à titre de Rapports techniques du Service des pêches et de la mer, ministère des Pêches et de l'Environnement. Le nom actuel de la série a été établi lors de la parution du numéro 925.

Canadian Technical Report of
Fisheries and Aquatic Sciences 3830

2026

Physical, Chemical, Biological, and Optical Oceanographic Conditions in the Labrador Sea in 2025

by

Stephanie Clay[1], Marc Ringuette[1], Emmanuel Devred[1], Kumiko Azetsu-Scott[1], Zeliang Wang[1], Blair Greenan[1], Chris Gordon[1], Carrie-Ellen Gabriel[1], Darlene Childs[1], Chantelle Layton[1], Guoqi Han[2]

[1]Bedford Institute of Oceanography
Fisheries and Oceans Canada
1 Challenger Drive
Dartmouth, Nova Scotia, Canada
B2Y 4A2

[2]Institute of Ocean Sciences
Fisheries and Oceans Canada
9860 West Saanich Rd
PO Box 6000
Sidney, British Columbia, Canada
V8L 4B2

© His Majesty the King in Right of Canada, as represented by the Minister of the Department of Fisheries and Oceans, 2026

This work is licensed under the Open Government Licence

Cat. No. Fs 97-6/3830E-PDF ISBN 978-1-100-01331-2 ISSN 1488-5379
https://doi.org/10.60825/a49g-ng87

Correct citation for this publication:

Clay, S., Ringuette, M., Devred, E., Azetsu-Scott, K., Wang, Z., Greenan, B., Gordon, C., Gabriel, C., Childs, D., Layton, C., Han, G. 2026. Physical, Chemical, Biological, and Optical Oceanographic Conditions in the Labrador Sea in 2025. Can. Tech. Rep. Fish. Aquat. Sci. 3830: vi + 65 p. https://doi.org/10.60825/a49g-ng87

TABLE OF CONTENTS

ABSTRACT V
RÉSUMÉ VI
1 INTRODUCTION 1
2 DATA AND METHODS 3
2.1 IN SITU SAMPLES COLLECTION 3
2.1.1 Missions 3
2.1.2 Core stations 4
2.1.3 Biological stations 5
2.1.4 Mission data presented in this report 5
2.2 PHYSICAL DATA 5
2.2.1 North Atlantic Oscillation (NAO) Index 6
2.2.2 Air temperatures 6
2.2.3 Sea surface temperature (SST) 6
2.2.4 Sea ice extent and concentration 6
2.2.5 Current transport 6
2.2.6 Argo data 7
2.2.7 Mixed Layer Depth and convection depth 7
2.3 CHEMICAL DATA 8
2.3.1 Transient tracers $SF6$ and CFC-12 8
2.3.2 Dissolved Inorganic Carbon (DIC), Total Alkalinity (TA), and pH 8
2.3.3 Dissolved oxygen 9
2.3.4 Spatio-temporal binning and trend calculations 9
2.4 BIOLOGICAL DATA 10
2.4.1 Surface temperature (0 to 100 m) 10
2.4.2 Nutrients 10
2.4.3 In situ chlorophyll-a concentration 10
2.4.4 Phytoplankton Taxonomic Groups 11
2.4.5 Phytoplankton Apparent Absorption Wavelength (PAAW) 11
2.4.6 Satellite-derived chlorophyll-a concentration and bloom metrics 12
2.4.7 Mesozooplankton 13
2.4.8 Spatio-temporal binning 14
2.4.9 Scorecards 14
2.5 ACCESS TO DATA PRODUCTS 15
3 RESULTS AND DISCUSSION 15
3.1 PHYSICAL DATA 15
3.1.1 North Atlantic Oscillation (NAO) Index 15
3.1.2 Surface air temperatures 16
3.1.3 Sea surface temperature (SST) 16
3.1.4 Sea ice 16

3.1.5 Current transport from CTD and altimetry data 17
3.1.6 Argo temperature and salinity 17
3.1.7 Shipboard observations of temperature, salinity, and density....18
3.1.8 Mixed Layer Depth and convection depth 20
3.2 CHEMICAL DATA 20
3.2.1 Transient tracers CFC-12 and SF_6 20
3.2.2 Dissolved Inorganic Carbon and pH....21
3.2.3 Dissolved oxygen....21
3.3 BIOLOGICAL DATA 21
3.3.1 Surface temperature (0 to 100 m) 21
3.3.2 Nutrients 22
3.3.3 In situ chlorophyll-a concentration....22
3.3.4 Phytoplankton Taxonomic Groups 23
3.3.5 Phytoplankton Apparent Absorption Wavelength 24
3.3.6 Satellite-derived chlorophyll-a concentration and bloom metrics 24
3.3.7 Mesozooplankton....25
4 SUMMARY....26
5 ACKNOWLEDGEMENTS....27
6 REFERENCES....28
7 TABLES 35
8 FIGURES 36
9 APPENDIX....65
10 OCEAN COLOUR POLYGON SEASONS....65

ABSTRACT

Clay, S., Ringuette, M., Devred, E., Azetsu-Scott, K., Wang, Z., Greenan, B., Gordon, C., Gabriel, C., Childs, D., Layton, C., Han, G. 2026. Physical, Chemical, Biological, and Optical Oceanographic Conditions in the Labrador Sea in 2025. Can. Tech. Rep. Fish. Aquat. Sci. 3830: vi + 65 p. https://doi.org/10.60825/a49g-ng87

This report summarizes the 2025 findings from the Atlantic Zone Off-Shelf Monitoring Program's (AZOMP) annual sampling of the AR7W line, covering the Labrador shelf and slope (AR7W-W), central Labrador Sea (AR7W-C), and Greenland shelf and slope (AR7W-E).

In 2025, physical conditions were marked by a slightly negative winter North Atlantic Oscillation (NAO) index, colder air temperatures in summer and warmer in other seasons, colder sea surface temperatures in spring and summer, below-normal sea ice extent, and a shallower convection depth. The water column was generally warmer and fresher than average in the upper 1000 m of the central Labrador basin. Current transport in spring-summer was slightly above normal on the Labrador shelf and below normal on the slope. Dissolved Inorganic Carbon (DIC) experienced a drop in concentration corresponding to an increase in pH. Dissolved oxygen remained near normal above 500 m and below normal at depth.

Nutrients remained below normal on the Labrador Shelf but returned to above-normal conditions elsewhere. Integrated chlorophyll-a was higher than normal on the Labrador Shelf corresponding to a higher-than-normal percentage of diatoms relative to total biomass, but lower in other regions where small flagellates were dominant. Satellite data revealed a late spring bloom and low annual chlorophyll-a on the Greenland Shelf, and a late fall bloom on the Labrador Shelf.

RÉSUMÉ

Clay, S., Ringuette, M., Devred, E., Azetsu-Scott, K., Wang, Z., Greenan, B., Gordon, C., Gabriel, C., Childs, D., Layton, C., Han, G. 2026. Physical, Chemical, Biological, and Optical Oceanographic Conditions in the Labrador Sea in 2025. Can. Tech. Rep. Fish. Aquat. Sci. 3830: vi + 65 p. https://doi.org/10.60825/a49g-ng87

Ce rapport résume les résultats de 2025 de l'échantillonnage annuel de la ligne AR7W du Programme de monitorage de la zone Atlantique au large du plateau continental (PMZAO), couvrant le plateau et le talus du Labrador (AR7W-O), le bassin central de la mer du Labrador (AR7W-C) et le plateau et le talus du Groenland (AR7W-E).

En 2025, les conditions physiques ont été marquées par un indice Oscillation nord-atlantique (ONA) hivernal légèrement négatif, des températures de l'air plus froides en été et plus chaudes les autres saisons, des températures de surface de la mer plus froides au printemps et en été, une étendue de glace de mer inférieure à la normale et une profondeur de convection moins profonde. La colonne d'eau était généralement plus chaude et plus fraîche que la moyenne dans les 1 000 premiers mètres du bassin central de la mer du Labrador. Le transport actuel au printemps et à l'été était légèrement supérieur à la normale sur le plateau continental de la mer du Labrador et inférieur à la normale sur le talus. Le carbone inorganique dissous (CID) a connu une baisse de concentration correspondant à une augmentation du pH. L'oxygène dissous est demeuré près de la normale au-dessus de 500 m et inférieur à la normale en profondeur.

Les nutriments sont restés inférieurs à la normale sur le plateau du Labrador, mais sont revenus à des conditions supérieures à la normale ailleurs. La chlorophylle-a intégrée était plus élevée que la normale sur le plateau du Labrador, ce qui correspond à un pourcentage de diatomées relative à la biomasse total supérieur à la normale, mais plus faible dans les autres régions où les petits flagellés étaient dominants. Les données satellitaires ont révélé une floraison printanière tardive et une faible concentration moyenne annuelle en chlorophylle-a sur le plateau du Groenland, ainsi qu'une floraison tardive sur le plateau du Labrador.

1 INTRODUCTION

The Labrador Sea is a deep basin nested between Labrador and Greenland with a cyclonic circulation pattern that leads to the mixing of Arctic and North Atlantic waters. The Baffin Island and Labrador currents transport cold and less-saline Arctic water southward along the Canadian coast (Wang et al. 2016). On the eastern side, the West Greenland Current brings warmer, more-saline waters northward, along the Greenland coast into the Baffin Bay, where it meets the Labrador Current (see Lozier et al. (2019) and Yashayaev and Loder (2017) for a detailed description of the Labrador Sea circulation). An ocean process called deep convection plays a vital role in the formation of dense water, which supplies oxygen and carbon to the deep layers of the ocean. In this process, warm, buoyant water at the surface cools, becomes denser, and sinks to deeper layers (down to 2500 m). This vertical movement is a critical component of ocean circulation. The Labrador Sea is one of the few areas in the global ocean where surface water is exchanged with the deep ocean, hence it has an important role in biogeochemical cycling in the Labrador Sea, and enhances the entrainment of gases such as oxygen and carbon dioxide into the deep water from the atmosphere, as well as from surface freshwater.

Since 1990, as part of the World Ocean Circulation Experiment (WOCE), Fisheries and Oceans Canada's (DFO) Ocean and Ecosystem Sciences Division (OESD) at the Bedford Institute of Oceanography (BIO) has carried out an annual occupation, usually in the spring, of the AR7W (Atlantic Repeat Hydrography Line 7 West) oceanographic section across the Labrador Sea (Figure 1). Soon after its inception, the program morphed into the Atlantic Zone Off-shelf Monitoring Program (AZOMP), following the OESD's overarching objectives to: 1) characterize and understand the causes of ocean variability at inter-annual and inter-decadal scales; 2) provide adequate data to monitor the health of the marine ecosystem and support decision-making based on scientific evidence; and 3) to build historical databases to address future issues. The program also contributes to the international Global Climate Observing System (GCOS) and the Climate Variability (CLIVAR) component of the World Climate Research Program (WCRP), the Global Ship-based Hydrographic Investigations Program (GO-SHIP), the Global Ocean Acidification Observing Network (GOA-ON), the United Nations Sustainable Development Goals 14.3.1 (UN SDG14.3.1), the Global Ocean Data Analysis Project (GLODAP, https://glodap.info), the Surface Ocean CO_2 Atlas (SOCAT, https://socat.info), and it reports annually with an environmental synopsis to the Northwest Atlantic Fisheries Organization (NAFO). Integration of these data into GLODAP and SOCAT contributes to the "Global Carbon Budget", (https://globalcarbonbudget.org/gcb-2025), which provides a key benchmark for climate change policy (McKinley 2025). Chlorophyll-a concentration and Particulate Organic Carbon data are distributed to the Ocean Colour Climate Change Initiative (OC-CCI) and Eumetsat for calibration and evaluation of satellite-derived products (Sathyendranath et al. 2019). Many of these datasets are also used in research publications (e.g. Barrett et al. (2025), Leist et al. (2026), Devred et al. (2025), Li et al. (2026), Cyr et al. (2024), Kam et al. (2024), Pollara et al. (2024)). The annual AZOMP multidisciplinary survey of the Labrador Sea primarily consists of AR7W occupations and deployments/recoveries of moorings and Argo floats. The ideal timing of the mission in May aims to capture the fading winter-deep-convection signal and the beginning of the phytoplankton bloom and productivity season, while avoiding possible sea ice on the Labrador shelf early in the spring. With nearly three decades of measurements, the time series allows examination of decadal trends in all key ecosystem variables (i.e, temperature, nutrients, plankton biomass and abundance).

Shipboard observations play a crucial role in studying changes in the ocean, complementing the valuable data provided by the Argo program and satellite ocean colour data. While satellite sensors offer near-surface ocean data at a high spatial and temporal resolution over the entire

globe, and Argo floats offer a large, three-dimensional view of the upper ocean, shipboard observations provide a more comprehensive, precise, and detailed picture. Ships can carry a wider array of instruments, allowing for measurements of various physical, chemical, and biological properties. This includes high-resolution sampling of the water column, collection of chemical and biological samples, and direct observations of surface phenomena. In addition, shipboard observations offer flexibility, adaptability, and can be strategically deployed to investigate specific regions or phenomena of interest. This targeted approach allows for focused investigations and the collection of unique datasets that may not be captured by satellite sensors or Argo floats. Ships can also carry out long-term time-series measurements at fixed locations, providing crucial insights into the variability and trends of ocean properties over time, and this is one of many merits of the on-going AZOMP program for the AR7W line. Additionally, the samples collected during the program can be used to validate satellite and Argo data, and are crucial to the continuing calibration and improvement of satellite data within the Labrador Sea.

The upper layers of the Labrador Sea exhibit significant interannual variability in temperature and salinity. These fluctuations are primarily driven by three key factors: 1) atmospheric forcing, 2) variations in the warm and saline inflows of the West Greenland Current, and 3) changes in freshwater input from both liquid and ice sources originating from the Arctic and Greenland. Seasonal cycles in each of these forcing mechanisms induce a pronounced seasonal cycle in the upper ocean properties of the Labrador Sea.

During the early 1990s, deep winter convection within the Labrador Sea resulted in the upper two kilometers of the water column being filled with cold, fresh water. However, milder winters in recent decades have led to more limited formation of mode waters, which have also become warmer, saltier, and less dense compared to those observed a decade and a half ago. This trend experienced an abrupt shift during the exceptionally cold winter of 2008, when deep convection extended to a depth of 1600 meters. The specific environmental conditions that facilitated this deep convection event in 2008 have been comprehensively documented by Yashayaev and Loder (2009).

About one quarter of the carbon dioxide (CO_2) released by human activities is taken up by the global ocean (Sabine et al. 2004), altering ocean chemistry, and correspondingly, the marine carbonate system. The Labrador Sea hosts a strong “solubility pump”, whereby anthropogenic CO_2 sequestrated from the atmosphere is transported to the deep ocean through chemical and physical processes. The dissolution of anthropogenic CO_2 has decreased global ocean pH by 0.1 units over the past 200 years, resulting in a 30% increase in acidity (Caldeira and Wickett 2003). If global emissions of CO_2 remain at their present rate, ocean pH is predicted to drop by an additional 0.3 units by 2100. The oceans have not experienced such a rapid pH decrease (ocean acidification), or one of such a high magnitude, for at least 20 million years (Feely et al. 2004), raising serious concerns about the ability of marine ecosystems to adapt. The major impact of decreasing pH will be felt by organisms that form calcium carbonate ($CaCO_3$) shells and skeletons, because rising acidity increases the solubility of $CaCO_3$. Since $CaCO_3$ shells and skeletons are naturally more soluble at lower temperatures and higher pressures, high latitudes and deep water ecosystems, such as the one encountered in the Labrador Sea, are more vulnerable to the added stress of ocean acidification than those at intermediate latitudes. Ocean acidification also influences the capacity of the ocean to take up CO_2 from the atmosphere. Furthermore, increasing precipitation and freshwater input from land under a warming climate may accelerate hydrological changes in high-latitude oceans, which could amplify these problems.

Transient tracers dichlorodifluoromethane (CFC-12) and sulfur hexafluoride (SF_6) are used to study ocean circulation, ventilation, and mixing processes. Specifically, they are used to study

ventilation rates and age determination of water masses. As the Labrador Sea is the site of direct uptake of these tracers by deep convection during winter, these measurements provide the boundary conditions for the global network of tracer observations, which are used to trace ocean circulation pathways such as spreading of North Atlantic Deep Water. These tracers are also used to estimate anthropogenic CO_2 storage and track their changes (Haine and Hall 2002; Hall et al. 2002; Raimondi et al. 2021).

The AR7W transect crosses two productive shelves (Labrador and Greenland shelves) and the central Labrador Sea, where phytoplankton production is subject to local forcing (eddies, mixing, stratification) that drive phytoplankton biomass and community structure. In the central Labrador Sea, light limits primary production for most of the year (Harrison and Li 2008; Fragoso et al. 2016), while a shallow mixed layer, and relatively low nitrate concentration, limit phytoplankton growth on the Labrador shelf following the spring bloom. Phytoplankton growth, in particular diatoms, also seemed to be limited by availability of silicate in the central Labrador Sea (Harrison and Li 2008). These conditions support the emergence of small flagellates such as *Phaeocystis pouchetii* in the northern and eastern region of the Labrador Sea, which can form large blooms under favorable conditions (Fragoso et al. 2016). In recent years, large blooms of *Phaeocystis spp.* have also been observed in the western part of the central Labrador Sea (Devred et al. 2024). The Labrador shelf, influenced by Arctic waters, is dominated by polar diatom species (*Thalassiosira spp.*, *Chaetoceros spp.*, and *Bacteriosira bathyomphala*) and species associated with sea-ice (*Porosira glacialis* and *Fossula arctica*). Primary production patterns and mesoscale features leave their imprint on the mesozooplankton distribution and abundance (Yebra et al. 2009). One species of copepod, *Calanus finmarchicus*, dominates the mesozooplankton biomass throughout the central region of the Labrador Sea, while on the shelves, two Arctic *Calanus* species, *C. glacialis* and *C. hyperboreus*, are equally important (Head et al. 2003). *C. finmarchicus* abundance shows regional variations that are generally consistent from year-to-year and are related to differences in the timing of life-cycle events, which are influenced by environmental conditions, including spring bloom dynamics.

This report describes the physical, chemical, and biological state of the Labrador Sea in 2025. Data presented in this report come from: 1) the annual survey carried out over a 3-week period, typically between early May and early June depending on vessel and crew availability; 2) satellite remote-sensing of daily observations of ocean colour converted into chlorophyll-a concentration (chl-a), 3) Argo float data for temperature, salinity, and dissolved oxygen when available, and 4) publicly-available datasets provided by various organizations to summarize the physical conditions of the region (Table 1).

2 DATA AND METHODS

2.1 In situ samples collection

2.1.1 Missions

The AZOMP sampling period was dictated in the past by the Canadian Coast Guard operational constraints and ship availability, which was challenging in the 2010s due to mechanical issues with the research vessel CCGS Hudson. From 2008 to 2018 (except 2013), AZOMP missions started slightly early each year, with about 25 days difference over the entire period (Figure 2). The timing of the mission has been highly variable since 2019 with the chartering of foreign oceanographic vessels, and the 2017 and 2021 missions were skipped entirely due to the lack of ship availability. In addition, the COVID pandemic in 2020 prevented the chartering of foreign vessels and the mission was only possible on the CCGS Amundsen at a later date in July – August.

The occupation of AR7W in 2025 was conducted as part of a collaborative effort within the Transforming Climate Action subgroup *Uncertain-Sea*, whose overarching objective is to investigate carbon transfer processes in the Labrador Sea. Particular emphasis was placed on improving our understanding of the recurrent large-scale blooms of *Phaeocystis spp.* in the Labrador Sea and their influence on carbon fixation and transport through the lower trophic food web and the northwestern Atlantic Ocean.

The mission (LAT2025-146), conducted aboard IFREMER's research vessel *R.O. L'Atalante*, commenced on April 25th 2025 from the Bedford Institute of Oceanography and concluded at the same port on May 27th 2025. During the 32-day expedition, the vessel traveled 3503.7 nautical miles and visited 50 stations, resulting in 212 unique deployments and more than 5000 individual measurements.

For the second consecutive year, stations planned for the Greenland Shelf region could not be occupied due to the presence of drifting pack ice, poor visibility, and forecasts of severe storm conditions in the area.

2.1.2 Core stations

The core stations (Figure 1) remain the priority of the monitoring program to ensure geographical consistency over time when reporting on the data. The main goal of the sampling is to obtain a complete suite of measurements at selected locations from surface to bottom to characterize the physical and chemical properties of the entire water column, while measurements of biological properties are restricted to the upper layers (0 to 100 m).

The CTD (Conductivity, Temperature, Depth)-rosette system is used to collect water at 24 selected depths distributed over the entire water column using 12 L Niskin bottles and profiles of physical and biogeochemical properties are recorded using a core of twinned sensors for temperature, salinity and oxygen, as well as additional sensors to measure fluorescence (both chl-a and Colored Dissolved Organic Matter (CDOM)), pH, light attenuation, Photosynthetically Active Radiation (PAR) and current velocity (LADCP). CTD profiles are collected on both the downcast and upcast from surface to near bottom (often several thousand meters deep). The CTD-rosette is first lowered down to 10 m for 10 minutes due to the requirement for an underwater acclimation period at depth for the sensors, and this part of the cast is removed during quality control processing. Following the acclimation period, the CTD-rosette system is brought as close as possible to the surface but, partly because of the ship's movements, it does not reach the theoretical 0 m depth. Surface values are obtained by linear extrapolation of the temperatures at the two depths closest to the surface. The CTD is then lowered to within 7 to 12 meters of the bottom depending on sea conditions. The speed of descent is around 0.5 m/s for the top and bottom 200 m and 1 m/s otherwise. At the bottom, the CTD is stopped to acclimate for at least one minute before beginning its ascent (Mitchell et al. 2002). Similarly on the upcast, the CTD is stopped to acclimate for at least one minute at each depth where one or more bottles are closed. The CTD sensor data is recorded from the scan that occurs at the moment the bottle is closed to use in conjunction with the water sample data (see section 2.4.1). The full downcast CTD profiles are presented in conjunction with the physical data (section 2.2) as the downcast is not interrupted to close the bottles. Data for pressure, temperature, conductivity, salinity, and dissolved oxygen undergo rigorous calibration and quality control to meet WOCE standards. This process utilizes data from water samples (e.g., Autosal salinity and Winkler titration), SBE35 temperature recorders, and laboratory calibrations.

When the CTD-rosette returns to the deck, water samples are immediately collected to measure transient gases (CFC-12 and SF_6), oxygen, partial pressure of carbon dioxide (pCO_2), Dissolved Inorganic Carbon (DIC), total alkalinity (TA), pH, nutrients, and salinity. In addition to the

previous measurements, four bottles located in the surface-layer (2, 25, 50 and 100 m) are sampled for chl-a and cell abundance (Flow Cytometry). The 2 m depth is sampled for phytoplankton absorption and pigment composition, particulate organic carbon, and CDOM absorption. The collection of water from the Niskin bottles is carried out as listed previously (i.e., gases first and phytoplankton last) from bottom to surface waters to minimize the loss of transient tracers and other gases during sampling. All variables were sampled and analyzed following GO-SHIP protocols (Mitchell et al. 2002; Hood et al. 2010). In addition to water sampling from the Niskin bottles, mesozooplankton are collected in vertical net hauls in the upper 100 m using a 0.75 m diameter ring net fitted with a 200 µm mesh, and 0.5 m diameter ring net with a 76 µm mesh size. A detailed description of the processing of the physical oceanographic data is presented in Yashayaev et al. (2021).

When time allows, additional stations are added between core stations in order to increase the spatial resolution of the sampling. However, at these stations only measurements from the sensors located on the CTD-Rosette are recorded and water is not collected unless requested by programs outside the core program. At these stations, the CTD-Rosette system is lowered to the ocean bottom to profile the entire water column.

2.1.3 Biological stations

The purpose of these stations is to increase the vertical resolution compared to core stations where only four depths are sampled over the first 100 m, and to carry out Photosynthesis-Irradiance (P-I) 14C-uptake experiments with phytoplankton (water) samples. In these experiments, 20 aliquots of phytoplankton from two depths (surface and close to the deep chl-a maximum) are incubated with 14C-bicarbonate at in situ temperatures and 20 light levels (+ 3 dark bottles) for approximately 3 hours. The P-I measurements are used to estimate the rate of primary production according to Platt and Jassby (1976). The timing of the 14C experiments at the biological stations is more critical than the exact location, so the vessel is stopped mid-morning at any location on the AR7W transect in order to start the incubations around noon (Halifax time) to ensure consistency of the method. Because the biological stations focus on the upper layers of the water column, the CTD sensor is only lowered to 200 m, allowing for a greater vertical resolution of all the biogeochemical parameters. Bottles are closed at 2, 10, 20, 30, 40, 50, 60, 80, 100, and 150 m, with an additional bottle at the depth of the deep chl-a maximum, as revealed by the in situ fluorescence sensor. In general, a total of seven biological stations are sampled, which are spread along the AR7W transect: two on the Labrador shelf, three in the central Labrador Sea, and two on the Greenland shelf.

2.1.4 Mission data presented in this report

In the current report, we present the data for a subset of the in situ measurements listed in this subsection, which includes: CTD data (temperature, salinity, and density), transient tracers, TIC, pH, nutrients, chl-a, and mesozooplankton abundances. The remaining datasets are available from the Canadian Integrated Ocean Observing System (CIOOS, https://cioos.ca) and Open Data (https://search.open.canada.ca). Links can be provided upon request to the corresponding author.

2.2 Physical data

This section documents the physical data presented in this report which complements the shipboard CTD data described above. The reference period used to calculate climatological means and standard deviations (SD) is 1991-2020, as long as data is available (1993-2020 for current transports, and 2002-2020 for Argo data).

2.2.1 North Atlantic Oscillation (NAO) Index

The NAO index data were downloaded from the Physical Sciences Laboratory at NOAA (Table 1). The winter (January to March) NAO index anomalies presented in this report were calculated by subtracting the climatology (1991-2020) from the winter NAO index.

2.2.2 Air temperatures

Air temperature data for this study were obtained from the NCEP Reanalysis dataset, a joint project by the National Centers for Environmental Prediction (NCEP) and the National Center for Atmospheric Research (NCAR) (Table 1). This dataset provides a comprehensive analysis of historical surface air temperature since 1948, along with near-real-time analyses of the current atmospheric state (Kalnay et al. 1996).

To investigate air temperature variations over the central Labrador Sea, as defined by Yashayaev (2007), we focused on the area within 150 km of the AR7W line where bottom depth exceeds 3300 m (P3300, the yellow polygon in Figure 1). Air temperature anomalies were computed by subtracting the seasonal climatologies (1991-2020) from the data, offering a clear view of deviations from long-term averages. Seasons were defined as follows: January to March (winter), April to June (spring), July to September (summer), and October to December (winter).

2.2.3 Sea surface temperature (SST)

The sea surface temperature (SST) data used in this study were sourced from the Hadley Centre Sea Ice and Sea Surface Temperature (HadISST) dataset (Rayner et al. 2003). HadISST is a widely recognized gridded dataset that provides historical records of global SST and sea ice concentration. HadISST combines observations from various sources, including ships, buoys, and satellites. It employs statistical interpolation methods to create a comprehensive global coverage of SST and sea ice data. Areas covered by sea ice are assigned a value of -1.8 °C. The HadISST dataset spans the period from 1870 to the present, offering a valuable long-term perspective on oceanic conditions. It is a crucial resource for understanding historical and ongoing changes in global sea surface temperatures and sea ice extent. The data were downloaded from Met Office Hadley Centre observations datasets (Table 1). Similar to the air temperature analysis, the seasonal SST anomalies were derived by subtracting the 1991-2020 climatologies from the data, where seasons are defined as in section 2.2.2 and analyses are focused on the area within the P3300 polygon (Figure 1).

2.2.4 Sea ice extent and concentration

Sea ice concentrations derived from satellite passive microwave data since late 1978 were obtained from the U.S. National Snow and Ice Data Center (Table 1) (Cavalieri et al. 1996; Fetterer et al. 2017). Monthly sea ice concentration climatologies were calculated for the reference period 1991-2020, and standardized anomalies were calculated for 2025 using this reference period. Ice extent was defined as the area in which sea ice concentration was at least 15%. Note that the report on Labrador Sea conditions in 2024 (Clay et al. 2026) used version 3.0 of this sea ice product, and the current report uses version 4.0.

2.2.5 Current transport

The geostrophic currents normal to the AR7W transect (positive southeastward) and relative to the sea surface were calculated from the temperature and salinity data. The daily altimetric sea surface currents, obtained from the level-4 1/8-degree gridded altimetry product distributed by CMEMS (E.U. Copernicus Marine Service Information (2026), Table 1), were averaged over the CTD period, and the averaged altimetric sea surface currents normal to the AR7W transect

were added onto the geostrophic currents to obtain total currents. Transport was then calculated from the 700-m isobath to the 3000-m isobath to represent the Labrador Current over the continental slope, and inshore to the 700-m isobath to represent the Labrador Current over the Labrador Shelf. The climatological average and SD of the slope and shelf transports were calculated over the 1993-2020 reference period, and used to calculate standardized anomalies of transports.

2.2.6 Argo data

The Argo program is a global array of about 4000 free-drifting profiling floats that measure the temperature and salinity of the upper 2000 m of the ocean (Table 1, Wong et al. (2020)). Argo floats are essentially robotic ocean observers that are deployed from ships to autonomously collect and report data for their entire lifetime, typically about 5 years. The main advantage of Argo floats is their ability to take measurements all year long with a large spatial distribution when compared to ship-based measurements. Limitations of this approach include the absence of control of the sampling location, and a sampling depth limit of 2000 m (however, deep Argo floats with depths ranging from 3500 to 6000 m are currently being deployed).

The float sinks to a predetermined depth (typically around 1000 meters - as a result, they do not sample on the shelves) and drifts with the ocean currents. After a set period (usually 10 days), the float descends to 2000 m using a bladder system to regulate its density (and hence its buoyancy), and then begins its ascent toward the surface. During its ascent, the float measures temperature, conductivity, and pressure of the water column. Some biogeochemical floats are further equipped with oxygen, chlorophyll fluorescence, particulate backscatter, pH, nitrate, or radiometry sensors. Once at the surface, the float transmits the collected data via Iridium satellite to scientists on land where it is openly available within 24 hours. The float then repeats this cycle, providing a continuous stream of valuable oceanographic data.

Argo data collected from the Labrador Sea beginning in 2002 was downloaded using the Python package *argopy* (Maze and Balem 2020). To investigate changes in ocean conditions, we focused on four depth ranges within the water column: 0-50 dbar, 100-500 dbar, 500-1000 dbar, and 1000-2000 dbar. Salinity data (on the practical salinity scale, PSS-78) and temperature were retrieved for each depth range. A climatology was established by averaging values over the period 2002-2020. The climatology was either calculated within 1 degree by 1 degree grid boxes (Figures 11-13) or monthly means within the P3300 polygon (Figures 14-15), using all available Argo float profiles after standard quality control processing. The anomaly for 2025 was then calculated as the deviation of 2025 conditions from the appropriate climatological baseline.

2.2.7 Mixed Layer Depth and convection depth

The ocean mixed layer depth (MLD) is the depth of the near-surface layer in which turbulence generated by winds, waves, and buoyancy forcing has homogenized properties such as temperature, salinity, and density, resulting in relatively uniform water characteristics from the surface to the base of the mixed layer. The MLD is typically identified from hydrographic profiles using a temperature or density threshold and varies seasonally, ranging from tens of meters during strongly stratified summer conditions to several hundred meters during winter. In regions that experience deep winter convection, such as the Labrador Sea, surface cooling and storm-driven mixing can erode stratification to much greater depths, causing dense surface waters to overturn and sink. During these periods, the mixed layer may deepen to 1000-2000 m or more, and the maximum winter MLD is often used as a proxy for the depth of convection and the formation of Labrador Sea Water. Although the terms are closely related, the mixed layer depth is a diagnostic property describing the depth of the homogenized surface layer at a given time, whereas the depth of deep convection refers to the maximum penetration of convective

overturning. Consequently, the deepest convection reached during a winter may be greater than the mixed layer depth observed later in the season after restratification has begun. In most parts of the global ocean, mixed layers are typically less than 200 m deep, whereas in the Labrador Sea winter convection can connect the surface directly with the ocean interior over depths exceeding 1500 m, making it one of the most important regions for ocean ventilation and intermediate water-mass formation.

To estimate the 2025 winter convection depth in the Labrador Sea, we analyzed CTD data from the AR7W line survey conducted in 2025. Two distinct methodologies were employed to estimate convection depth for each individual CTD cast within the P3300 polygon (Figure 1): 1) The Mixed Layer Depth (MLD) Approach: We calculated the MLD using an adaptation of the 'ra_mld.m' MATLAB function (Patel 2025). The temperature difference criterion within the function was set to 0.29 °C. This approach assumes the base of the mixed layer corresponds to the depth of active convective process. 2) The Vertical Temperature Gradient Maximum Approach: This method postulates that the depth of maximum vertical temperature gradient coincides with the deepest extent of convective mixing.

To cross-validate our estimates of MLD and examine long-term trends, MLD was also calculated for each Argo profile following Patel (2025), using the temperature difference criterion with a value to 0.3 °C. Stratification index was also calculated for each profile, defined as the difference in density between the surface and at 200 dbar, following Yamaguchi and Suga (2019). When using Argo data, which is resolved on a finer timescale than the shipboard CTD data, we define the convection depth of a given year as the maximum monthly median of the mixed layer depth for that year.

2.3 Chemical data

2.3.1 Transient tracers SF_6 and CFC-12

Prior to analysis, seawater samples from the rosette were drawn directly into 250 mL glass syringes and were stored at approximately 4 °C in a low-temperature incubator for up to 12 hours. Immediately before analysis, the samples were warmed to approximately 20 °C in a water bath then injected into the purge vessel of a custom-made purge-and-trap system, where dissolved gases were stripped from the sample in a stream of ultra-high-purity nitrogen with a flow rate of 140 mL per minute. The SF_6 and CFC-12 gases were quantitatively retained in a trap comprised of 30 cm of 1/16" diameter stainless steel tubing packed with 100–120 mesh Carboxen 1000, held at -70 °C over liquid nitrogen. After each 7 minute purge cycle, the trap was heated to 180 °C with a low-voltage electric current and the desorbed gases directed to a Varian gas chromatograph equipped with an electron-capture detector. SF_6 and CFC-12 were separated on a one-meter pre-column packed with Porasil B and a three-meter main column packed with Molecular Sieve 5A held isothermally at 100 °C. Total run-time was 11.5 minutes for each sample. The chromatographic sample peaks were quantified with Varian Galaxie software and the analytical system calibrated at least once each day using an air standard supplied by the Climate Monitoring and Diagnostics Laboratory of the National Oceanic and Atmospheric Administration (CMDL/NOAA), Boulder, Colorado. Analytical precision, as determined by repeated standard injections, was around ± 2% for SF_6 and ± 0.7% for CFC-12. (Punshon et al. 2016)

2.3.2 Dissolved Inorganic Carbon (DIC), Total Alkalinity (TA), and pH

Samples for Dissolved Inorganic Carbon (DIC) and Total Alkalinity (TA) were collected in 500 mL borosilicate glass bottles. Before 2013, DIC and TA were measured onboard within six hours of sample collection. After 2013, samples were preserved with mercuric chloride following

best practices described by Dickson et al. (2007) and stored at room temperature until analysis at BIO's chemical laboratory. DIC was measured using gas extraction and coulometric titration with photometric endpoint detection (Johnson et al. 1987). TA was measured by open-cell potentiometric titration with full-curve Gran Point determination using a Titrando dosimat with Tiamo software, along with a sample delivery system that was built in-house. Certified Reference Material (supplied by Professor Andrew Dickson, Scripps Institution of Oceanography, San Diego, USA) was analyzed in duplicate every 20 samples to ensure accuracy.

Spectrophotometric pH measurements, using an Agilent 8453 UV-Vis spectrophotometer, began in 2009. Samples were collected in 60 mL borosilicate glass tubes, stored at 4 °C, and analyzed onboard within six hours of collection following best practices (Dickson et al. 2007). Detailed methods for TIC, TA, and pH analyses are described in Punshon et al. (2019) and Raimondi et al. (2019).

pH values were calculated from DIC and TA measurements using CO2SYS (Lewis et al. 1998), applying the dissociation constants of Lueker et al. (2000), and are presented here to ensure consistency throughout the study period. However, in 2012 and 2014, pH values were derived using direct pH measurements and DIC due to a TA instrument failure. All pH values are reported on the total scale.

2.3.3 Dissolved oxygen

Dissolved oxygen concentrations were determined using the Winkler titration method (Langdon 2010), where oxygen is chemically fixed upon sampling, converted to iodine, and quantified using a thiosulfate titration. Dissolved oxygen samples for Winkler titration were collected at all sampled depths at each station, providing full-depth coverage of the water column. The full coverage supports the identification of the ventilation structure, calibration of oxygen sensors, and aids the validation of transient tracer measurements.

Spatial patterns of dissolved oxygen were cross-validated with Argo data in the 100-500 dbar layer, using the same 1x1 degree gridding method as described in section 2.2.6.

2.3.4 Spatio-temporal binning and trend calculations

For tracers, TIC, and pH data, statistics were limited to samples collected within 150 to 500 m depth and stations from 56°N to 59.1°N along the AR7W line. These samples were considered representative of the Newly Ventilated Labrador Sea Water (NV-LSW) as they are less impacted by seasonal variability than surrounding waters (Azetsu-Scott et al. 2003). Time series of dissolved oxygen data were limited to two water masses: the NV-LSW, and the North East Atlantic Deep Water (NEADW), which is defined by a density range of 36.96-37.1 $kg\ m^{-3}$ referenced to 2000 dbars within 56°N to 59.1°N (Yashayaev 2007).

Tracer, TIC, pH, and dissolved oxygen data were averaged annually over the NV-LSW (and over the NEADW for dissolved oxygen) and presented as time series in Figures 21, 22, and 24. Linear trends were calculated for SF_6, TIC, and pH using an ordinary least squares method, as each exhibited monotonic trends over time.

2.4 Biological data

2.4.1 Surface temperature (0 to 100 m)

For the surface temperature measurements coinciding with the biological data, we used the temperature data recorded at the discrete depths at which water was collected for biological sampling during the CTD upcast (see section 2.1).

2.4.2 Nutrients

Nutrient measurements were made using a SEAL Analytical continuous-flow AutoAnalyzer 3 (AA3) and concentrations are expressed in micromoles per liter. The analytical methods have been modified from the historically used Technicon II: Technicon for Seawater Analysis (Silicate 186 72W, Phosphate 155 71W, Nitrate/Nitrite 158 71W) (Kérouel and Aminot 1997) so as to remain compatible with methods described in the nutrient section of The GO-SHIP Repeat Hydrography Manual (Becker et al. 2020). Duplicate nutrient samples were drawn into 10 ml collection vials directly from the rosette without using tubing, with technicians wearing vinyl gloves to avoid contamination. Since 2024, samples were filtered through a 0.2 µm mesh filter to further align our methods with the GO-SHIP protocols, where the filtration of nutrient samples is recommended for coastal and highly productive areas. This procedure aims to reduce the variance between replicate samples by diminishing the impact of cell lysis and bacterial activity between sampling and process time (Reed et al. 2022). Samples were stored at 4 °C and analyzed within 12 hours. Five dissolved inorganic nutrients were analyzed, namely, nitrate plus nitrite (NO_3 + NO_2), nitrite (NO_2), phosphate (PO_4), silicate (SiO_4), and ammonium (NH_4). Note that in 2023 and 2024, nutrients were frozen and analyzed upon return to BIO due to a lack of laboratory space in the fishing trawler CCGS Jacques Cartier preventing the installation of the auto-analyser.

The instrument was calibrated for every analytical run, using a six-point calibration curve from pre-made solutions diluted using artificial seawater of same salinity as the samples, distributed over the concentration range for each nutrient. The analysis was followed by a drift standards analysis and blank samples to determine the method's detection limits. The baseline was re-assessed every 12 sample duplicates (i.e., every 6 samples). The pH of the imidazole buffer was monitored to ensure optimal pH levels (i.e. approximately 7.83-7.85) for the nitrate plus nitrite analyses, and adjusted as needed using hydrochloric acid, thus improving the lifespan and stability of the cadmium reduction column. Ultimately, this method diminished drift issues observed in the past between analytical runs.

The quality of these analyses was validated by analyzing Certified Reference Material (CRM) for nutrients produced by KANSO Co., Ltd, Japan. There is no existing reference material for ammonium in seawater, although CRM values were tracked for consistency. The mean of the duplicates is used in this report.

2.4.3 In situ chlorophyll-a concentration

Phytoplankton biomass is represented by the concentration of its main pigment, chl-a, which was measured using Turner fluorometry (Yentsch and Menzel 1963). Details of the protocol and method can be found in Mitchell et al. (2002). In brief, two replicates of 100 mL aliquots of seawater were drawn from each sampling depth and filtered via vacuum filtration (PSI < 10) onto 25 mm glass fiber filters (GF/F). The GF/Fs were immediately deposited into separate scintillation vials containing 10 mL of 90% acetone, which were kept at -20 °C for at least 24 hours to ensure extraction of all the chl-a pigments. Following the extraction period, the aliquots were warmed to room temperature and transferred into fluorometer cuvettes (glass test tubes).

The extracts were exposed to blue light (excitation wavelengths) in the fluorometer, which leads them to emit red light. This red light is detected and quantified by a photomultiplier (Holm-Hansen et al. 1965). Chloropigments other than chl-a (e.g., chlorophyll-b, chlorophyll-c1, -c2, and -c3) can contribute to the overall fluorescence signal, but their contribution is generally minor. Chl-a degradation products (a-type phaeopigments associated with senescent phytoplankton or zooplankton fecal pellets) may sometimes be present in a sample and contribute to the fluorescent signal. To account for their contribution, after taking the first fluorescence measurement, samples were acidified, which converts chl-a into phaeophytin-a. A conversion factor was then applied to retrieve the concentrations of both the chl-a and a-type phaeopigments (Welschmeyer 1994).

2.4.4 Phytoplankton Taxonomic Groups

Biomass of four phytoplankton categories were computed from water samples using their pigment signature. Surface (i.e., between 1 and 20 m depth) water collected from Niskin bottles was immediately filtered using 25 mm GF/F filters at a pressure less than 10 PSI. Between 250 mL to 1 L of water was filtered to ensure enough material was retained for analysis. Filters were stored in cryovials, flash-frozen in liquid nitrogen, and placed in a -80°C freezer until analysis at the Bedford Institute of Oceanography. Concentrations of about 20 pigments were measured using High Performance Liquid Chromatography (HPLC) following Head and Horne (1993) as modified by Stuart and Head (2005). Biomass of eight taxonomic groups (namely, diatoms, dinoflagellates, *Phaeocystis spp.*, prasinophytes, cryptophytes, dictyophytes, haptophytes, and chlorophytes) was determined using eight diagnostic pigments (Roy et al. 2011) in addition to chlorophyll-a; these pigments were chlorophyll-b, chlorophyll-c3, fucoxanthin, peridinin, zeaxanthin, alloxanthin, 19'-butanoyloxyfucoxanthin, and 19'-hexanoyloxyfucoxanthin. Taxonomic composition in terms of biomass was inferred using a statistical approach that simultaneously optimizes the biomass of each group and their pigment signature relative to chl-a concentration using the *phytoclass R* package (Hayward et al. 2023). The approach requires that the statistical analysis is rerun each time the pigment dataset is updated with data from a new mission. Initial pigment signatures for each taxonomic group were taken from Table 2 in Devred et al. (2024), and four tests were conducted to ensure the robustness of the method to changes in the dataset size. The *phytoclass* function was run on the entire dataset, and then a cluster partitioning in 2, 3, and 6 clusters as indicated by the *NbClust* function in *R*, which determines the optimal number of clusters using 30 indices. The similarity in biomass concentration of all taxonomic groups for the four cases (i.e., 1, 2, 3, and 6 clusters) provided confidence in the retrieval of biomass of each groups. Biomass of prasinophytes, cryptophytes, dictyophytes, haptophytes and chlorophytes were summed in an "other phytoplankton" category. The results for the sample taxonomic composition were therefore summarized in four phytoplankton taxonomic groups: diatoms, dinoflagellates, *Phaeocystis spp.* and other phytoplankton. Biomass for each group was converted to the percentage contribution to total biomass as expressed by chl-a. Note that the time series for taxonomic group analysis starts in 2001, while the integrated chl-a (0-100m) derived from fluorometric analysis starts in 1997.

2.4.5 Phytoplankton Apparent Absorption Wavelength (PAAW)

PAAW is the harmonic mean of the phytoplankton absorption spectrum from 400 to 700 nm, namely, the wavelength-weighted mean of phytoplankton absorption coefficients. This approach emphasizes the absorption values in the blue/green (short) wavelengths rather than the red (long) wavelengths (Devred et al. 2022) and provides a single metric in nm that summarises the shape of the absorption spectrum, which changes depending on total phytoplankton biomass and community composition. In the Labrador Sea, PAAW varies from about 461 nm (blue/green) to 498 nm (orange), the low values being indicative of low biomass and likely small

phytoplankton cells, while the higher wavelengths suggest high biomass and a phytoplankton community structure dominated by large cells such as diatoms.

Surface (1-2 m depth) water samples (250 to 1000 mL depending on visual inspection of the filter to ensure enough material was retained) were filtered on a GF/F 25 mm filter immediately after collection from the Niskin bottle, flash frozen in liquid nitrogen, and stored in a -80°C freezer until analysis upon return to BIO. Particulate absorbance was measured on the filter using a UV-Vis Shimadzu 2600i using an integrating sphere, and the filter was then placed in hot methanol (60°C) for 25 to 45 minutes to extract pigments. A second measurement of the filter after pigment extraction was performed to obtain detritus absorbance. Particulate and detritus absorption were derived by using the path length correction formula from Stramski et al. (2015) with coefficients from Equation 5.5 in Neeley et al. (2018) on the absorbance values. Phytoplankton absorption (m^{-1}) was calculated by subtracting detritus absorption from particulate absorption, and the spectra were smoothed using the *smooth.spline* function from the *stats* package in *R* (R Core Team 2022) with the degree of smoothing set to 55. The absorption at 700 nm was subtracted from the spectrum, assuming the absorption at 700 nm would be zero. Finally, PAAW was calculated using the smoothed phytoplankton absorption as input to the equation from Devred et al. (2022).

2.4.6 Satellite-derived chlorophyll-a concentration and bloom metrics

In addition to in situ measurements, chl-a concentrations were derived using satellite ocean colour. This mode of observation provides information on phytoplankton biomass at synoptic scales and daily frequency (assuming clear skies). These satellite-derived data are used to complement the in-situ observations by providing context to the seagoing missions, including a suite of metrics to characterize the phytoplankton spring bloom (described below in this section). Satellite data presented in this document were retrieved from the OC-CCI multi-sensor product generated by the Plymouth Marine Laboratory (PML) as part of the European Space Agency (ESA) climate change initiative (Table 1, Sathyendranath et al. (2019) and Sathyendranath et al. (2023)), which provides daily data from September 1997 to the present. Previous reports used data from the MODIS-Aqua sensor alone, which was launched in 2002. However, there has been a decline in data quality from this sensor since 2023 (Twedt et al. 2023), and therefore a decision was made to adopt the OC-CCI product, which offers improved spatial and temporal coverage due to the use of multiple satellite optical sensors.

For this report, global daily level-3 binned data at 4 km resolution were downloaded from PML (Table 1) and data were extracted for the three regions of interest, namely, AR7W-West (AR7W-W, -55.7°E to -53.7°E and 53.6°N to 55.5°N), AR7W-Central (AR7W-C, -53.7°E to -48.8°E and 55.5°N to 60.1°N), and AR7W-East (AR7W-E, -48.8°E to -48.1°E and 60.1°N to 60.7°N) (Figure 1). The boundaries of these boxes were designed to delineate the main regions along the AR7W line: Labrador shelf and slope, central Labrador Sea, and the Greenland shelf and slope. In previous reports, these polygons were referred to as the Labrador Shelf (LAS), Central Labrador Sea (CLS), and the Greenland Shelf (GS), respectively, but have been renamed to reduce confusion when referring to the shelves or the central Labrador Sea as a whole. Remote sensing reflectances were used to generate chl-a using the POLY4 algorithm (Clay et al. 2019), a modified version of the band ratio model OCx (O'Reilly et al. 1998) with regionally-tuned coefficients to correct for a bias observed in the Northwest Atlantic.

Metrics were derived from satellite chl-a using the PhytoFit R shiny app (Clay et al. (2021), see Table 1). Data were $\log_{10}$-transformed to allow better modelling of the exponential increase in chl-a at the initiation of the bloom. Daily averages and SD were calculated within each of the three Labrador Sea polygons (AR7W-W, AR7W-C, and AR7W-E), filtering pixels outside ±3 SD from the mean. Days with less than 20 % coverage were excluded from the time series, and the

remaining points were smoothed using the LOESS method (locally-estimated scatterplot smoothing) as implemented in *R* (*loess* function, R Core Team (2022)) with a span window of 0.2 (a parameter that controls the degree of smoothing) and weighted by percent coverage (i.e. percent area of the region of interest that is observed by the satellite, as cloud cover results in missing data). A symmetric shifted Gaussian was fitted to the smoothed points with nonlinear least squares regression using the *nlsLM* function of the *minpack.lm* package in *R* (Elzhov et al. 2023), and the chl-a baseline was allowed to vary linearly as a function of time. The Gaussian fits were restricted to days 85 to 299, and the day of initiation and day of maximum concentration were restricted to day ranges 85-226 and 108-247, respectively to avoid classification of small early peaks of the spring bloom.

In previous reports, the spring bloom metrics (the timing of the start of the bloom, the duration, peak concentration during the bloom period, and "magnitude" or total chl-a produced during the bloom period) relied mainly on the accuracy of the Gaussian fit, which was subject to high variability in chl-a concentration and low data coverage, particularly in the north and early in the year. This resulted in an absence of model fits, or problematic fits that may not have accurately captured the interannual anomalies in each region. To reduce the impact of these bad fits on the scorecards, and retrieve information about bloom timing and intensity, a new set of a metrics were recently proposed: spring bloom peak timing and fall bloom initiation, and "seasonal" averages, where the season boundaries are region-specific and based on the climatology of the spring and fall bloom periods observed over the time series (See Figure 35, and Bélanger et al. (in prep.)). While the spring metrics are still derived from a Gaussian fit, we now report on the peak of the curve instead of its initiation, as it does not require a subjective threshold (i.e., percentage of maximum chl-a) and it remains robust to small variation in chl-a early in spring. All fits were visually inspected to ensure that the bloom peak timing was accurately captured by the model, and the input parameters were adjusted if necessary.

The fall bloom period is less predictable than the spring bloom as its signal is not as large as in the spring, and satellite data are more sparse due to cloud cover. Rather than a Gaussian model, a threshold method was used to define the start of the bloom as the day of year when chl-a concentration surpasses 5% over the annual median and remains above this threshold for 14 consecutive days (Layton et al. 2022). In this case we used the LOESS-smoothed data spanning between day of year 151 and 365 with the initiation occurring between day of year 151 to 270. The timing of the fall bloom initiation was reported rather than the peak, as the peak may occur late in the year when data coverage is poor.

The mean chl-a for each region-specific "season" was calculated as an average of the daily chl-a concentrations within that season, weighted by daily percent coverage. Note that in this calculation, daily chl-a concentrations correspond to the averages calculated using absolute (i.e. not log-transformed) values within the polygons, after filtering outlying pixels. Data coverage is very sparse or non-existent in the Labrador Sea from November to January (see Figure 35). Days with valid data that have low coverage (<20%), a common occurrence early or late in the year, might not be representative of the overall conditions. Sea ice also impacts the quality of the data and may introduce artifacts close to the ice edge (Bélanger et al. 2007). Although weighting points by percent coverage lessens the impact of low data coverage, extra caution must be used when interpreting results in late fall or winter due to these issues.

2.4.7 Mesozooplankton

Mesozooplankton were collected using vertical net hauls in the upper 100 m, where 95% of the biomass in spring-summer occurs (Astthorsson and Gislason 2003), using a 0.75 m diameter ring net fitted with a 200 µm mesh size and a 0.5 m diameter ring net with a 76 µm mesh size. The cod-end was attached via a clamp to a weighted hydro-wire and the towing bridles were

attached to a crossbow mounted on the wire, at a height equal to the length of the net such that the net was held vertically during the descent and ascent. In this configuration, zooplankton were only collected as the net was towed upwards. The towing speed was about 0.5 $\mathrm{m\ s^{-1}}$ and the volume of water sampled was assumed to be the volume of the cylinder sampled by the net, until 2010, when the filtered volumes started to be measured using a Danemark K/C flowmeter. The flowmeter was equipped with a back-spin pin, to prevent the impeller from spinning during the descent of the net, so that it only measured flow during the ascent. Samples were preserved in 2% formaldehyde solution. For *C. finmarchicus*, *C. hyperboreus*, and *C. glacialis*, specimens were identified and enumerated to the level of species and stage, and size-frequency distributions of sizes-at-stage were constructed for all stages at each station. To track anomalies in reproduction events and population growth, the Population Development Index (%PDI) was calculated as the ratio of young copepodite stages (CI-CIII) over the total abundance, expressed as a percentage (Head et al. 2008). Other taxa were identified to the level of species (sometimes to stage), genus, or group, depending on their abundance in the samples. Meaningful abundances were obtained when quantitative subsamples with a minimum of 300 organisms, and a minimum of 200 *Calanus spp.*, were counted to allow assessment of community structure and *Calanus* population growth/development, respectively.

2.4.8 Spatio-temporal binning

All data are aggregated following a spatio-temporal scheme to summarise the information in simple metrics. The data in this subsection are summarized over the three main regions of interest defined in section 2.4.6 (AR7W-W, AR7W-C, and AR7W-E, see Figure 1).

All nutrients and Turner-fluorometric chl-a concentrations were integrated over selected depth ranges, namely, chl-a from 0 to 100 m, surface nutrients from 0 to 100 m, and deep nutrients from the first depth below 100 m to bottom. HPLC chl-a and taxonomic group percentage contributions to total biomass were averaged over the top 20 m in the water column. Temperatures were averaged from 0 to 100 m. Zooplankton values correspond to the integrated abundances in the water column (0–100 m) since collection was carried out using vertical net tows (see section 2.4.7). Following the vertical binning, the data were averaged by region and year.

2.4.9 Scorecards

Annual anomalies for surface temperature, surface and deep nutrients, chl-a concentration, mesozooplankton abundance, PAAW, HPLC chl-a concentration and phytoplankton taxonomic group percentage contributions to total biomass, and satellite ocean colour metrics were calculated as the deviation of an individual year from the mean of the annual estimates over a reference period (defined below), and expressed as normalized quantities (i.e., by dividing by the SD of the annual estimates over the same period):

$$A_y = (M_y - M_r)/\sigma_r$$

where A_y is the anomaly for a given property in a given year (y) and region, M_y is the annual mean, M_r is the reference period mean and σ_r is the SD for the reference period (1999-2025). This method was selected because it provides good estimates of anomalies and trends for data with large gradients and gaps (Jones and Hulme 1996). Note that years when sampling occurred after day of year 170 (i.e. during summer, see 1998, 1999, 2002, 2003, and 2020 in Figure 2) were excluded from calculation of the in situ data reference period and omitted from the scorecards (Figures 26-31 and 34). These samples, collected in the summer rather than spring during the typical bloom period, would reflect a different dynamic and skew the climatology. The time series of HPLC data used in phytoplankton taxonomic grouping starts in

2001, so the reference period for this dataset is 2001-2025. Due to the absence of missions in 2017 and 2021, these cells are also greyed out in the scorecards. Note that the report on Labrador Sea conditions in 2024 (Clay et al. 2026) used a reference period ending in 2020 for the biological data, which was updated to 2025 this year to include the latest five years of data.

2.5 Access to data products

Data products presented in the figures of this document are available on request to the corresponding author. The satellite ocean colour data can be found in Phytofit and the bloom metrics (i.e. bloom timing and weighted "seasonal" averages, see Figure 32) are available in the PhytoFit github repository (Table 1). All the chemical data are available at the Ocean Carbon and Acidification Data System (OCADS, Table 1).

3 RESULTS AND DISCUSSION

3.1 Physical data

3.1.1 North Atlantic Oscillation (NAO) Index

The North Atlantic Oscillation (NAO) is a crucial teleconnection pattern that significantly impacts atmospheric processes in the Labrador Sea (Barnston and Livezey 1987; Hauser et al. 2015). During a positive NAO phase, low-pressure anomalies over Iceland and the Arctic, coupled with high-pressure anomalies across the subtropical Atlantic, drive stronger-than-average westerly winds at mid-latitudes. This generally leads to colder and drier conditions in the northwestern Atlantic, including the Labrador Sea region. Conversely, a negative NAO weakens both the Icelandic low and the Azores high, reducing the pressure gradient across the North Atlantic and generally resulting in weaker westerlies and warmer conditions. Both NAO phases are associated with basin-wide changes in the intensity and location of the atmospheric jet stream and storm track over the North Atlantic ocean, as well as large-scale fluctuations in zonal and meridional heat and moisture transport (Hurrell 1995). These changes ultimately modify temperature and precipitation patterns. While this report primarily focuses on the 2025 conditions in the context of the past several decades, we analyze the NAO record to contextualize recent conditions within the broader history of atmospheric patterns over the North Atlantic.

The wintertime (JFM) NAO exhibits significant multi-decadal variability (Hurrell (1995); Figure 3). A notable upward trend in the NAO index was observed from the 1960s to the 1990s (Visbeck et al. 2001). However, a slight downward trend followed the peak in the 1990s, persisting until 2010. Recent research has identified an atmospheric circulation pattern that becomes more pronounced during periods of low NAO (Hauser et al. 2015). Further investigation of this complementary pattern will enhance our comprehension of atmospheric and oceanic conditions, ultimately improving forecasting capabilities. In 2010, the NAO index reached a record low (Figure 3). The following year it rebounded, only to strengthen significantly in 2012, reaching levels comparable to the mid-1990s. A dramatic shift occurred in 2013, with the NAO index becoming strongly negative. The index returned to a high positive phase in 2014, though slightly weaker than 2012. Another peak in positive NAO values was observed in 2015, the largest since 1989. More recently, 2020 saw a strong positive NAO, followed by a moderate negative phase in 2021. In 2022, the NAO index returned to a strong positive phase, slightly weaker than 2020. 2025 exhibited a near-normal but slightly negative NAO condition.

3.1.2 Surface air temperatures

In 2025, strong warming conditions were observed in the majority of northern part of the domain in the winter and fall seasons, reaching values of approximately 4.0 °C or above over the Hudson Bay and Baffin Bay (Figure 4). Cold anomalies were present to the east of Newfoundland and to the east of Nova Scotia, over the deep ocean regions in the spring of 2025, and these cold anomalies increased and expanded throughout the Labrador Sea in the summer.

Figure 5 presents time series plots of air temperature anomalies within the central Labrador Sea (outlined by the black polygon, P3300) for the four seasons from 1950 to 2025. Mid-1980s experienced the lowest temperature in all four seasons in this period, and 1993 recorded the second lowest temperature in the winter season. The air temperature in winter appears to have stronger inter-annual variability than in the other three seasons, particularly in the spring and summer. In 2025, the air temperature anomalies were positive for winter and fall in the central Labrador Sea, with winter anomalies at 1.0 °C and fall at 0.9 °C. The spring anomaly was close to normal, and summer anomaly was 0.7 °C below normal.

3.1.3 Sea surface temperature (SST)

In 2025, a combination of cold and warm anomalies were present in the four seasons in the northwest Atlantic Ocean (Figure 6), with large negative anomalies in the Labrador Sea in spring and summer, slightly negative anomalies in winter, and prominent warm anomalies in the southern part of the domain in spring and summer. The negative anomalies seen in summer shrank in the fall.

To illustrate SST variability in the central Labrador Sea (P3300 polygon), Figure 7 presents SST anomalies relative to the 1991-2020 climatology. Consistent with the air temperature, mid-1980s recorded the largest negative changes in all the four seasons, while the second largest ones were in early 1970s. SST variations at the Ocean Weather Station Bravo (56 °N, 51 °W; in the central Labrador Sea) investigated by Loder and Wang (2015) (see their Figure 3) are consistent with the pattern observed in summer in the present analysis (Figure 7). Most of the positive anomalies observed over the time series have occurred since 2003. In 2025, winter, spring, and summer SST anomalies were below normal (winter: -0.08 °C, spring: -0.36°C and summer: -0.42°C). In contrast, the 2025 fall anomaly was above normal (0.32 °C).

3.1.4 Sea ice

Sea ice extent (i.e. the area in which sea ice concentration exceeded 15%, see section 2.2.4) in 2025 was lower than the climatology in January and February on the entire Labrador coast and around Newfoundland (Figure 8). In March the sea ice extent was close to normal on the Labrador Shelf, but below normal on the Newfoundland Shelf. Sea ice concentration was mostly lower than normal (i.e., Labrador Shelf and Newfoundland) during the three winter months. A large positive anomaly occurred in March on the Labrador Shelf.

Sea ice extent anomalies were computed for three latitude bands in the Labrador Sea region: 63-68°N (Davis Strait), 58-63°N (Northern Labrador Sea), and 53-58°N (Labrador Shelf) for the winter and spring from 1979-present (Figure 9). In 2025 in the two seasons and across the three regions, the ice extent anomalies were close to the climatological average of the 1991-2020 period, except for Davis Strait in winter, which was below normal.

3.1.5 Current transport from CTD and altimetry data

The transport over the Labrador Slope from the 700-m to 3000-m isobath has a mean value of 16.2 Sv (southeastward) over the 1993-2020 reference period, with large variations year-to-year (SD of 4.6 Sv). The estimated transport ranges from 4 to 26 Sv. The transport over the Labrador Shelf (to the 700-m isobath) has a mean value of 3.7 Sv (southeastward) over 1993-2020, with a SD of 0.9 Sv. Note that the transport estimate is sensitive to the choice of isobaths which determine the spatial extent used for calculating transport. In particular, the transport over the Labrador Slope in some years is highly sensitive to the choice of the offshore extent because this current can have two branches (Wang et al. 2016) and a variable recirculation gyre can influence the transport magnitude. The offshore extent of the Labrador Current averaged over 1993-2020 is approximately located at the 3000 m isobath.

The time periods of the CTD and altimetry data used in the current transport calculations vary from May to early August, depending on the year. During this time of year (spring-summer), the Labrador Current is weaker than in fall and winter (e.g. Han et al. (2008)). Figure 10 shows the standardized indices of the spring-summer Labrador Current transport over 1993-2025 for the Labrador Slope (between 700- and 3000-m isobaths) and the Labrador Shelf (inshore of the 700-m isobath). In 2025, the slope branch was below normal (mean transport over the reference period) and the shelf branch was slightly above normal.

3.1.6 Argo temperature and salinity

Argo data is used to monitor the state of the ocean and to improve our understanding of climate variability and change, particularly during periods when ship and satellite measurements are limited. The value of the Argo floats is even more significant in winter, when they serve as the only means of providing information about real-time development of winter convection. By tracking temperature and salinity changes at various depths, Argo data reveals the rate of ocean warming or cooling, which is vital for understanding the impact of climate change on marine ecosystems and sea level rise.

Deployment of Argo floats in the Labrador Sea began in 2002, with about 150 measured profiles that year (Figure 11, right panel). The number of profiles increased continuously to about 1200 profiles in 2012, with a peak of almost 1500 profiles in 2021. A total of 15791 Argo profiles from the Labrador Sea region were used to compute the climatology by grouping them in 1° x 1° grid cells from 2002 to 2020 (Figure 11, left panel). For each grid cell, the mean temperature, salinity, and density were computed for four layers: 0-50 dbar, 100-500 dbar, 500-1000 dbar, and 1000-2000 dbar. In 2025, 1089 Argo profiles were collected across the entire Labrador Sea region (Figure 11, middle panel).

The temperature and salinity in the near-surface layer (0-50 dbar) are the most variable in comparison to the other layers due to the effect of atmospheric forcing (Figures 12 and 13, top row). The climatology shows slightly cooler (about 3 °C) and fresher (practical salinity of about 34) water along the slope regions and in the north, compared to relatively warm (6-7 °C) and salty (35) water in the central Labrador Sea and south of Greenland. In 2025, temperature anomalies in the surface layer did not show any clear spatial patterns except for warmer-than-normal water along the Labrador slope and in the east below Greenland, and a patch of cooler water in the northwest. 2025 salinity anomalies showed fresher water in the north and near-normal conditions in the south.

The climatological temperature and salinity distributions in layers below 100 dbar (Figures 12 and 13, left panels) show the opposite pattern to the surface layer climatology, with cooler, fresher water in the central Labrador Sea and warmer, saltier water elsewhere. A band of cold, fresh water is also visible along the Labrador slope in the 100-500 dbar layer, which is attributed

to the influence of the Labrador Current. Conversely, the presence of warmer waters in the 100-500 dbar layer on the Greenland side indicates the influence of the Irminger Current, which advects warm salty Atlantic waters into the region. The 500-1000 dbar layer corresponds to the upper limit of the Labrador Sea Water resulting from winter convection (Yashayaev 2007). As depth increases, water becomes cooler and saltier, and water masses become isolated from surface forcing, resulting in homogenization of the physical properties. Climatological temperatures range from about 3.7-4.5 °C in the 100-500 dbar layer and 3.4-3.6 °C in the 1000-2000 dbar layer, while climatological salinity ranges from 34.82-34.92 in the 100-500 dbar layer and about 34.88-34.91 in the 1000-2000 dbar layer.

The general patterns observed in the layers below 100 dbar in 2025 (Figures 12 and 13, middle panels) exhibit similarities to the climatological distributions, albeit with varying magnitudes. In 2025, the Labrador Sea experienced temperatures predominantly warmer than the climatology in all layers below 100 dbar, with significant positive anomalies (up to 0.4°C) in the 100-500 dbar layer (Figure 12, right panel). Salinity in 2025 was generally lower than the climatology between 100 and 1000 dbar, indicating fresher conditions, with the 100-500 dbar layer showing an area of saltier conditions outside of the central Labrador Sea. A combination of slightly positive and negative salinity anomalies were present at depths between 1000 and 2000 dbar.

Seasonal changes in the Labrador Sea are an important indicators to monitor under a changing climate, particularly in the upper ocean layers. A monthly climatology of temperature and salinity for the central Labrador Sea was derived from Argo data spanning 2002-2020. The climatological temperature in the central Labrador Sea between 100 and 500 dbar (blue shaded area, Figure 14) reaches its minimum in March (~3.5 °C) and maximum in November (~4.0 °C). Climatological salinity in the same layer (Figure 15) is lowest in January (~34.83) and highest in October (~34.85).

In 2025, temperatures in the 100-500 dbar depth range of the central Labrador Sea closely followed the climatology with the exception of January and February, which were about 0.4 ˚C warmer than the climatology. These months exceeded the climatology by +0.38 °C and +0.35 °C respectively. This continues the trend observed in winter last year where December 2024 was +0.24 °C warmer than the climatology (Clay et al. 2026). Conversely, salinity was consistently lower (fresher) than the climatology in every month of 2025 (Figure 15). This freshening may indicate increased freshwater inputs, potentially from enhanced Greenland glacier melting or Arctic sea ice melt, driven by warming air temperatures at high latitudes (Schiller-Weiss et al. 2024).

The result of the mixed layer depth calculated from Argo profiles is discussed in section 3.1.8.

3.1.7 Shipboard observations of temperature, salinity, and density

To capture interannual variability amidst strong seasonal fluctuations in physical, chemical, and biological conditions, the annual AR7W survey is conducted as early in the spring as feasible. Sea ice typically restricts access to the Labrador Shelf until mid-May. Each mission encompasses at least 30 stations between Labrador and Greenland, where CTD profiles are obtained, and water samples are collected at up to 24 depths. While CTD data are paramount, a comprehensive suite of sensors is routinely deployed on every AZOMP mission.

The hydrographic climatology for the 1991 to 2020 reference period was established for the AR7W line using CTD profiles from the annual surveys (Layton et al. 2026). These benchmarks allow us to quantify anomalies in temperature, salinity, and density.

Based on the climatology, waters along the Labrador Shelf (AR7W-W), with depths reaching about 200 m, are characterized by relatively cold temperatures (<2 °C) that are homogeneous

through depth, and salinity that increases (32 to 34.5) with increasing distance from the coast (Layton et al. 2026). In the Labrador Basin (AR7W-C) the top 200 m contrast sharply with the Labrador Shelf, with relatively warmer (3.5 to 4 °C) and saltier (34.5 to 34.8) waters. Temperature and salinity are relatively constant until about 200 m when temperature steadily decreases to the bottom. The coldest waters, below 2.5 °C, occur below about 2500 m and correspond to the North Atlantic Deep Water and the Denmark Strait Overflow Water (Yashayaev 2007). On the Greenland Shelf (AR7W-E), with depths reaching about 120 m, there are gradients of temperature and salinity, both increasing with increasing distance from the coast, with relatively cooler (0 to 2 °C) and fresher (33.0) waters near the coast. Along the shelf break (stations AR7W-24 to AR7W-26) waters are relatively warmer (>4 °C) between 100 and 1000 m.

In 2025, the Labrador Shelf (AR7W-W) and the Labrador Basin (AR7W-C) were sufficiently sampled, however, only one station on the Greenland Shelf (AR7W-E) was sampled, precluding a full assessment of the conditions. Between about 750 and 1250m, the temperature anomaly was up to +0.25° C, and below this depth the temperature was close to normal (top right panel, Figure 16). A thin surface layer of cold anomaly was present in the central basin, which is consistent with cold SST anomaly in spring (Figure 6).

Across most of the transect, from near-surface to 500 m, the negative (fresh) anomaly reached a minimum of about -0.05 (middle right panel, Figure 16). Below 1000 m salinity was mostly close to normal, with the exception of a small positive (salty) anomaly at 2000 m in the central basin.

For the density anomaly (bottom right panel of Figure 16), a combination of relatively warmer and fresher waters resulted in less dense waters above 1000 m, but the density was close to normal below 1000 m. Wang et al. (2019) identified an ongoing decrease in water density in deep layers as a mechanism for the weakening of the Atlantic Meridional Overturning Circulation (AMOC).

The Labrador Current, encompassing both its inshore and offshore branches, is a southward extension of the Baffin Island Current. It transports cold, relatively low-salinity waters originating from Baffin Bay and the Hudson Strait outflow (Wang et al. 2015). These waters are enriched with freshwater inputs from Arctic and subarctic sources, contributing to the current's distinct thermohaline characteristics. On the Labrador Shelf, the low salinity and cold temperatures observed at the surface were thus likely a direct reflection of these freshwater influences, modulated by seasonal and regional oceanographic processes. A cold intermediate layer (CIL) was also observed between approximately 50 m and 150 m depth (left panels of Figure 17), characterized by its low temperature.

The right panels of Figure 17 show the temperature (top), salinity (middle) and density (bottom) anomalies in 2025. Along the shelf edge, temperature anomalies reached a significant peak of +1.0 °C. Salinity and density exhibit closely coupled spatial patterns: near-coastal regions are characterized by a marked freshening of up to -0.3 PSU and a corresponding density reduction of -0.2 $kg\ m^{-3}$. In contrast, the upper water column (surface to 50 m) is largely dominated by positive anomalies in both salinity and density across most of the section.

It is clear the central Labrador Sea water mass experienced significant changes over the 30 year-period as indicated by records of temperature, salinity, and density (left panels of Figure 18). In the early 1990s, a cold, fresh and dense water mass at a depth of about 100 m to 2300 m was the dominant feature, which corresponds to the high NAO indices (Figure 3) and low air temperatures (Figure 5) during this period. This can be linked to the role of atmospheric forcing on the water mass formation in the Labrador Sea, resulting in a well-mixed water column during the winter from the surface to approximately 2000 m (Yashayaev and Loder 2016; Wang et

al. 2019, 2022; Yashayaev 2024). The right panels of Figure 18 illustrate the evolution of anomalous temperature, salinity, and density, revealing a clear transition from the persistent cold and fresh anomalies of the 1990s to a sustained warming and salinification phase post-2010. During this shift, 2010 stood out as a year of particularly shallow convection (~600 m), after which warm anomalies dominated the upper 2000 m through 2015. While the temperature throughout the entire water column has stabilized within 0.25 °C of the climatology by 2025, salinity and density exhibit more complex, depth-dependent trends. In the upper layer (100–500 m), a freshening trend of up to 0.05 PSU has emerged since 2023, resulting in a corresponding density decrease of 0.05 kg/m relative to the climatological baseline. In contrast, the deep layer (2000–2500 m) has maintained a persistent salty anomaly of up to 0.0375 PSU since approximately 2010, which continues to spread through the deep interior into recent years.

3.1.8 Mixed Layer Depth and convection depth

The parameters of each methodology used to estimate convection depth with CTD data in this report were tuned against historical convection depth estimates to ensure accuracy and consistency with the established estimates. The convection depth climatology in the Labrador Sea, as documented by Yashayaev and Loder (2016) and Yashayaev (2024), indicates convection depths exceeding 500 m throughout the period from the early 1990s to 2023, even during periods of very low winter NAO index. Our analysis suggests a very shallow convection event in the winter of 2025, with a depth of ~450 m.

The historical record of monthly median mixed layer depth and stratification index computed from Argo data is shown in Figure 19. Since 2021 we have observed annual maximum monthly median mixed layer depths shallower than the climatological average. Additionally, since 2020 the upper water column has been more stratified than average, until 2025 where stratification is observed to have weakened and is slightly below the average. These results are summarized in Figure 20 where the yearly convection depth and maximum stratification index are shown. In 2025, a convection depth of ~400 m was observed, which is in good agreement with the convection depth computed from the CTD data and is the shallowest convection since 2010 when a record shallow convection depth of ~380 m was observed. It should also be noted that the deep convection depth in 2025 was observed in the month of April which is later than usual, as the Argo record shows. Convection depths observed in April in other years tended to be shallower than average as well (2003, 2009, 2019, and 2025).

3.2 Chemical data

3.2.1 Transient tracers CFC-12 and SF_6

During the second half of the twentieth century, the atmospheric burden of CFCs increased steadily, due mainly to their widespread use as refrigerants and aerosol propellants. The invasive atmospheric flux of these mostly inert gases provided an excellent record of ocean circulation, and profiles of dissolved CFC-12 concentration have been measured annually along the AR7W line since 1991 (Figure 21). As a consequence of restrictions on the manufacturing and use of ozone-depleting substances introduced in 1989, the atmospheric mixing ratio of CFC-12 has been in decline since 2003 and its capacity at tracking recent ventilation episodes has become limited. Data quality issues affected the 2023 CFC-12 measurements, and these data are not considered reliable; this behavior is consistent with known backflush timing complications. The 2022 dataset, however, has been quality controlled using the “crossover” method (Lauvset and Tanhua 2015) and are considered reliable.

Measurements of an alternative transient tracer, SF_6, were introduced in 2011. There has been a rapid, near-linear increase in atmospheric SF_6 since 2011 (+0.09 $\mathrm{fmol\ kg^{-1}\ y^{-1}}$) reflected in

the dissolved concentration profiles of the Newly Ventilated Labrador Sea Water (NV-LSW) (Figure 21).

3.2.2 Dissolved Inorganic Carbon and pH

The Labrador Sea hosts a strong "solubility pump": atmospheric anthropogenic CO_2 is sequestrated to the deep ocean by chemical and physical processes. DIC concentration increased by 0.87 $\mu mol\ kg^{-1}\ y^{-1}$ from 1996 to 2025 (Figure 22). As a result, the pH decreased by 0.1 pH units during the same period (Figure 22) representing a decline rate of 0.003 y^{-1}. Trends between 1996 and 2025 were highly significant with a correlation coefficient, r^2, explaining respectively 96% and 86% of the variance in DIC and pH, respectively. Arctic outflow and the local uptake of anthropogenic CO_2 in the deep-convection region of the Labrador Sea are major controlling mechanisms for the state of ocean acidification in the Northwest Atlantic. The observed increase of acidification affects not only the local region but also downstream areas. The Arctic water flows into the highly productive regions in the Northwest Atlantic, which have important commercial fisheries and make these regions more susceptible to future ocean acidification than other regions (Azetsu-Scott et al. 2010).

3.2.3 Dissolved oxygen

A section plot of all the Winkler titration measurements for 2025 (Figure 23) identifies the region of ventilation (surface between ~100-500 m) which overlies an intermediate region that hasn't been ventilated since 2022 (see Figure 20, left panel). This intermediate region overlies the NEADW which is the oldest water mass in the water column and contains the lowest dissolved oxygen concentrations. A timeseries of Winkler dissolved oxygen measurements shows the variability of the NV-LSW and the NEADW masses over the last 3 decades (Figure 24). Dissolved oxygen in the NEADW has been below average since 2003, and generally near average since 2006 in the NV-LSW.

Figure 25 shows dissolved oxygen in the 100-500 dbar layer derived from Argo floats. A mix of negative and positive anomalies near the AR7W-line in the central basin confirms the slightly above average dissolved oxygen concentration observed in the NV-LSW from Winkler titration measurements in 2025.

3.3 Biological data

3.3.1 Surface temperature (0 to 100 m)

Because the timing of the cruise affects the average temperature for a given region and year, removal of the years 1998, 1999, 2002, 2003, and 2020 (due to later-than-usual sampling dates, Figure 2) from the reference period (1999-2025) lowered the temperature by about 0.2 °C with little effect on the anomaly patterns (not shown here). AR7W-W exhibited a lower temperature in the top 100 m (mean of 0.8 °C) than AR7W-C (mean of 3.8 °C) and AR7W-E (mean of 2.1 °C) due to the inflow of Arctic water (Figure 26). The warmest years occurred in 2000 (AR7W-W, +1.72 SD, unitless), 2019 (AR7W-C, +1.62 SD), and 2008 (AR7W-E, +2.36 SD) (Figure 26). The coolest years occurred in 2007 (AR7W-W, -1.42 SD), 2018 (AR7W-C, -1.52 SD), and 2011 (AR7W-E, -1.45 SD).

In 2025, temperatures in all three regions were near or slightly below normal. This trend of near or below normal temperatures has persisted since 2011, with the exception of scattered high warm anomalies in 2012, 2019, and 2023 in AR7W-C, and in 2015, 2018, and 2024 in AR7W-W.

3.3.2 Nutrients

All near-surface nutrient concentrations (i.e., 0–100 m, nitrate, phosphate, and silicate) exhibited inter-annual variations between 1997 and 2010, followed by three years (2011 to 2013) of near or below average nutrient levels for all regions, except for silicate (AR7W-W, 2011) and phosphate (AR7W-C, 2013) (Figure 27). From 2014 to 2018, all nutrients levels were above normal except for nitrate in 2015 in AR7W-C. While no patterns are observed between nutrients and regions before 2011, all regions and nutrients anomalies were correlated between 2011 and 2019.

From 2019 to 2024 (excluding 2020-2021 when there were no sampling missions), surface nutrients (0-100 m) were negative in AR7W-W and AR7W-C. In 2025, nutrients remained below normal in AR7W-W, but positive nutrient anomalies were observed in AR7W-C after record-low anomalies in 2024. In the same period (2019-2025), AR7W-E experienced more variability, with positive nutrient anomalies in 2025.

Deep nutrients (>100 m) showed a different pattern than the surface nutrients over the climatological period, in agreement with the hydrodynamics of the Labrador Sea and the surface-layer biological activity (Figure 28). Deep nutrients levels are less impacted by the timing of the mission as they are not consumed by phytoplankton and microbial remineralization at depth replenishes the nutrient pool. Filtration of water samples may not impact deep nutrients to the same degree as shallow nutrients, as there is less particulate material collected at depth. Deep nutrient anomalies showed large interannual variability between 1999 and 2018 (Figure 28). While no clear trend has emerged for the scorecards, patterns in deep nutrients have coincided with surface nutrients since 2019. In the period from 2019 to 2024, all deep nutrients showed below-average levels, except for nitrate in AR7W-C in 2022 and AR7W-E in 2024, which were near normal. In 2025, deep nutrients remained below average in AR7W-W, while AR7W-C rebounded to above-average nitrate and silicate, and all nutrients in AR7W-E rose to above average concentrations with record high nitrate and silicate.

3.3.3 In situ chlorophyll-a concentration

In general, the AR7W-E region has high levels of integrated chl-a with a mean of 366 $\mathrm{mg\ m^{-2}}$ from 1999 to 2025 (Figure 29), and is dominated by microphytoplankton with low concentrations of picophytoplankton. Conversely, AR7W-C is a region with low integrated chl-a (169 $\mathrm{mg\ m^{-2}}$), a lower proportion of nanophytoplankton than the AR7W-E region, and high concentrations of picophytoplankton. AR7W-W exhibits the lowest concentrations of integrated chl-a (151 $\mathrm{mg\ m^{-2}}$) and micro and nano-phytoplankton dominate the phytoplankton assemblage, with low biomass of picophytoplankton. Upper ocean (< 100 m depth) phytoplankton sampled on the AR7W section in spring and early summer between 1999 and 2022 showed region-specific characteristics (Li and Harrison 2014; Fragoso et al. 2016; Devred et al. 2024).

Integrated chl-a shows a low frequency variability with a given trend (above or below average) that remains for several years at a time (Figure 29). In that respect, the time series for AR7W-W and AR7W-C show two periods of lower-than-normal levels, from about 2001 to 2005 and from 2014 to 2019, while the remaining periods typically show near or above-normal values. Record-high levels of integrated chl-a occurred in 2015 in AR7W-C and 2022 in AR7W-W. The 2015 AR7W-C record corresponded to a very large bloom of *Phaeocystis spp.* (Devred et al. 2024, 2025) that occurred across the entire region (Figure 30). On the other hand, the record high chl-a in AR7W-W in 2022 was related to above-normal contribution of diatoms. AR7W-E showed a different pattern than the two other regions, with lower than normal values between 2004 and 2008, followed by a period of large interannual variability (2009 to 2013, 2009 being the record

high). Since 2014, integrated chl-a in AR7W-E has been lower than average, except for near-normal concentrations in 2023.

In 2025, integrated chl-a anomalies were above-normal in AR7W-W. In AR7W-C, chl-a dropped to below-average concentrations after a two-year period of near-normal anomalies. AR7W-E integrated chl-a remained below normal, continuing the trend observed since 2014 in this region.

Integrated chl-a levels do not necessarily reflect nutrients concentrations, which can be somewhat explained by the timing of the missions (Figure 2). For instance, in 2013, the mission sampled the transect at the peak of the bloom (as indicated by satellite ocean colour), resulting in high integrated chl-a and low nutrients, likely depleted by phytoplankton consumption. Conversely, in 2014, the mission sampled the AR7W before or at the start of the spring bloom, when chl-a concentration was low and surface nutrients levels high. Similarly, both 2022 and 2023 missions in AR7W-W and in AR7W-C occurred at the peak of the spring bloom (Figure 2), corresponding to high integrated chl-a values and low nutrients values, while the 2024 mission sampled these regions at the tail end of the bloom when chl-a concentrations were lower and nutrients depleted.

3.3.4 Phytoplankton Taxonomic Groups

In general, chl-a biomass at the surface (i.e., < 20m) derived from HPLC (Figure 30) follows similar patterns to the integrated chl-a (0-100m) derived from fluorometry (Figure 29). Discrepancies can be explained by the presence of deep chl-a maxima that are not accounted for in the surface values. In 2025, surface chl-a was above-normal in the AR7W-W and below-normal in AR7W-C and AR7W-E.

Phytoplankton community structure at the surface (< 20m) showed high interannual variability and is impacted by sampling timing and physical forcing. Diatoms favor cold turbulent environments (Margalef 1978) while dinoflagellates and *Phaeocystis spp.* thrive in warmer and saltier stratified waters. Outside the bloom period, small flagellates contribute more significantly to total biomass and samples show higher phytoplankton diversity (Fragoso et al. 2017; Devred et al. 2025).

The highest fraction of total biomass is comprised of diatoms, with mean contributions of 58.5%, 45.8%, and 66% for AR7W-W, AR7W-C and, AR7W-E respectively. Diatoms show large interannual variability in all regions. In 2025, their percent contribution was above average in AR7W-W, a trend observed since 2019 except for 2024 which was below average. AR7W-C and AR7W-E saw below average percent contribution in 2025.

Dinoflagellates showed below-normal anomalies in all regions since 2014 except in the AR7W-C region in 2019, 2023, and 2025, and in the AR7W-W in 2016. The current method of taxonomic grouping only accounts for peridinin-containing dinoflagellates, which might explain the small contribution of this taxonomic group to total biomass.

Phaeocystis spp. is known to occur mainly at the Greenland shelf break and eastern central basin (Fragoso et al. 2017) as reflected in the average values observed over the entire time series (23.4% and 20.1% of total biomass for AR7W-C and AR7W-E respectively, and only 5.6% in the AR7W-W). Three major *Phaeocystis spp.* blooms occurred in 2004, 2014, and 2015, which covered a large surface area of the Labrador Sea, as well as three smaller but significant blooms in 2006, 2008, and 2023 in the AR7W-E region. Notably, during the large *Phaeocystis spp.* bloom in 2015 that resulted in record high anomalies over all regions, all other groups exhibited below-normal anomalies, with a record low percentage contribution of diatoms in AR7W-E. In 2025, *Phaeocystis spp.* contribution to total biomass was near but slightly below

normal. The positive sea-ice anomaly around the Greenland coast in 2025 (Figure 8) may explain the lower contribution of *Phaeocystis spp.* in the AR7W-E since this taxonomic group favors warmer and saltier waters (Devred et al. 2025).

The “other phytoplankton” category comprises small flagellates. This group contributed 35% of the total biomass on average from 2001-2025 in the AR7W-W, and 29.2% in the AR7W-C, the second largest percentage contribution after diatoms in these two regions. In the AR7W-E, the average percentage contribution of this group was 13.7%, the third largest after diatoms and *Phaeocystis spp.* This group experienced high interannual variability, with near normal or negative anomalies over the period from 2019 to 2024 across all regions, except for a high positive anomaly in AR7W-W. In 2025, AR7W-W saw a below average anomaly, and AR7W-C and AR7W-E saw record high anomalies, a pattern in contrast to the percent contribution of diatoms in 2025.

3.3.5 Phytoplankton Apparent Absorption Wavelength

PAAW is a measure of phytoplankton colour and biomass. Higher values, indicated by red in Figure 31, occur when the spectral shape of the phytoplankton absorption curve is flatter (Devred et al. 2022). A shift in anomaly patterns could indicate a shift in community structure, though it might be more the result of sample timing than a change in the properties of the ecosystem.

The mean PAAW were similar in AR7W-W and AR7W-C (477 nm), and slightly higher in AR7W-E (480 nm). Up to 2007, PAAW anomalies were predominantly negative, but the period from 2008 to 2019 saw variability between lower and higher than normal PAAW with no clear pattern, unlike integrated chl-a. Since 2022 PAAW anomalies have been mainly positive, indicating a possible increase in phytoplankton biomass with a change of structure toward larger cells. In 2025, PAAW showed a higher than normal anomaly in AR7W-W, and near-normal anomalies in the other regions. This anomaly pattern is positively correlated with the percent contribution of diatoms and negatively correlated with the percent contribution of “other” (smaller) phytoplankton (Figure 30).

3.3.6 Satellite-derived chlorophyll-a concentration and bloom metrics

Satellite-derived chl-a allows observation of the Labrador Sea all year long, but is limited by sea ice and cloud cover. The main advantage of the satellite is that information on phytoplankton biomass and spring bloom timing can be reported when sea-going missions have been cancelled or delayed. Here we report on the timing of the spring and fall blooms, and the annual and seasonal mean chl-a in the three regions of interest.

The timing of the spring bloom peak is highly variable and depends on several factors, including the thermal stratification, the amount of nutrients, the light available for photosynthesis, and the grazing pressure. The spring bloom generally occurs first in AR7W-E (day of year (doy) 139 on average), then in AR7W-W (doy 154 on average) and shortly after in AR7W-C (doy 166 on average) (Figure 32), likely driven by sea-ice dynamics (Cyr et al. 2024).

AR7W-W spring bloom peak timing has typically been near normal or early since 2003, with the exception of 2007, 2009, and the second latest bloom on record in 2018. AR7W-E bloom timing has also been near normal or early for most of the time series (2000 to 2021) except for a record late bloom in 2008, and late blooms since 2023. AR7W-C has experienced periods of early or late blooms (late from 2000-2005, early from 2006-2015 with the exception of 2009 and 2011, late again from 2016-2021, and early since 2022). In 2025, slightly early blooms occurred in AR7W-W and AR7W-C and a later bloom occurred in AR7W-E.

A secondary bloom occurs in the fall, less intense than the spring one, triggered by the replenishment in nutrients of the surface-lit layer by storm-induced vertical mixing when light is still sufficient to stimulate phytoplankton productivity. The average fall bloom timing across the climatology follows similar patterns over the region as the spring bloom timing (i.e. AR7W-E bloom first at doy 248, AR7W-W second at doy 256, and AR7W-C last at doy 260). AR7W-W has seen typically late fall blooms since 2015, and a record late bloom in 2024 (anomaly of +1.79). AR7W-C and AR7W-E fall bloom timings have been highly variable over the time series. In 2025, AR7W-W saw the second latest bloom on record, while the timing was near-normal in AR7W-C and slightly early in AR7W-E.

The drivers of total annual production differ in each region. In AR7W-W, both the spring and fall chl-a average anomalies are highly correlated with the annual average anomalies (r=0.84 and 0.7, respectively, Figure 33). In AR7W-E, annual production is driven by the spring bloom alone (r=0.75). In AR7W-C, however, significant production occurs during all non-winter months, with spring, summer, and fall chl-a averages showing correlations of r=0.97, 0.72, and 0.68 with annual average chl-a. The mean annual and seasonal chl-a show high interannual variability, with a notable increase in the number of high positive chl-a anomalies across all seasons over the past decade. In 2025, mean annual and spring chl-a were below normal and winter saw near-normal anomalies in all regions. AR7W-C saw an increase in chl-a later in the year in summer and fall with positive anomalies, while AR7W-E chl-a remained below average, and AR7W-W was near normal.

3.3.7 Mesozooplankton

Mesozooplankton abundances from the 2025 mission will be available at a later date.

C. finmarchicus copepods dominate the mesozooplankton biomass in AR7W-C, while they and their congeners *C. glacialis* and *C. hyperboreus* contribute about one third each of total biomass on the shelves (AR7W-W and AR7W-E) (Head et al. 2003). *C. finmarchicus* total abundance is greatly influenced by the abundance of young stage copepodites, which develop from eggs laid by overwintering pre-adults in the deep central basin that have re-ascended in spring. The phytoplankton spring bloom provides the fuel required for egg-laying individuals and the development of nauplii and young copepodite stages, so that regional differences in spring bloom dynamics impact the timing of the development of *C. finmarchicus* populations. Since spring blooms are generally earlier and more intense in AR7W-E than in the other regions, *C. finmarchicus* abundance is generally higher in AR7W-E than in other regions of the Labrador Sea at the time of sampling (Figure 34). Young stages become abundant later in the season, following the phytoplankton bloom that triggered and sustained egg production (Head et al. 2015). There was no trend in spring total abundance for *C. finmarchicus* between 1997 and 2024. In general, abundances remained slightly below or near normal except for a few years where abundance was above normal (e.g., AR7W-C in 2007, 2018 and 2024). Record high level anomalies occurred in 2024 in both AR7W-W and AR7W-C, and 2006 in AR7W-E, mostly due to the large number of younger stages, which is reflected in the above average anomalies of the corresponding %PDI typical of post-phytoplankton bloom sampling.

High climatological abundance of *C. glacialis* and *C. hyperboreus* in AR7W-W (2×10^3 and 4×10^3 individuals per m^2, respectively) and AR7W-E (2×10^3 and 3×10^3 individuals per m^2) compared to AR7W-C (2×10^2 and 1×10^3 individuals per m^2) may result from the transport of individuals in the inflows, since neither species have a local source of overwintering population. The abundance of both species has generally shown considerable year-to-year variability, with the exception of sustained periods of low abundance from 2014 to 2016 and high abundance of *C. hyperboreus* in AR7W-E between 2009 and 2012 (Figure 34).

Both AR7W-C and AR7W-E have shown close to normal or high abundances of *Pseudocalanus spp.* since 2022 (Figure 34). The AR7W-C showed record high abundance in 2022, and the second highest abundance in 2024. As a result of changing the climatological period since the report on the 2024 conditions (1999-2020, Clay et al. (2026), now 1999-2025), the AR7W-C now generally shows below or close-to-normal *Pseudocalanus spp.* abundance between 1999 and 2019.

Oithona spp. abundances were generally near or below normal up to 2004 (Figure 34) followed by a period of high variability from 2005 to 2013. They remained persistently less abundant than average from 2014 to 2019, but rebounded in 2022 in AR7W-W and have remained above-average since, while abundance in AR7W-C and AR7W-E remained near or below average in 2022 and 2023 followed by record-high abundances in 2024.

Up to 2013, *Euphausiid* showed a large interannual variability in the three regions of interest (Figure 34). *Euphausiid*, like *Oithona*, also experienced a period of low abundances from 2014 to 2019, followed by above average abundances since 2022 in AR7W-W, variable abundances in AR7W-C, and near to below normal abundances in AR7W-E in 2022 and 2023. Record high abundances occurred in all three regions in 2024.

Amphipoda, mostly represented here by *Themisto libellula*, showed lower-than-average abundances throughout the Labrador Sea since 2019, following a decade-long period of higher interannual variability.

4 SUMMARY

The Atlantic Zone Off-Shelf Monitoring Program (AZOMP) provides observations on ocean climate and plankton variability within the Labrador Sea and adjacent shelves affecting ecosystems of Atlantic Canada and the climate at both regional and global scales. In the Labrador Sea, surface heat losses in winter result in the formation of dense waters, which spread across the ocean, ventilating the deep layers, thus contributing to the global ocean-overturning circulation. Occupation of the monitoring line is time and season sensitive. Therefore, interpretation of the data should take into consideration the timing of sampling and its impact on physical, chemical and biological processes. This year the occupation of AR7W happened around the time of the spring bloom initiation (Figure 2).

The winter (January to March) NAO index in 2025 was slightly below normal. In the central Labrador Sea in 2025, winter had the highest air temperature anomaly with 1.0 °C above normal, and summer had an anomaly of 0.7 °C below normal. The winter, spring, and summer SST anomalies in the central Labrador Sea (derived from the HadISST product) were below normal (winter: -0.08 °C, spring: -0.36 °C, and summer: -0.42 °C), and fall anomalies were above normal (0.32 °C). Sea ice extent and concentration anomalies in the winter of 2025 were generally negative for the Labrador shelf. In 2025, data retrieved from Argo profilers revealed that the temperature anomalies relative to the 2002-2020 reference period in the Labrador Sea for three layers (100-500 dbar, 500-1000 dbar, and 1000-2000 dbar) were mostly positive (warm), and the salinity anomalies were variable, with fresher waters in the central basin and saltier waters along the Greenland Shelf. The analysis of the AR7W temperature and salinity data from CTD profiles collected during the 2025 mission indicated that the winter convection in the Labrador Sea reached about 450 m, and calculation of the MLD using Argo profiles yielded a median MLD of approximately 400 m. Current transport along the Labrador Slope was above normal (positive southeastward), but below normal along the Labrador Shelf.

The concentration of CFC-12 rose slightly between 2024 and 2025 to approximately 2.3 $\mathrm{pmol\ kg^{-1}}$. SF_6 concentration continued decreasing after its peak in 2023. DIC concentrations

from the NV-LSW in the central Labrador Sea have continued to increase as in previous years (0.87 $\mu mol\ kg^{-1}\ y^{-1}$ from 1996 to 2025). The increase resulted in pH levels continuing their declining trend (0.003 pH units per year). Observations in Winkler oxygen measurements and Argo floats found oxygen concentrations were slightly above normal in the NV-LSW and slightly below normal in the NEADW in 2025.

In 2025, average surface layer temperature (0-100 m) derived from CTD measurements taken in conjunction with water samples was slightly below normal in all regions. Negative anomalies of all surface and deep nutrient concentrations were observed in AR7W-W, a trend that began in 2019. AR7W-C and AR7W-E saw high positive anomalies of all surface and deep nutrients with the exception of deep phosphate in AR7W-C, breaking the trend of below-average nutrients that were observed in these regions since 2019 (except for surface silicate in AR7W-E). Deep nitrate and silicate concentrations in AR7W-E saw record positive anomalies. Chl-a concentrations showed negative anomalies in 2025 in AR7W-C and AR7W-E and a high positive anomaly in AR7W-W, measured using Turner fluorometry in the top 100 m of the water column. Surface chl-a (i.e. less than 20 m depth, measured using HPLC) confirmed these anomaly patterns over the region. Diatom contribution to total biomass was lower than normal in AR7W-C and AR7W-E and above normal in AR7W-W. Dinoflagellate and *Phaeocystis spp.* contributions were near or slightly lower than normal in all three regions. Other phytoplankton showed a lower than normal percentage contribution in AR7W-W and higher than normal in AR7W-C and AR7W-E, in contrast to diatom contributions. The PAAW metric (an indicator of the shape of the phytoplankton absorption spectrum) showed positive anomalies on the shelves (AR7W-W and AR7W-E), with the AR7W-W seeing the second highest anomaly on record, and AR7W-E near normal. PAAW was slightly below average in AR7W-C in 2025. Satellite ocean colour data revealed the spring bloom was early in AR7W-W and AR7W-C and late in AR7W-E. In contrast, the fall bloom was late in AR7W-W and AR7W-C and early in AR7W-E. Mean annual surface chl-a derived from satellite data was near or below normal in all regions throughout the year, except for summer and fall in AR7W-C when it was above normal. Mesozooplankton abundances from the 2025 mission are not yet available.

5 ACKNOWLEDGEMENTS

The authors thank the sea-going and land-based support staff of the Bedford Institute of Oceanography, the TCA *Uncertain-Sea* Team, and officers and crew of the of the *R.O. L'Atalante* for their enthusiasm toward our monitoring program, and Robert Benjamin, Diana Cardoso, and Flo Hum for their support with data management and data sharing. We would also like to thank the two DFO reviewers for providing many helpful comments.

6 REFERENCES

Astthorsson, O.S., and Gislason, A. 2003. Seasonal variations in abundance, development and vertical distribution of Calanus finmarchicus, C. hyperboreus and C. glacialis in the East Icelandic Current. Journal of Plankton Research 25(7): 843–854.

Azetsu-Scott, K., Jones, E. P., Yashayaev, I., and Gershey, R.M. 2003. Time series study of CFC concentrations in the Labrador Sea during deep and shallow convection regimes (1991–2000). Journal of Geophysical Research: Oceans 108(C11).

Azetsu-Scott, K., Clarke, A., Falkner, K., Hamilton, J., Jones, E. P., Lee, C., Petrie, B., Prinsenberg, S., Starr, M., and Yeats, P. 2010. Calcium carbonate saturation states in the waters of the Canadian Arctic Archipelago and the Labrador Sea. Journal of Geophysical Research 115(C11021).

Barnston, A. G., and Livezey, R.E. 1987. Classification, seasonality and persistence of low-frequency atmospheric circulation patterns. Monthly Weather Review 115(6): 1083–1126. American Meteorological Society, Boston MA, USA.

Barrett, R. C., Carter, B. R., Fassbender, A. J., Tilbrook, B., Woosley, R. J., Azetsu-Scott, K., Feely, R. A., Goyet, C., Ishii, M., Murata, A., and Pérez, F.F. 2025. Biological responses to ocean acidification are changing the global ocean carbon cycle. Global Biogeochemical Cycles 39(3): e2024GB008358.

Becker, S., Aoyama, M., Woodward, E. M. S., Bakker, K., Coverly, S., Mahaffey, C., and Tanhua, T. 2020. GO-SHIP repeat hydrography nutrient manual: The precise and accurate determination of dissolved inorganic nutrients in seawater, using continuous flow analysis methods. Frontiers in Marine Science 7: 581790.

Bélanger, D., Clay, S., Blais, M., and Devred, E. in prep. Ocean colour derived metrics for reporting on Northwest Atlantic phytoplankton phenology and interannual variability. XXX. Can. Tech. Rep. Hydrogr. Ocean Sci. XXX: vii + p.

Bélanger, S., Ehn, J.K., and Babin, M. 2007. Impact of sea ice on the retrieval of water-leaving reflectance, chlorophyll a concentration and inherent optical properties from satellite ocean color data. Remote Sensing Env. 111(1): 51–68.

Caldeira, K., and Wickett, M.E. 2003. Anthropogenic carbon and ocean pH. Nature 425: 365.

Cavalieri, D., Parkinson, C., Gloersen, P., and Zwally, H. 1996. Sea ice concentrations from nimbus-7 SMMR and DMSP SSM/i-SSMIS passive microwave data, version 1. NASA National Snow; Ice Data Center Distributed Active Archive Center.

Clay, S., Peña, A., DeTracey, B., and Devred, E. 2019. Evaluation of satellite-based algorithms to retrieve Chlorophyll-a concentration in the Canadian Atlantic and Pacific oceans. Remote Sens. 11(22).

Clay, S., Layton, C., and Devred, E. 2021. PhytoFit: First release (v1.0.0).

Clay, S., Ringuette, M., Devred, E., Azetsu-Scott, K., Wang, Z., Greenan, B., Gordon, C., Gabriel, C. E., Childs, D., and Layton, C. 2026. Physical, Chemical, Biological, and Optical Oceanographic Conditions in the Labrador Sea in 2024. 3752. Can. Tech. Rep. Fish. Aquat. Sci. 3752: vii + 58 p.

Cyr, F., Lewis, K., Bélanger, D., Regular, P., Clay, S., and Devred, E. 2024. Physical controls and ecological implications of the timing of the spring phytoplankton bloom on the Newfoundland and Labrador shelf. Limnology and Oceanography Letters 9(3): 191–198.

Devred, E., Perry, T., and Massicotte, P. 2022. Seasonal and decadal variations in absorption properties of phytoplankton and non-algal particulate matter in three oceanic regimes of the Northwest Atlantic. Frontiers in Marine Science Volume 9 - 2022.

Devred, E., Wilson, K. L., Perry, T., Hardy, M., Brosnahan, M., and Ringuette, M. 2024. Identification and validation of phytoplankton taxonomic assemblages derived from pigment signatures using samples collected in the Labrador Sea from 2014 to 2022. 3596. Can. Tech. Rep. Fish. Aquat. Sci. 3596: viii + 55 p.

Devred, E., Clay, S., Ringuette, M., Perry, T., Amirian, M., Irwin, A., and Finkel, Z. 2025. Net primary production in the Labrador Sea between 2014 and 2022 derived from ocean colour remote sensing based on ecological regimes. Remote Sensing of Environment 323: 114713.

Dickson, A. G., Sabine, C. L., and Christian, J.R.(Eds.). 2007. Guide to best practices for ocean CO2 measurements. PICES Special Publication 3.

Elzhov, T.V., Mullen, K.M., Spiess, A.-N., and Bolker, B. 2023. Minpack.lm: R interface to the levenberg-marquardt nonlinear least-squares algorithm found in MINPACK, plus support for bounds.

E.U. Copernicus Marine Service Information. 2026. Global ocean gridded L4 sea surface heights and derived variables reprocessed. Marine Data Store (MDS).

Feely, R. A., Sabine, C. L., Lee, K., Berelson, W., Kleypas, J., Fabry, V. J., and Millero, F.J. 2004. Impact of anthropogenic CO2 on the CaCO3 system in the oceans. Science 305(5682): 362–366.

Fetterer, F., Knowles K., Meier W., Savoie M., and A., W. 2017. Sea ice index, version 3. NSIDC.

Fragoso, G. M., Poulton, A. J., Yashayaev, I. M., Head, E.J.H., Stinchcombe, M. C., and Purdie, D.A. 2016. Biogeographical patterns and environmental controls of phytoplankton communities from contrasting hydrographical zones of the Labrador Sea. Progress in Oceanography 141: 212–226.

Fragoso, G.M., Poulton, A.J., Yashayaev, I.M., Head, E.J.H., and Purdie, D.A. 2017. Spring phytoplankton communities of the Labrador Sea (2005–2014): Pigment signatures, photophysiology and elemental ratios. Biogeosciences 14(5): 1235–1259.

Haine, T. W. N., and Hall, T.M. 2002. A generalized transport theory: Water-mass composition and age. Journal of Physical Oceanography 32(6): 1932–1946.

Hall, T. M., Haine, T. W. N., and Waugh, D.W. 2002. Inferring the concentration of anthropogenic carbon in the ocean from tracers. Global Biogeochemical Cycles 16(4): 1131.

Han, G., Lu, Z., Wang, Z., Helbig, J., Chen, N., and deYoung, B. 2008. Seasonal variability of the Labrador Current and shelf circulation off Newfoundland. Journal of Geophysical Research: Oceans 113(C10).

Harrison, W. G., and Li, W.K.W. 2008. Phytoplankton growth and regulation in the Labrador Sea: Light and nutrient limitation. Journal of Northwest Atlantic Fishery Science 39: 71–82.

Hauser, T., Demirov, E., Zhu, J., and Yashayaev, I. 2015. North atlantic atmospheric and ocean inter-annual variability over the past fifty years - dominant patterns and decadal shifts. Progress in Oceanography 132: 197–219.

Hayward, A., Pinkerton, M. H., and Gutierrez-Rodriguez, A. 2023. Phytoclass: A pigment-based chemotaxonomic method to determine the biomass of phytoplankton classes. Limnology and Oceanography: Methods 21(4): 220–241.

Head, E. J. H., and Horne, E.P.W. 1993. Pigment transformation and vertical flux in an area of convergence in the North Atlantic. Deep Sea Research Part II: Topical Studies in Oceanography 40(1): 329–346.

Head, E. J. H., Harris, L. R., and Yashayaev, I. 2003. Distributions of Calanus spp. And other mesozooplankton in the Labrador Sea in relation to hydrography in spring and summer (1995–2000). Progress In Oceanography 59(1): 1–30.

Head, E. J. H., Azetsu-Scott, K., Harrison, G., Hendry, R., Li, W., Yashayaev, I., and Yeats, P. 2008. Changes in environmental conditions and the population dynamics of Calanus finmarchicus in the Labrador Sea (1990-2006).

Head, E. J. H., Gentleman, W. C., and Ringuette, M. 2015. Variability of mortality rates for Calanus finmarchicus early life stages in the Labrador Sea and the significance of egg viability. Journal of Plankton Research 37(6): 1149–1165.

Holm-Hansen, O., Lorenzen, C. J., Holmes, R. W., and Strickland, J.D.H. 1965. Fluorometric determination of chlorophyll. ICES Journal of Marine Science 30(1): 3–15.

Hood, E. M., Sabine, C. L., and Sloyan, B.M.(Eds.). 2010. The GO-SHIP repeat hydrography manual: A collection of expert reports and guidelines, version 1. (IOCCP Report 14), (ICPO Publication Series 134).

Hurrell, J.W. 1995. Decadal trends in the North Atlantic Oscillation: Regional temperatures and precipitation. Science (New York, N.Y.) 269: 676–9.

Johnson, K. M., Sieburth, J.McN., Williams, P. J.leB., and Brändström, L. 1987. Coulometric total carbon dioxide analysis for marine studies: Automation and calibration. Marine Chemistry 21(2): 117–133.

Jones, P. D., and Hulme, M. 1996. Calculating regional climatic time series for temperature and precipitation: Methods and illustrations. International Journal of Climatology 16(4): 361–377.

Kalnay, E., Kanamitsu, M., Kistler, R., Collins, W., Deaven, D., Gandin, L., Iredell, M., Saha, S., White, G., Woollen, J., Zhu, Y., Chelliah, M., Ebisuzaki, W., Higgins, W., Janowiak, J., Mo, K. C., Ropelewski, C., Wang, J., Leetmaa, A., Reynolds, R., Jenne, R., and Joseph, D. 1996. The NCEP/NCAR 40-year reanalysis project. Bulletin of the American Meteorological Society 77(3): 437–472. American Meteorological Society, Boston MA, USA.

Kam, K., Atamanchuk, D., Devred, E., and Wallace, D. 2024. Estimates of the biological carbon pump from in-situ data and satellite remote sensing in the center Labrador Sea. *In* American geophysical union, ocean sciences meeting. pp. OB42B–03.

Kérouel, R., and Aminot, A. 1997. Fluorometric determination of ammonia in sea and estuarine waters by direct segmented flow analysis. Marine Chemistry 57(3): 265–275.

Langdon, C. 2010. Determination of dissolved oxygen in seawater by winkler titration using the amperometric technique. : 18pp.

Lauvset, S. K., and Tanhua, T. 2015. A toolbox for secondary quality control on ocean chemistry and hydrographic data. Limnology and Oceanography: Methods 13(11): 601–608.

Layton, C., Devred, E., and Detracey, B. 2022. A comparison of phytoplankton spring bloom fitting methods using MODIS satellite-derived chlorophyll-a concentration for the Maritimes region. 340. Can. Tech. Rep. Hydrogr. Ocean Sci. 340: vii + 22p.

Layton, C., Greenan, B., and Wang, Z. 2026. Atlantic Repeat Hydrography Line 7 West 1991 to 2020 Hydrographic Climatology. Can. Data Rep. Hydrogr. Ocean Sci. 231: v + 44 p.

Leist, L. G. T., Castrillejo, M., Azetsu-Scott, K., Lee, C., Lenetsky, J., Ringuette, M., Vockenhuber, C., Pérez-Tribouilier, H., and Casacuberta, N. 2026. Radionuclide tracers reveal new Arctic pathways shaping water mass mixing and formation in Baffin Bay and Labrador Sea (in revision).

Lewis, E., Wallace, D., and Allison, L.J. 1998. Program developed for CO2 system calculations. Brookhaven National Lab., Dept. of Applied Science, Upton, NY (United States); Oak Ridge National Lab., Carbon Dioxide Information Analysis Center, TN (United States).
Li, F., Fu, Y., Tillys, P., and Zou, S. 2026. Strengthening of Labrador Sea overturning linked to subsurface freshening over recent decades. Geophysical Research Letters 53.
Li, W. K. W., and Harrison, W.G. 2014. The state of phytoplankton and bacterioplankton in the Labrador Sea: Atlantic Zone Off-Shelf Monitoring Program 1994–2013. 302. Can. Tech. Rep. Hydrogr. Ocean. Sci. 302: xviii + 181p.
Loder, J. W., and Wang, Z. 2015. Trends and variability of sea surface temperature in the Northwest Atlantic from three historical gridded datasets. Atmosphere-Ocean 53(5): 510–528. Taylor & Francis.
Lozier, M. S., Li, F., Bacon, S., Bahr, F., Bower, A., Cunningham, S., De Jong, M. F., Steur, de, L., Deyoung, B., Fischer, J., Gary, S., Greenan, B., Holliday, N., Houk, A., Houpert, L., Inall, M., Johns, W., Johnson, H., Johnson, C., and Zhao, J. 2019. A sea change in our view of overturning in the subpolar North Atlantic. Science 363(6426): 516–521.
Lueker, T. J., Dickson, A. G., and Keeling, C.D. 2000. Ocean pCO2 calculated from dissolved inorganic carbon, alkalinity, and equations for K1 and K2: Validation based on laboratory measurements of CO2 in gas and seawater at equilibrium. Marine Chemistry 70(1): 105–119.
Margalef, R. 1978. Life-forms of phytoplankton as survival alternatives in an unstable environment. Oceanologica Acta 1(4): 493–509. Article.
Maze, G., and Balem, K. 2020. Argopy: A python library for argo ocean data analysis. Journal of Open Source Software 5(53): 2425. The Open Journal.
McKinley, G. 2025. Revised estimates of CO2 sources and sinks improve global carbon accounting. Nature 649.
Mitchell, M. R., Harrison, G., Pauley, K., Gagné, A., Maillet, G., and Strain, P. 2002. Atlantic Zonal Monitoring Program sampling protocol.
Neeley, A., Mannino, A., Boss, E., D'Sa, E., Freeman, S., Fry, E., Mueller, J., Pegau, W., Reynolds, R., Roesler, C., Röttgers, R., Stramski, D., Twardowski, M., Ronald, J., and Zaneveld, V. 2018, November. IOCCG Protocol Series ocean optics & biogeochemistry protocols for satellite ocean colour sensor validation, volume 1: Inherent optical property measurements and protocols: Absorption coefficient (v1.0).
O'Reilly, J. E., Maritorena, S., Mitchell, B. G., Siegel, D. A., Carder, K. L., Garver, S. A., Kahru, M., and McClain, C. 1998. Ocean color chlorophyll algorithm for SeaWiFS. J. Geophys. Res. 103: 937–953.
Patel, R. 2025. To compute Mixed Layer Depth based on subjective method. MATLAB Central File Exchange.
Platt, T., and Jassby, A.D. 1976. The relationship between photosynthesis and light for natural assemblages of coastal marine phytoplankton. Journal of Phycology 12: 421–430.
Pollara, S., Jabre, L., Rowland, E., Roberts, M., Stevens-Green, R., LaRoche, J., McBride, C., Sipler, R. E., Healey, M., Roca-Marti, M., Kienast, S., Devred, E., Ward, B., and Bertrand, E.M. 2024. Examining drivers of biological carbon export in the Labrador Sea using metaproteomics-based assessments of primary production potential and microbial metabolism. *In* American geophysical union, ocean sciences meeting. pp. OB42B–08.
Punshon, S., Childs, D., and Azetsu-Scott, K. 2016. A purge-and-trap gas chromatographic method for shipboard determination of the transient tracers sulphur hexafluoride and

dichlorodifluoromethane in seawater and in air. Can. Tech. Rep. Hydrogr. Ocean Sci. 309: vii + 21p.
Punshon, S., Azetsu-Scott, K., Sherwood, O., and Edinger, E.N. 2019. Bottom water methane sources along the high latitude eastern Canadian continental shelf and their effects on the marine carbonate system. Marine Chemistry 212: 83–95.
R Core Team. 2022. R: A language and environment for statistical computing. R Foundation for Statistical Computing, Vienna, Austria.
Raimondi, L., Matthews, J. B. R., Atamanchuk, D., Azetsu-Scott, K., and Wallace, D.W.R. 2019. The internal consistency of the marine carbon dioxide system for high latitude shipboard and in situ monitoring. Marine Chemistry 213: 49–70.
Raimondi, L., Tanhua, T., Azetsu-Scott, K., Yashayaev, I., and Wallace, D.W.R. 2021. A 30-year time series of transient tracer-based estimates of anthropogenic carbon in the central Labrador Sea. Journal of Geophysical Research: Oceans 126(5): e2020JC017092.
Rayner, N. A., Parker, D. E., Horton, E. B., Folland, C. K., Alexander, L. V., Rowell, D. P., Kent, E. C., and Kaplan, A. 2003. Global analyses of sea surface temperature, sea ice, and night marine air temperature since the late nineteenth century. Journal of Geophysical Research: Atmospheres 108(D14).
Reed, M., Strope, E., Cremona, F., Myers, J., Newell, S., and McCarthy, M. 2022. Effects of filtration timing and pore size on measured nutrient concentrations in environmental water samples. Limnology and Oceanography: Methods 21.
Roy, S., Llewellyn, C. A., Egeland, E. S., and Johnsen, G. (*Editors*). 2011. Phytoplankton Pigments: Characterization, Chemotaxonomy and Applications in Oceanography. *In* 2nd edition. Cambridge University Press, Cambridge, UK.
Sabine, C. L., Feely, R. A., Gruber, N., Key, R. M., Lee, K., Bullister, J. L., Wanninkhof, R., Wong, C. S., Wallace, D. W. R., Tilbrook, B., Millero, F. J., Peng, T.-H., Kozyr, A., Ono, T., and Rios, A.F. 2004. The oceanic sink for anthropogenic CO2. Science 305(5682): 367–371.
Sathyendranath, S., Brewin, R. J. W., Brockmann, C., Brotas, V., Calton, B., Chuprin, A., Cipollini, P., Couto, A. B., Dingle, J., Doerffer, R., Donlon, C., Dowell, M., Farman, A., Grant, M., Groom, S., Horseman, A., Jackson, T., Krasemann, H., Lavender, S., Martinez-Vicente, V., Mazeran, C., Mélin, F., Moore, T. S., Müller, D., Regner, P., Roy, S., Steele, C. J., Steinmetz, F., Swinton, J., Taberner, M., Thompson, A., Valente, A., Zühlke, M., Brando, V. E., Feng, H., Feldman, G., Franz, B. A., Frouin, R., Gould, R. W., Hooker, S. B., Kahru, M., Kratzer, S., Mitchell, B. G., Muller-Karger, F. E., Sosik, H. M., Voss, K. J., Werdell, J., and Platt, T. 2019. An ocean-colour time series for use in climate studies: The experience of the ocean-colour climate change initiative (OC-CCI). Sensors 19(19).
Sathyendranath, S., Jackson, T., Brockmann, C., Brotas, V., Calton, B., Chuprin, A., Clements, O., Cipollini, P., Danne, O., Dingle, J., Donlon, C., Grant, M., Groom, S., Krasemann, H., Lavender, S., Mazeran, C., Mélin, F., Müller, D., Steinmetz, F., Valente, A., Zühlke, M., Feldman, G., Franz, B., Frouin, R., Werdell, J., and Platt, T. 2023. ESA ocean colour climate change initiative (ocean_colour_cci): Monthly climatology of global ocean colour data products at 4km resolution. NERC EDS Centre for Environmental Data Analysis.
Schiller-Weiss, I., Martin, T., and Schwarzkopf, F.U. 2024. Emerging influence of enhanced Greenland melting on boundary currents and deep convection regimes in the Labrador and Irminger Seas. Geophysical Research Letters 51(9): e2024GL109022.

Stramski, D., Reynolds, R., Kaczmarek, S., Uitz, J., and Zheng, G. 2015. Correction of pathlength amplification in the filter-pad technique for measurements of particulate absorption coefficient in the visible spectral region. Applied Optics 54: 6763–6782.
Stuart, V., and Head, E.J.H. 2005. The BIO method. In The Second SeaWiFS HPLC Analysis Round-Robin Experiment (SeaHARRE-2), ed. S. B. Hooker (NASA/TM 2005-212785, Greenbelt, Maryland). : 112.
Twedt, K., Xiong, X., Geng, X., Wilson, T., and Mu, Q. 2023. Impact of satellite orbit drift on MODIS earth scene observations used in calibration of the reflective solar bands. p. 24.
Visbeck, M. H., Hurrell, J. W., Polvani, L., and Cullen, H.M. 2001. The North Atlantic Oscillation: Past, present, and future. Proceedings of the National Academy of Sciences 98(23): 12876–12877.
Wang, Z., Yashayaev, I., and Greenan, B. 2015. Seasonality of the inshore labrador current over the newfoundland shelf. Continental Shelf Research 100: 1–10.
Wang, Z., Brickman, D., Greenan, B. J. W., and Yashayaev, I. 2016. An abrupt shift in the Labrador Current System in relation to winter NAO events. Journal of Geophysical Research: Oceans 121(7): 5338–5349.
Wang, Z., Brickman, D., and Greenan, B.J.W. 2019. Characteristic evolution of the Atlantic Meridional Overturning Circulation from 1990 to 2015: An eddy-resolving ocean model study. Deep Sea Research Part I: Oceanographic Research Papers 149: 103056.
Wang, Z., Yang, J., Johnson, C., and DeTracey, B. 2022. Changes in deep ocean contribute to a "see-sawing" Gulf Stream path. Geophysical Research Letters 49(21): e2022GL100937.
Welschmeyer, N.A. 1994. Fluorometric analysis of chlorophyll a in the presence of chlorophyll b and pheopigments. Limnology and Oceanography 39(8): 1985–1992.
Wong, A. P., Wijffels, S. E., Riser, S. C., Pouliquen, S., Hosoda, S., Roemmich, D., Gilson, J., Johnson, G. C., Martini, K., Murphy, D. J., and al., et. 2020. Argo data 1999-2019: Two million temperature-salinity profiles and subsurface velocity observations from a global array of profiling floats. Frontiers in Marine Science 7.
Yamaguchi, R., and Suga, T. 2019. Trend and Variability in Global Upper-Ocean Stratification Since the 1960s. Journal of Geophysical Research: Oceans 124(12): 8933–8948.
Yashayaev, I. 2007. Hydrographic changes in the Labrador Sea, 1960–2005. Progress in Oceanography 73(3): 242–276.
Yashayaev, I. 2024. Intensification and shutdown of deep convection in the Labrador Sea were caused by changes in atmospheric and freshwater dynamics. Communications Earth & Environment 5.
Yashayaev, I., and Loder, J.W. 2009. Enhanced production of Labrador Sea Water in 2008. Geophys. Res. Lett. 36(1): L01606.
Yashayaev, I., and Loder, J.W. 2016. Recurrent replenishment of labrador sea water and associated decadal-scale variability. Journal of Geophysical Research: Oceans 121(11): 8095–8114.
Yashayaev, I., and Loder, J.W. 2017. Further intensification of deep convection in the Labrador Sea in 2016. Geophysical Research Letters 44(3): 1429–1438.
Yashayaev, I., Peterson, I., and Wang, Z. 2021. Meteorological, sea ice and physical oceanographic conditions in the Labrador Sea during 2018. 42. DFO Can. Sci. Advis. Sec. Res. Doc. 2021/042. iv + 26 p.

Yebra, L., Harris, R. P., Head, E. J. H., Yashayaev, I., Harris, L. R., and Hirst, A.G. 2009. Mesoscale physical variability affects zooplankton production in the Labrador Sea. Deep Sea Research Part I: Oceanographic Research Papers 56(5): 703–715.

Yentsch, C.S., and Menzel, D.W. 1963. A method for the determination of phytoplankton chlorophyll and phaeophytin by fluorescence. Deep Sea Research 10(3): 221–231.

7 TABLES

Table 1. Links to data sources used in this report.

Data	Link	Date accessed
Winter NAO	https://psl.noaa.gov/data/climateindices	15 Jan 2026
Air temperature	http://ftp.cdc.noaa.gov	10 Jan 2026
SST (HadISST)	https://www.metoffice.gov.uk/hadobs/hadisst/data/download.html	26 Feb 2026
Sea Ice	https://nsidc.org/data/g02135/versions/3	11 Mar 2026
Satellite altimetry data	https://data.marine.copernicus.eu/product/SEALEVEL_GLO_PHY_L4_MY_008_047	05 May 2026
Argo floats	https://argo.ucsd.edu	21 May 2026
Tracers, TIC, pH, and dissolved oxygen	https://www.ncei.noaa.gov/products/ocean-carbon-acidification-data-system	13 Mar 2026
Satellite ocean colour info	http://climate.esa.int/en/projects/ocean-colour	26 Feb 2026
Satellite ocean colour data	https://www.oceancolour.org	26 Feb 2026
Satellite bloom metrics	https://github.com/BIO-RSG/PhytoFit/tree/master/verified_fits	27 Feb 2026
PhytoFit	https://cioosatlantic.ca/phytofit	27 Feb 2026

8 FIGURES

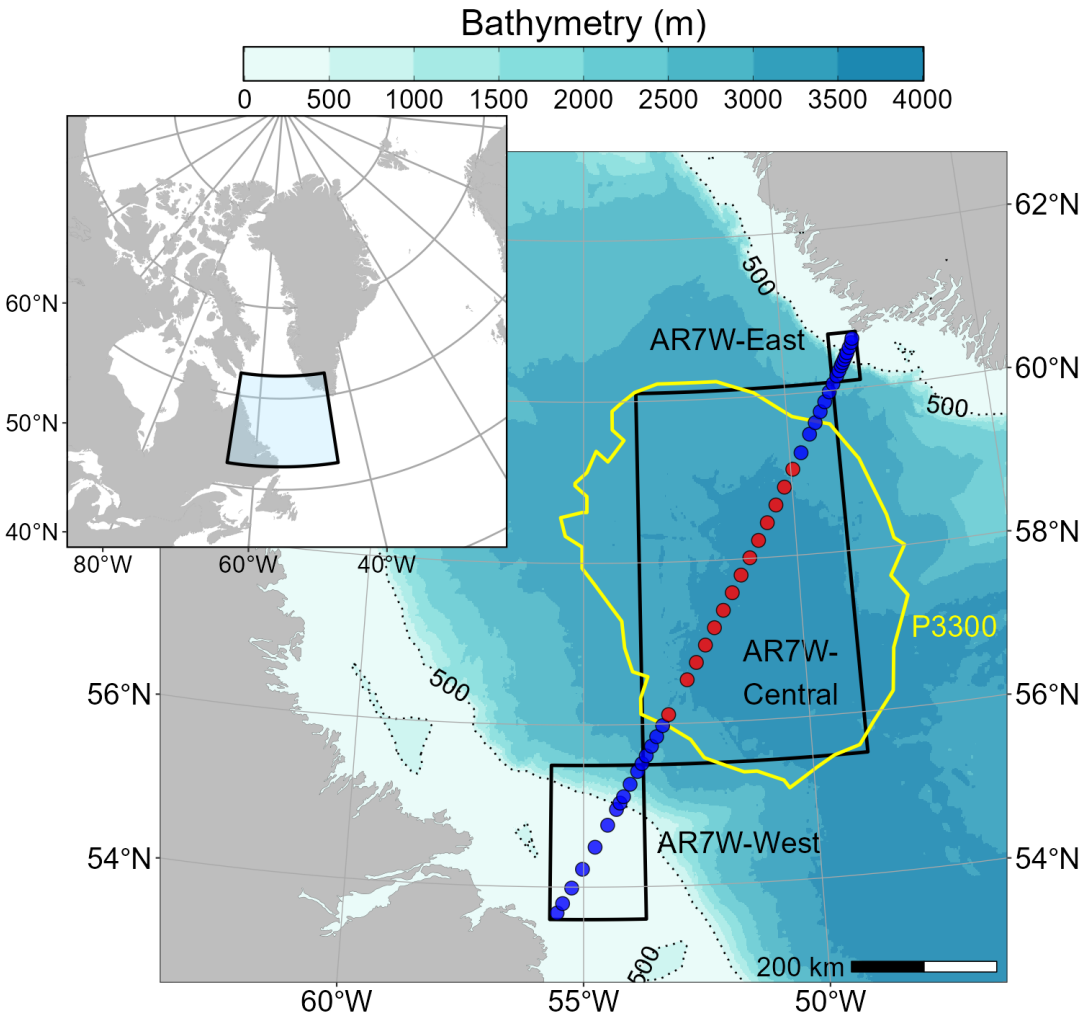


Figure 1. AR7W transect within the Labrador Sea. Blue and red dots represent the location of the core stations. Red stations are used in the calculation of annual averages for DIC, pH, and tracers for the NV-LSW from 150-500 m depth. Boxes correspond to the regions where satellite chl-a concentration is extracted (i.e., AR7W-West, AR7W-Central, and AR7W-East). Yellow polygon (P3300) indicates the area used in the physical data analysis (i.e. the area within 150 km of the AR7W line where bathymetry exceeds 3300 m). Dotted black lines correspond to the 500 m isobath.

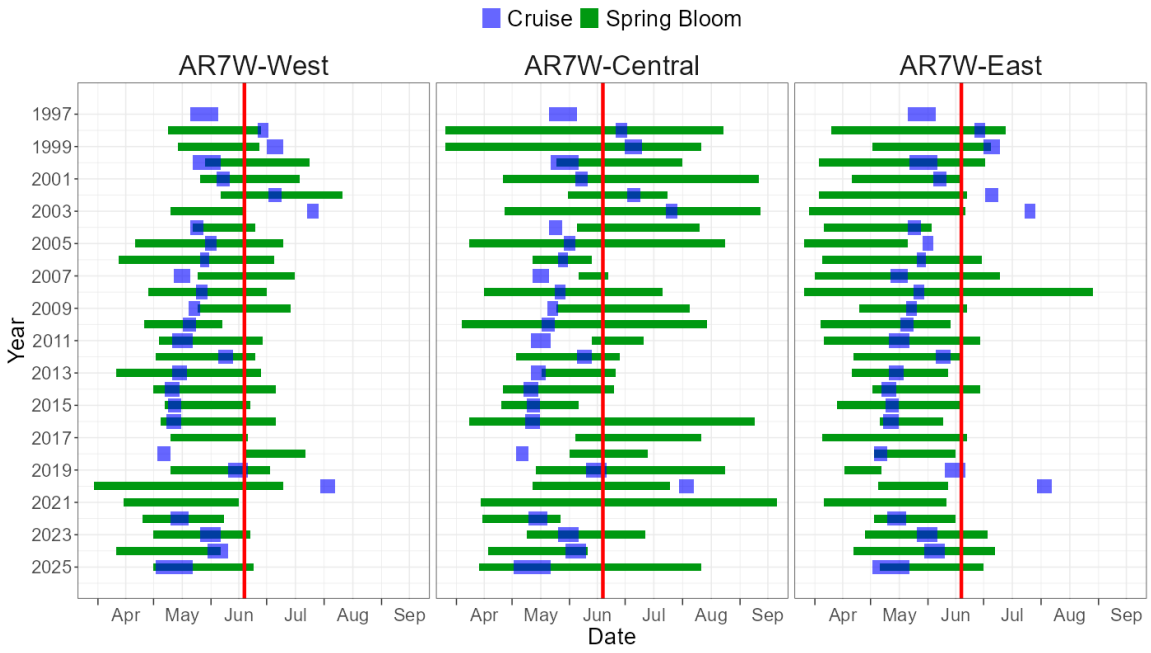


Figure 2. Blue rectangles represent the sampling period (actual occupation of AR7W line) and green rectangles correspond to the duration of the spring bloom within each region as derived from satellite ocean colour for AR7W-West (left), AR7W-Central (middle), and AR7W-East (right). Vertical red line (day of year 170) represents our cutoff date separating early and late missions.

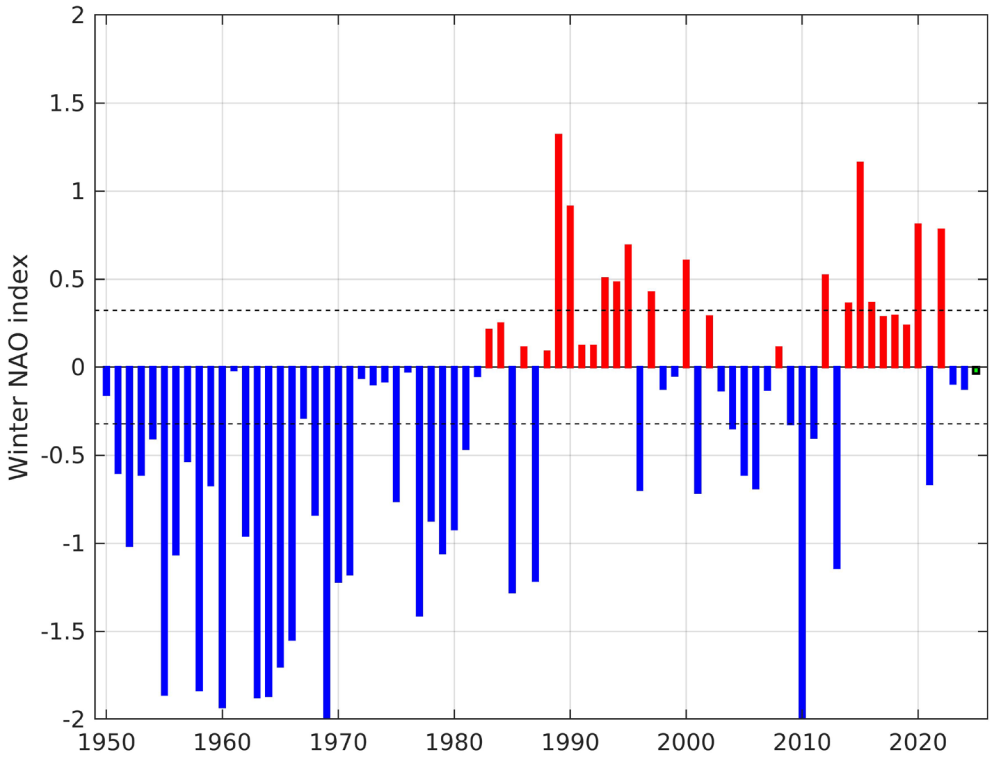


Figure 3. Anomalies of the winter (January to March) North Atlantic Oscillation (NAO) index, relative to the 1991-2020 mean. Horizontal dashed lines represent plus or minus 0.5 SD for the 1991–2020 period.

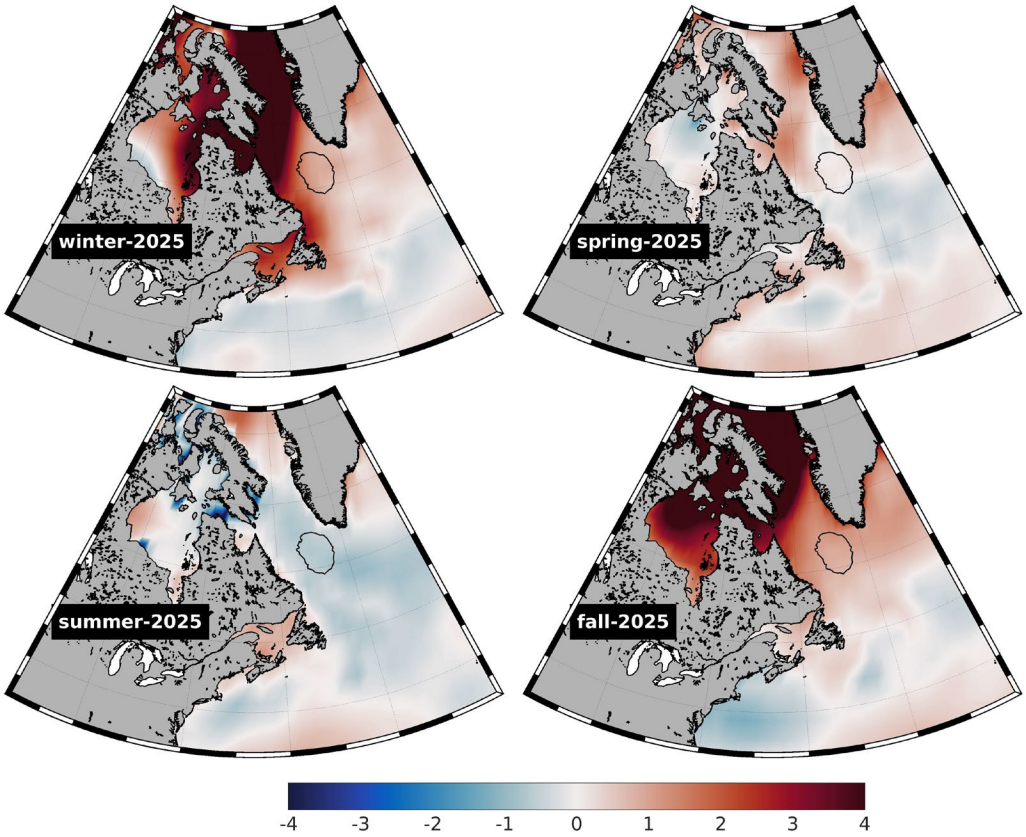


Figure 4. Surface air temperature anomaly (˚C) for winter (Jan-Mar), spring (Apr-Jun), summer (Jul-Sep), and fall (Oct-Dec) periods in 2025 as derived from NCEP/NCAR reanalysis. The black polygon represents the area defined as the central Labrador Sea for this report.

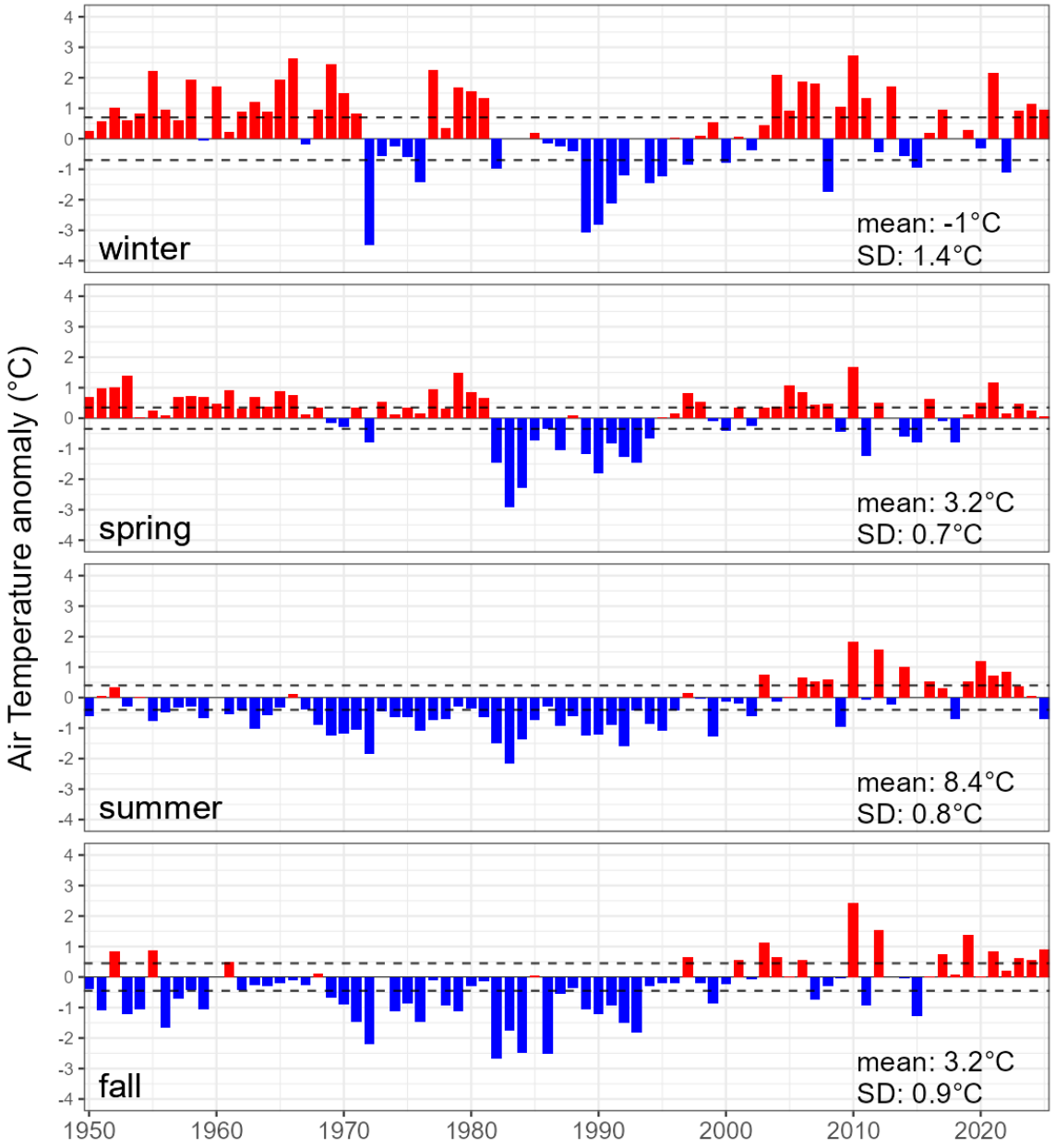


Figure 5. Anomalies of winter (Jan-Mar), spring (Apr-Jun), summer (Jul-Sep), and fall (Oct-Dec) air temperature in the central Labrador Sea, relative to the 1991-2020 mean. Derived from NCEP/NCAR Reanalysis dataset. Horizontal dashed lines represent plus or minus 0.5 SD for the 1991–2020 period. The numbers on the right are the means and standard deviations for the four seasons from the 1991-2020 period.

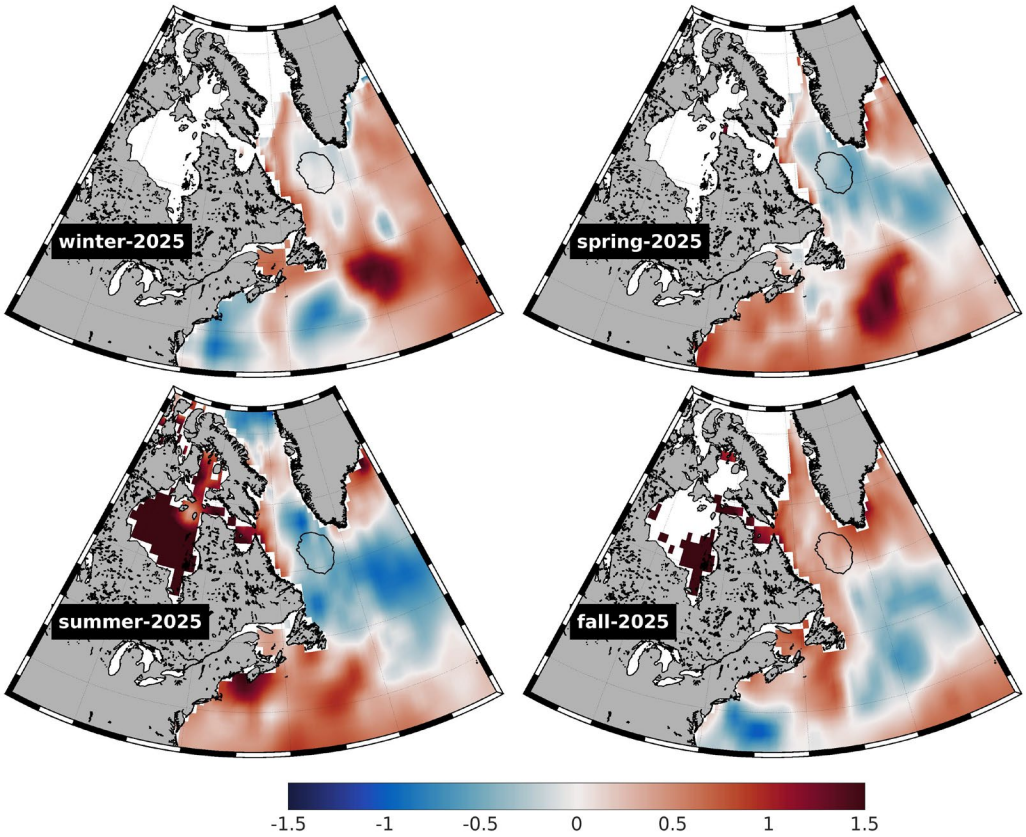


Figure 6. Sea surface temperature anomaly (˚C) for winter (Jan-Mar), spring (Apr-Jun), summer (Jul-Sep), and fall (Oct-Dec) periods in 2025 as derived from HadISST. The black polygon represents the area defined as the central Labrador Sea for this report.

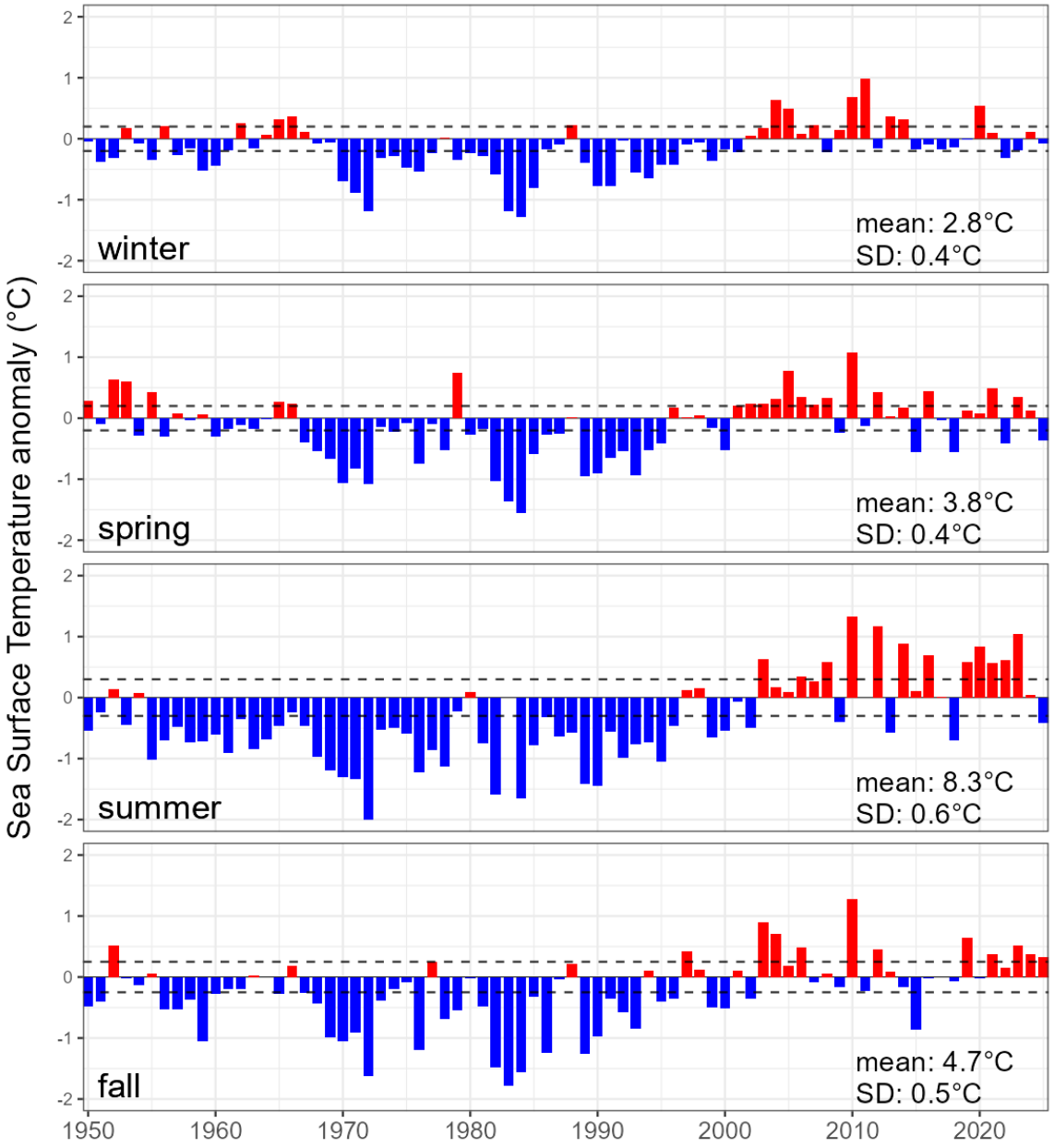


Figure 7. Anomalies of winter (Jan-Mar), spring (Apr-Jun), summer (Jul-Sep), and fall (Oct-Dec) sea surface temperature in the central Labrador Sea, relative to the 1991-2020 mean. Derived from HadISST dataset. Horizontal dashed lines represent plus or minus 0.5 SD for the 1991–2020 period. The numbers on the right are the means and standard deviations for the four seasons from the 1991-2020 period.

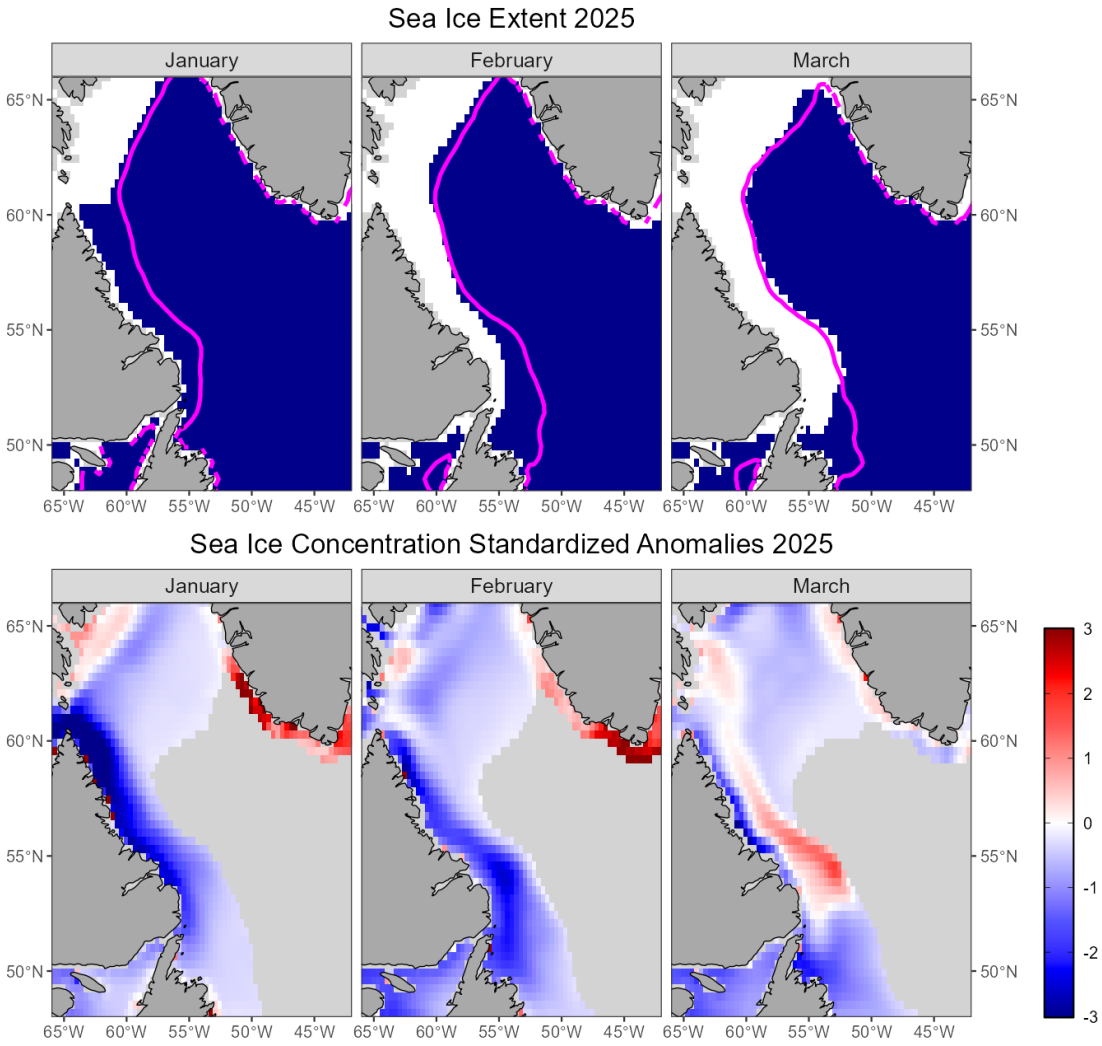


Figure 8. Top row: Sea ice extent for January to March 2025 (white pixels indicate sea ice concentration larger than 15%, blue pixels have low ice concentration or no ice, and light grey pixels have no data). The magenta line indicates the climatological median sea ice extent. Bottom row: Standardized anomalies of monthly sea ice concentration from January to March 2025, relative to the 1991-2020 climatological period. Pixels are greyed out where the climatological mean sea ice concentration was less than 1%.

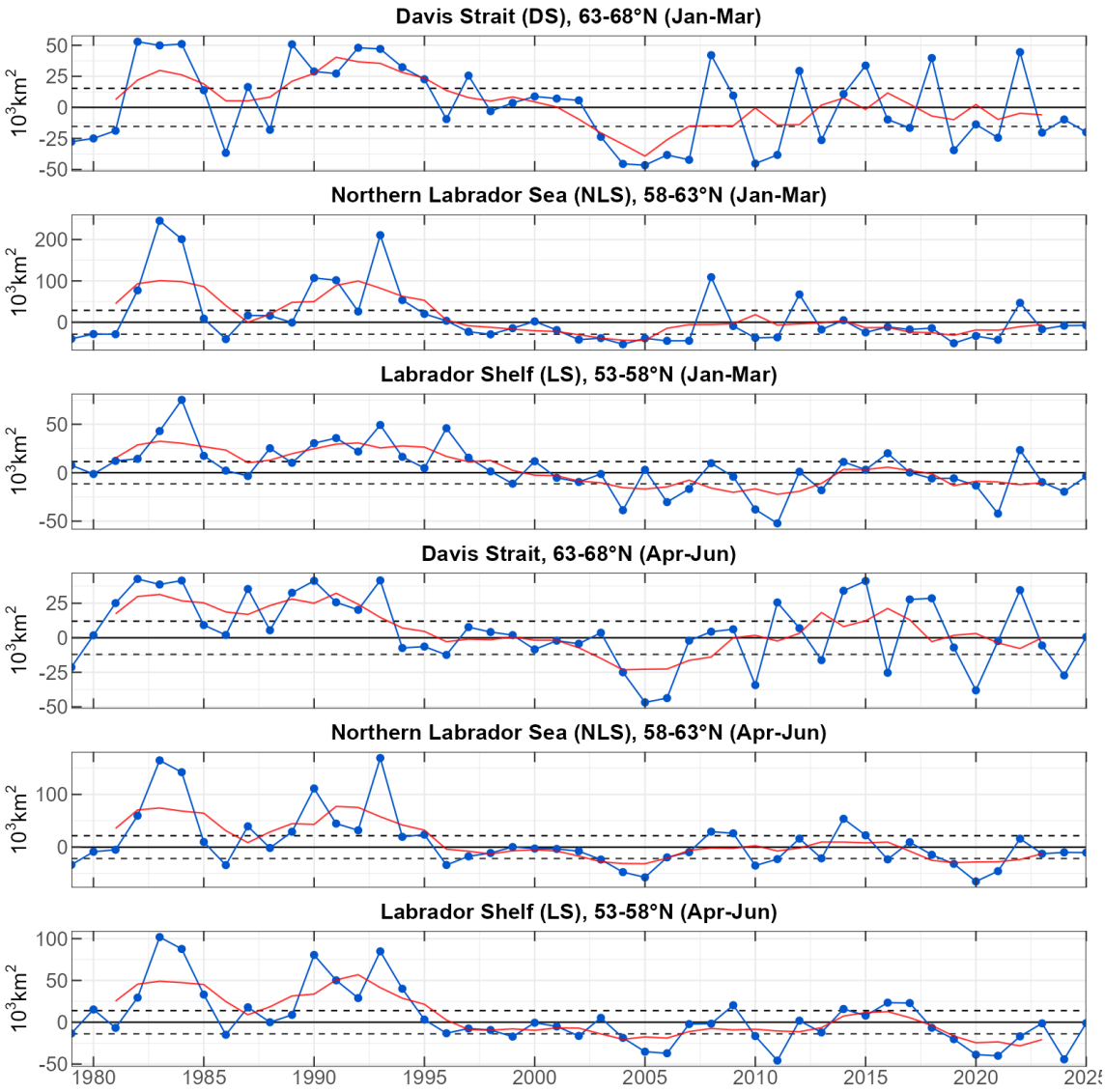


Figure 9. Winter and spring sea ice extent anomalies (blue) and their five-year running means (red) for: (1) Davis Strait (63-68°N), (2) the Northern Labrador Sea (58-63°N), and (3) Labrador Shelf (53-58°N). Horizontal dashed lines represent plus or minus 0.5 SD for the 1991-2020 period.

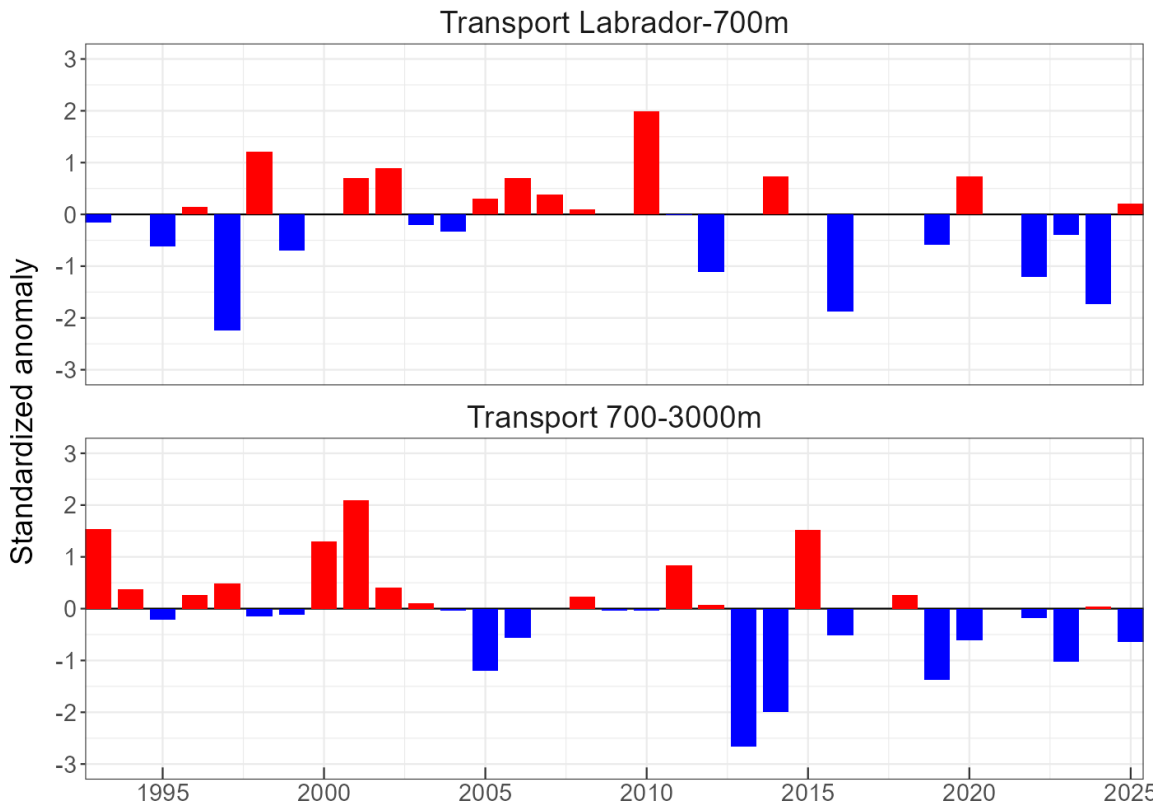


Figure 10. Standardized anomalies of the spring-summer Labrador Current transport over 1993-2025 for (a) the Labrador Slope (between 700- and 3000-m isobaths) and (b) the Labrador Shelf (inshore of the 700-m isobath).

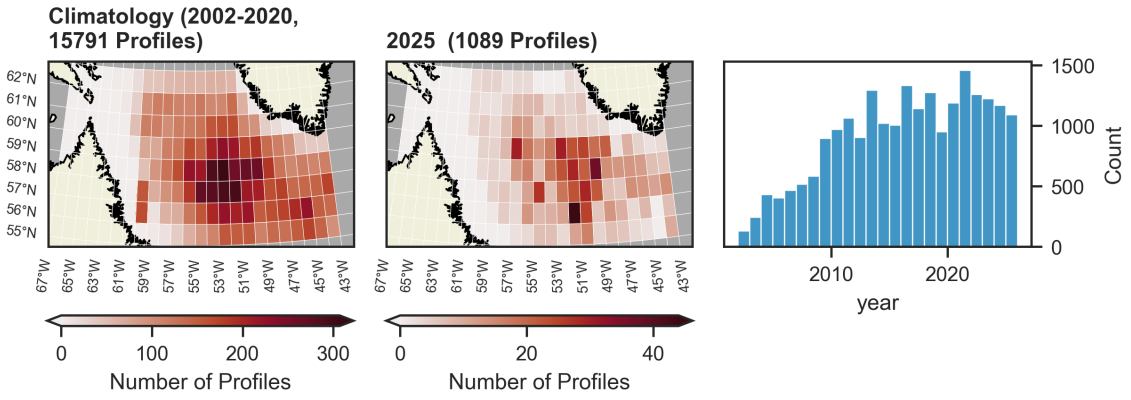


Figure 11. The number of Argo profiles in the Labrador Sea region, as defined by the grid cells that are not colored grey (left: climatology; middle: 2025; right: evolution of the number of profiles).

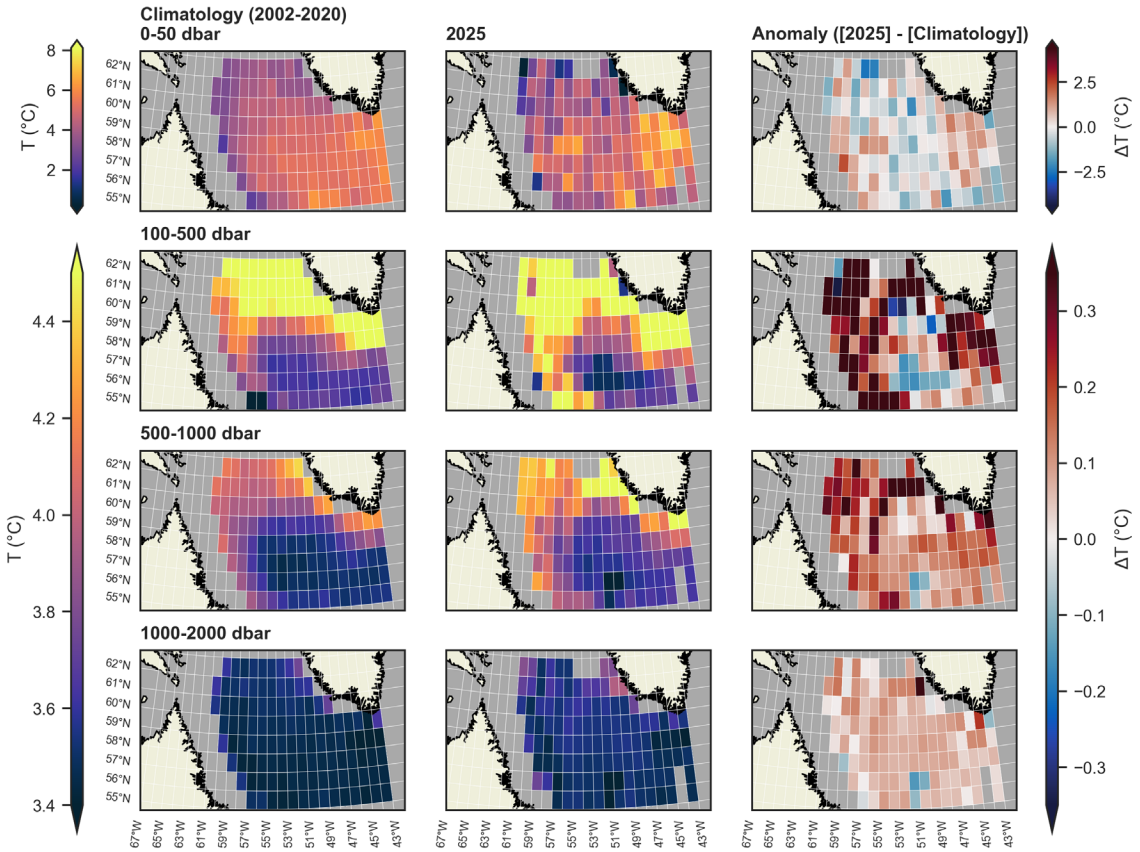


Figure 12. The averaged temperature in the water column in each depth layer (0-50 dbar, 100-500 dbar, 500-1000 dbar, and 1000-2000 dbar), measured by Argo profiles (left column: climatology; middle: 2025; right: 2025 anomalies relative to the climatology). Note the different colour scale used for surface (0-50 dbar) vs other layers.

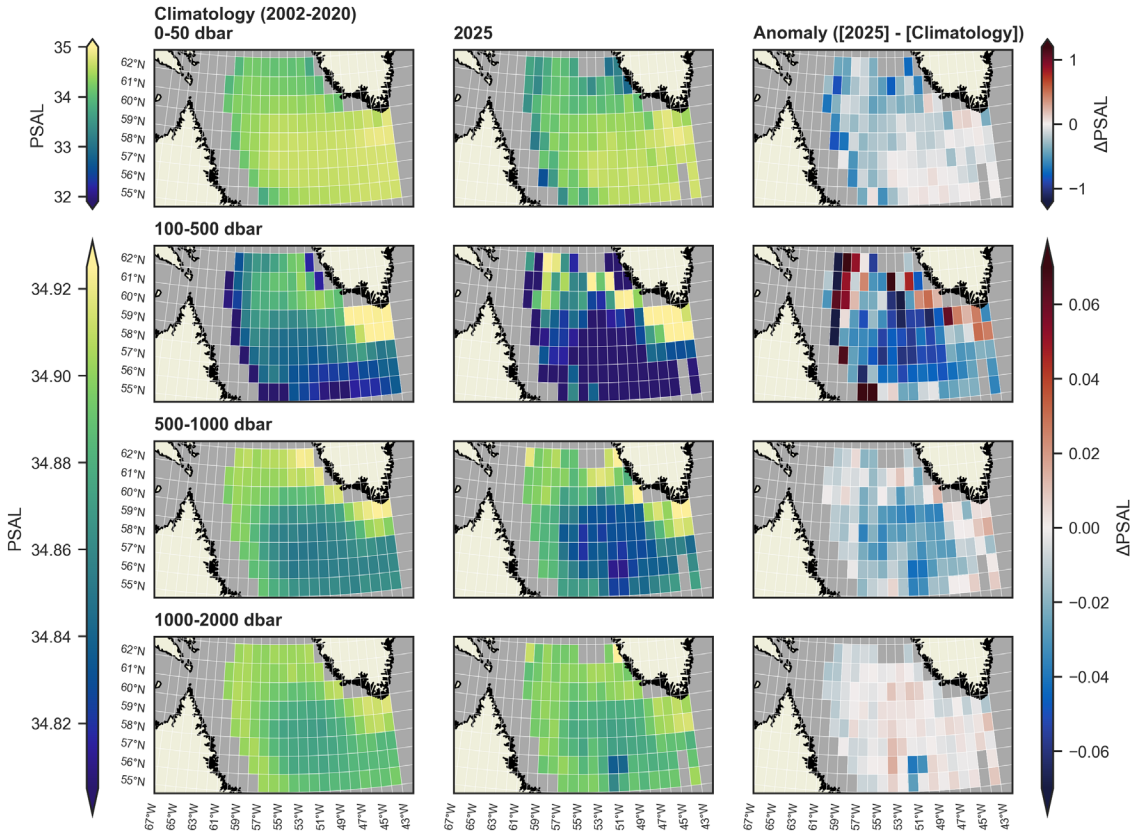


Figure 13. The averaged practical salinity in the water column in each depth layer (0-50 dbar, 100-500 dbar, 500-1000 dbar, and 1000-2000 dbar), measured by Argo profiles (left column: climatology; middle: 2025; right: 2025 anomalies relative to the climatology). Note the different colour scale used for surface (0-50 dbar) vs other layers.

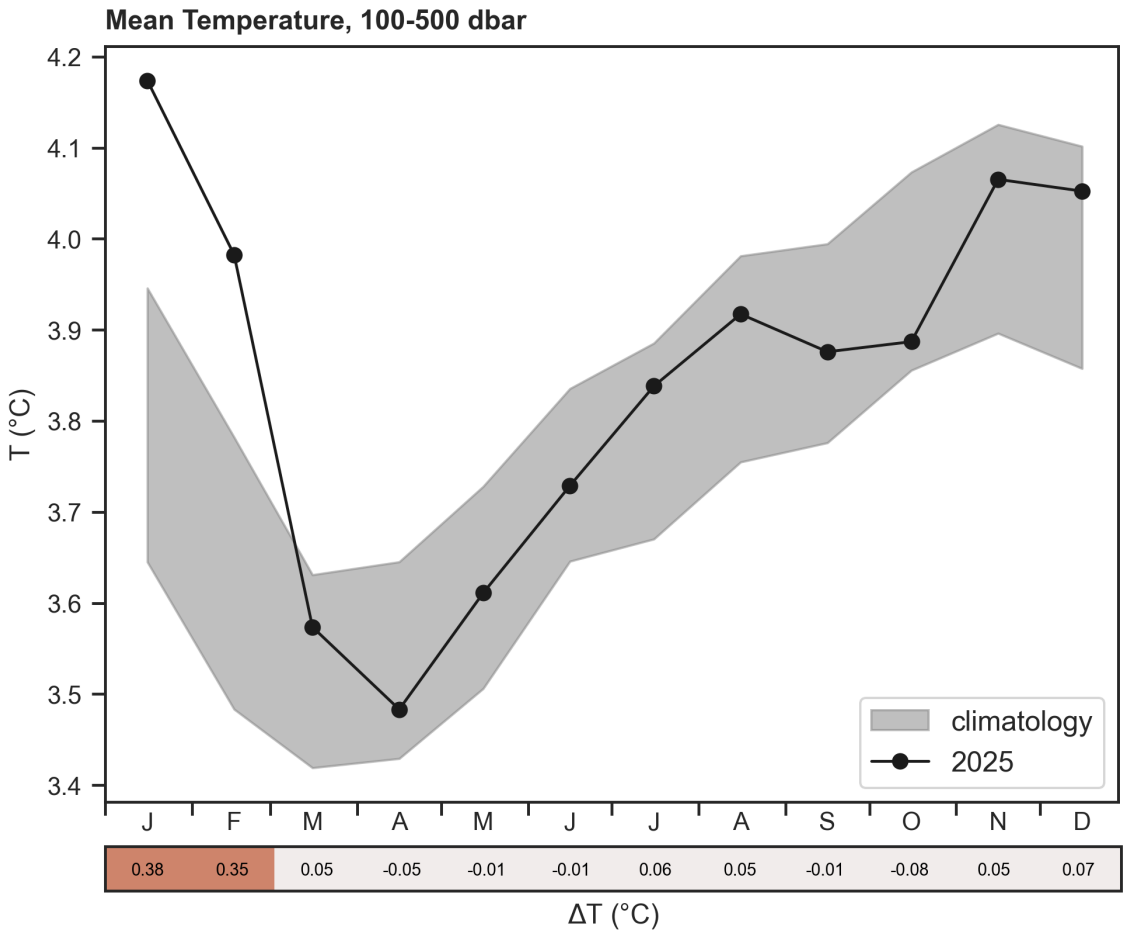


Figure 14. Time series of monthly temperature in 2025 (black) and the climatology of the 2002-2020 period (shaded area), as determined from Argo data for the P3300 polygon. The shaded area is plus/minus 0.5 SD from the climatological mean. The colours/numbers along the bottom show the difference between 2025 (black) and climatology (grey) for each month.

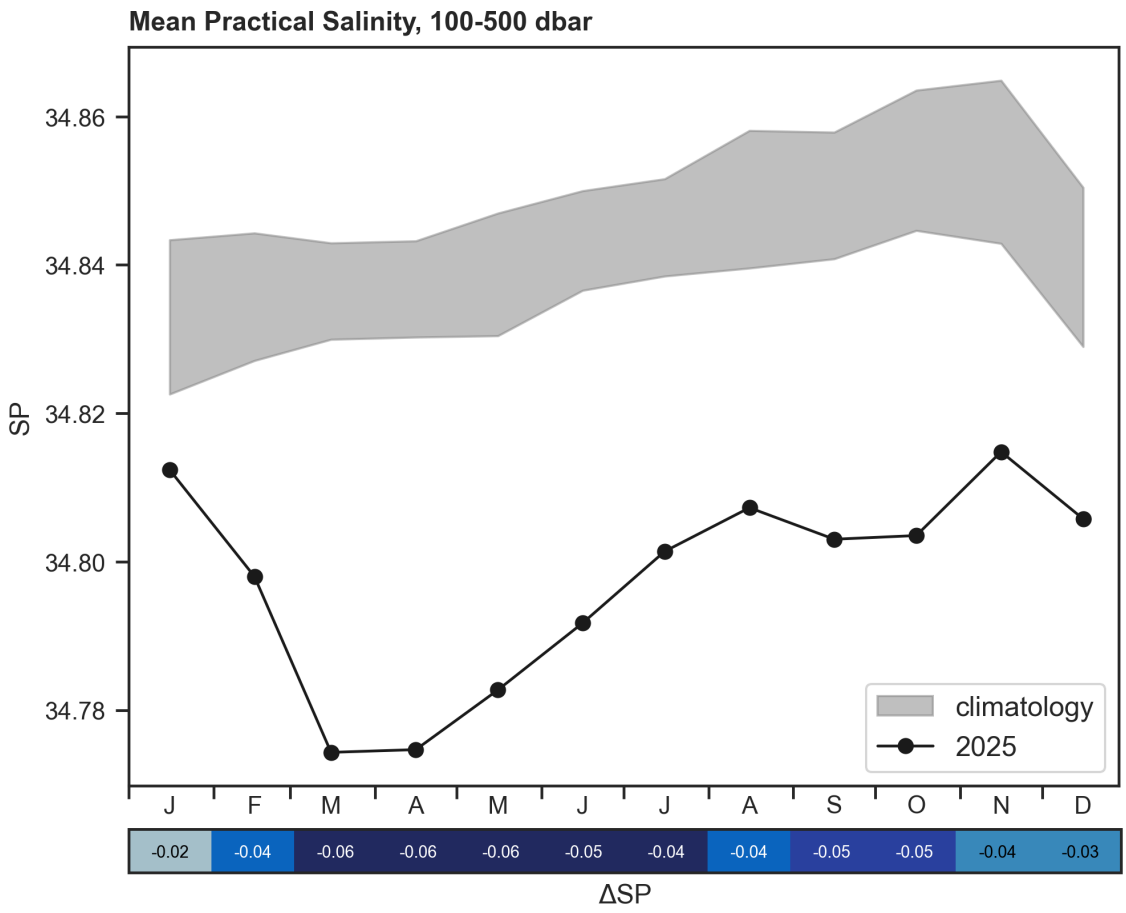


Figure 15. Time series of monthly practical salinity in 2025 (black) and the climatology of the 2002-2020 period (shaded area), as determined from Argo data for the P3300 polygon. The shaded area is plus/minus 0.5 SD from the climatological mean. The colours/numbers along the bottom show the difference between 2025 (black) and climatology (grey) for each month.

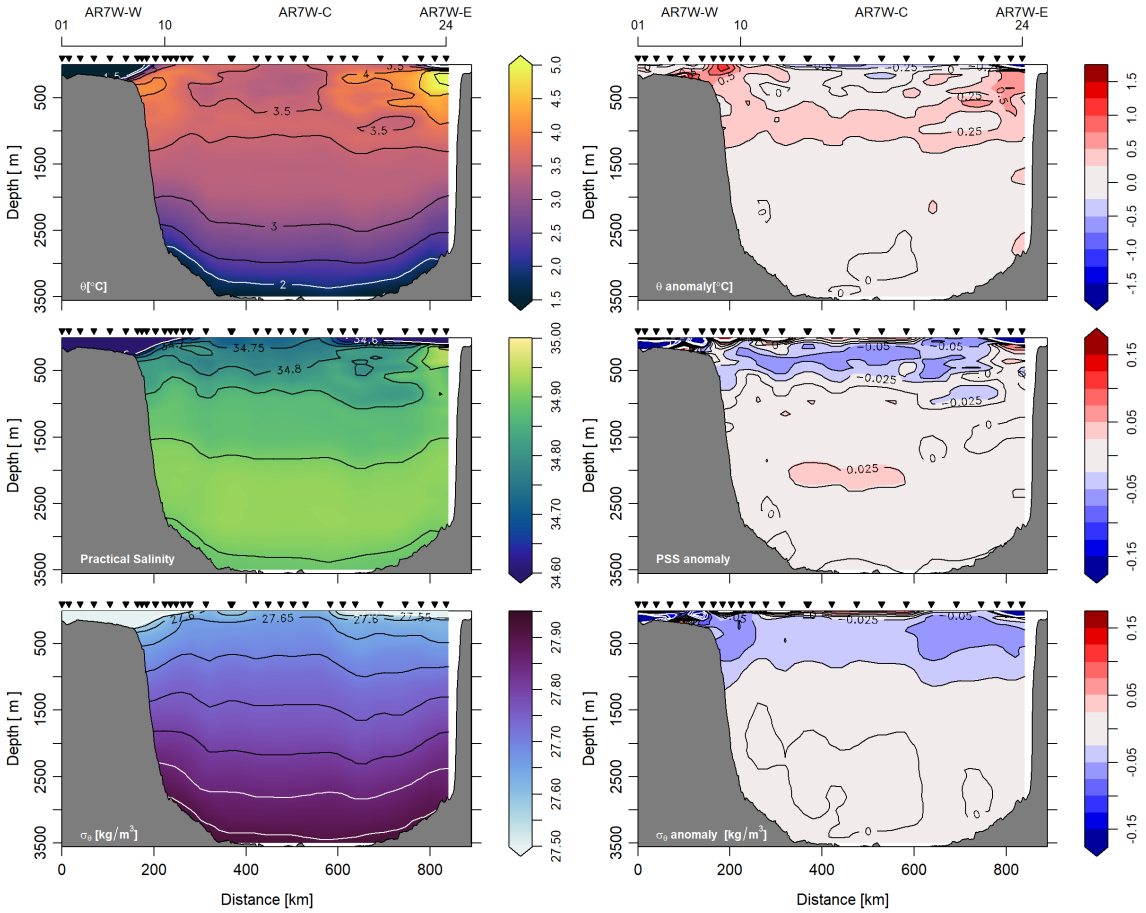


Figure 16. Left panels: Temperature (top), salinity (middle), and density(bottom) distribution along the AR7W line from the 2025 cruise CTD data. Right panels: Temperature (top), salinity (middle), and density (bottom) anomalies relative to the 1991-2020 climatology. Station locations are indicated by triangles along the top axis.

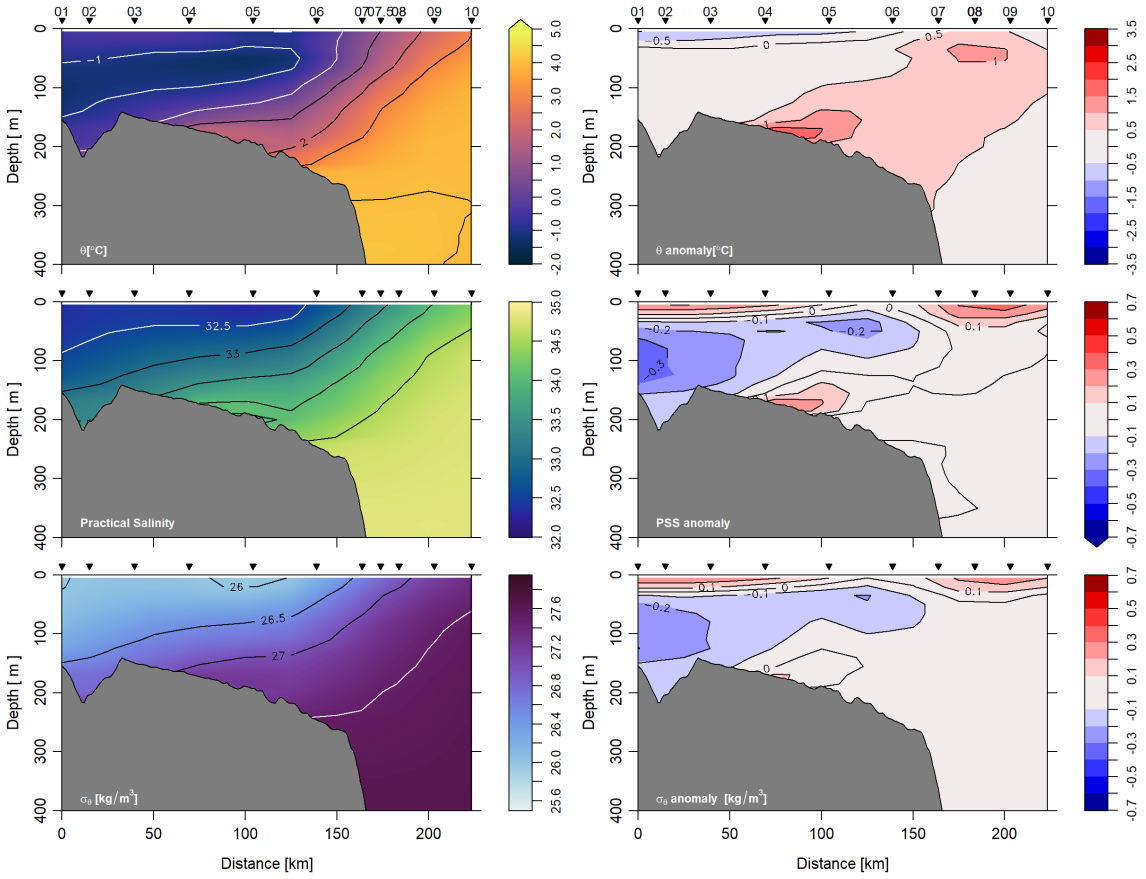


Figure 17. Left panels: Temperature (top), salinity (middle), and density (bottom) distribution on the Labrador Shelf from the 2025 cruise CTD data. Right panels: Temperature (top), salinity (middle), and density (bottom) anomalies relative to the 1991-2020 climatology. Station locations are indicated by triangles along the top axis.

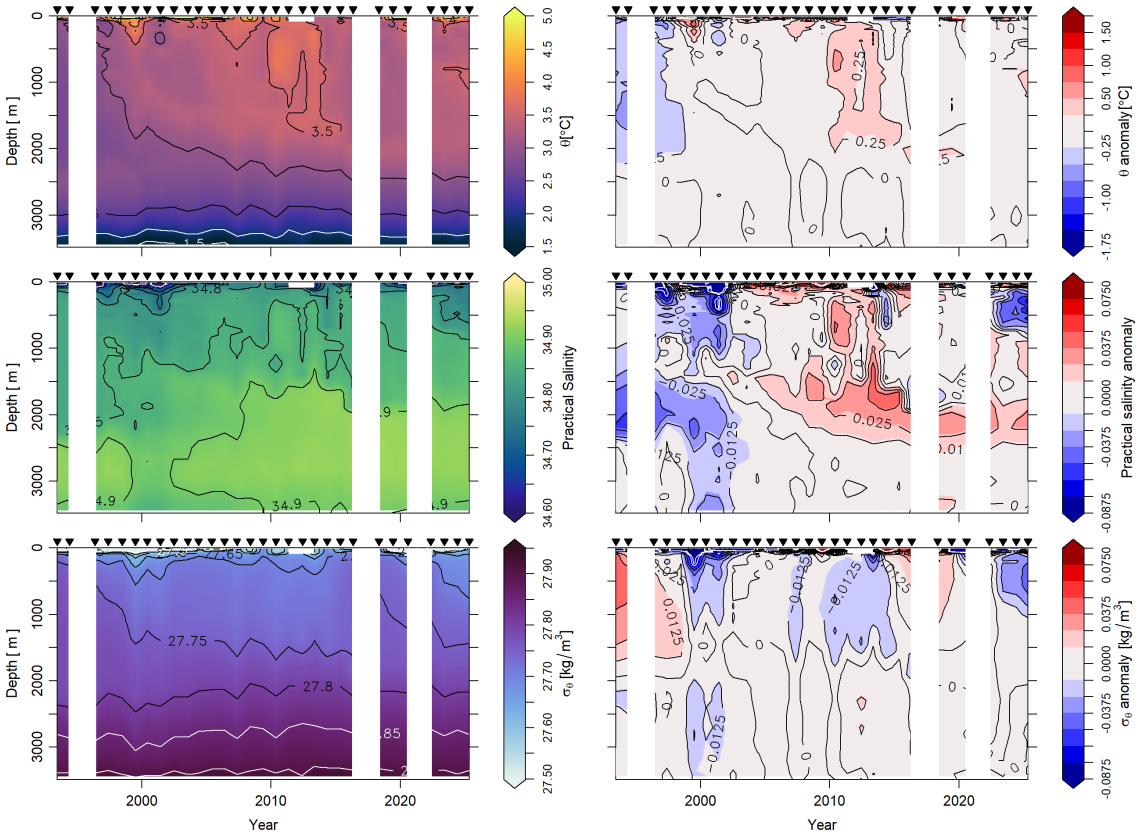


Figure 18. Left panels: Evolution of the temperature (top), salinity (middle), and density (bottom) from AR7W Station 15.5 in the center of the Labrador Sea from ship CTD data. Right panels: Evolution of temperature (top), salinity (middle), and density (bottom) anomalies relative to the 1991-2020 climatology. Triangles at the top of each panel indicate the time of sampling.

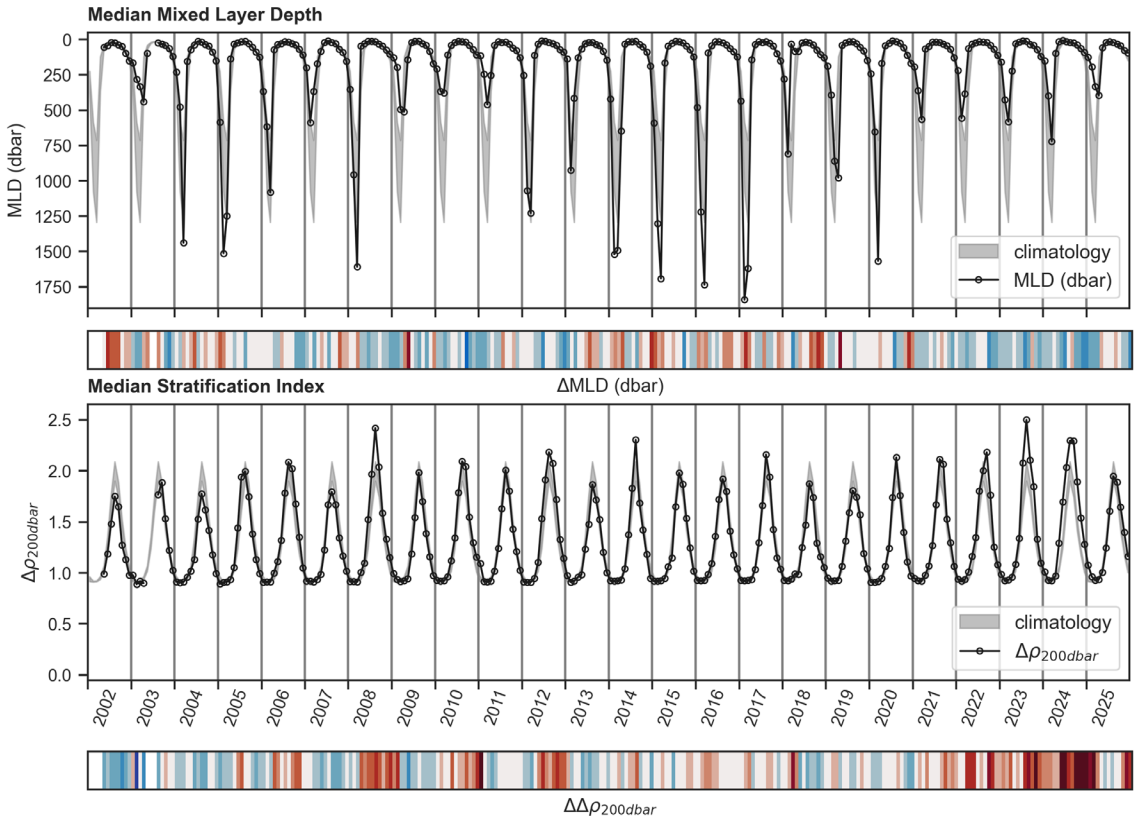


Figure 19. Median mixed layer depth (top panel) and stratification index (lower panel) calculated using Argo profiles inside the P3300 polygon. The shaded area shows a repeated monthly climatology (+/- 0.5 SD) and colours below indicate the magnitude of the difference between the timeseries and climatology in each month (red indicating deeper MLD or higher stratification, blue indicating shallower MLD or weaker stratification).

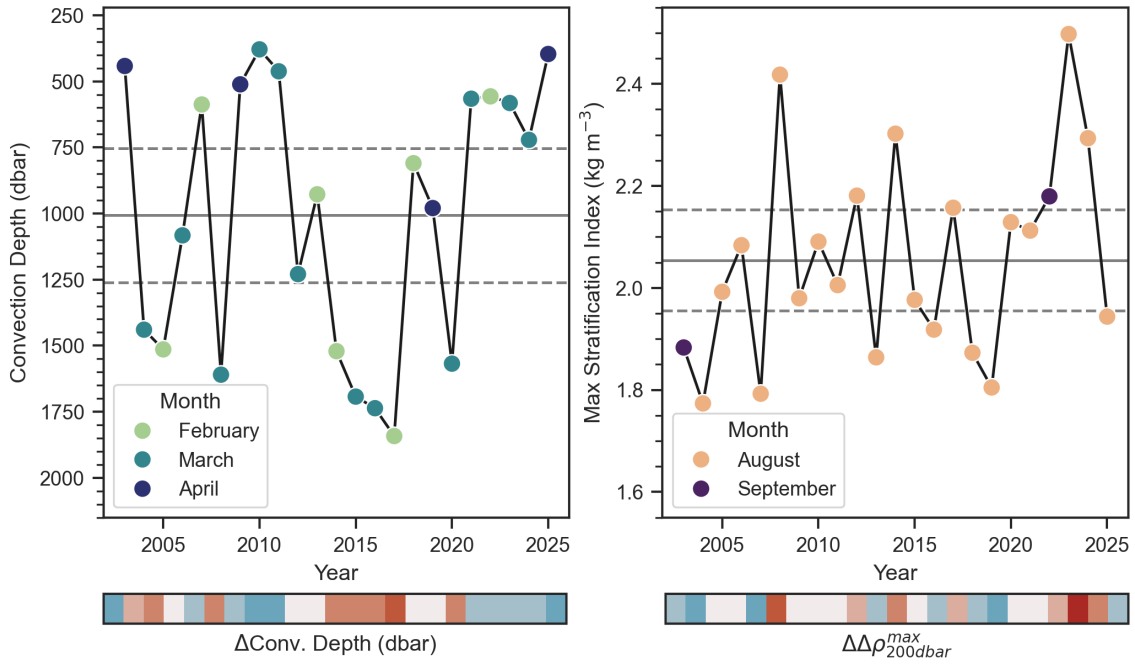


Figure 20. Convection depth (left panel) and stratification index (right panel) computed from the maximum yearly values of mixed layer depth and stratification index derived from Argo data in the P3300 polygon. The solid horizontal line shows the mean value across the timeseries and the dashed lines show +/- 0.5 SD. Colour of the points indicate in which month of the year the maximum depth or stratification occurred.

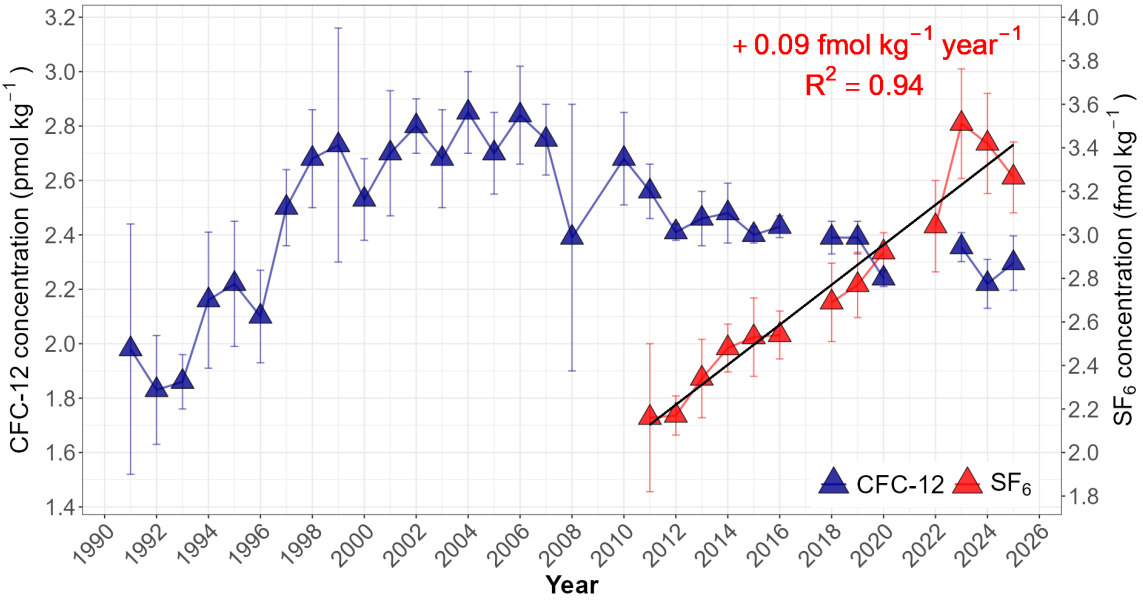


Figure 21. Time series of CFC-12 (blue solid triangles) and SF_6 (red solid triangles) in the Newly Ventilated Labrador Sea Water (150–500 m depth within 56°N to 59.1°N) from 1991 to 2025. Vertical bars indicate one standard deviation and black solid line corresponds to the linear regression of SF_6 against time for the period 2011-2025.

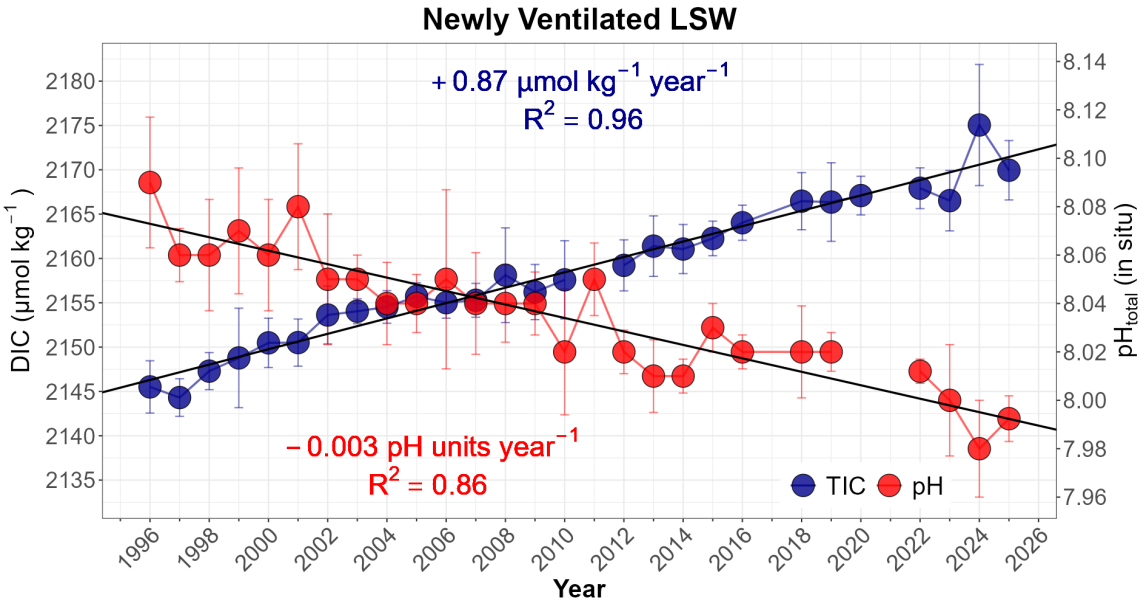


Figure 22. Time series of Dissolved Inorganic Carbon (DIC; blue solid circles) and pH (red solid circles) within the Newly Ventilated Labrador Sea Water (150–500 m depth within 56°N to 59.1°N). Vertical bars indicate one standard deviation and black solid lines correspond to the linear regression of DIC and pH against time for the period 1996-2025.

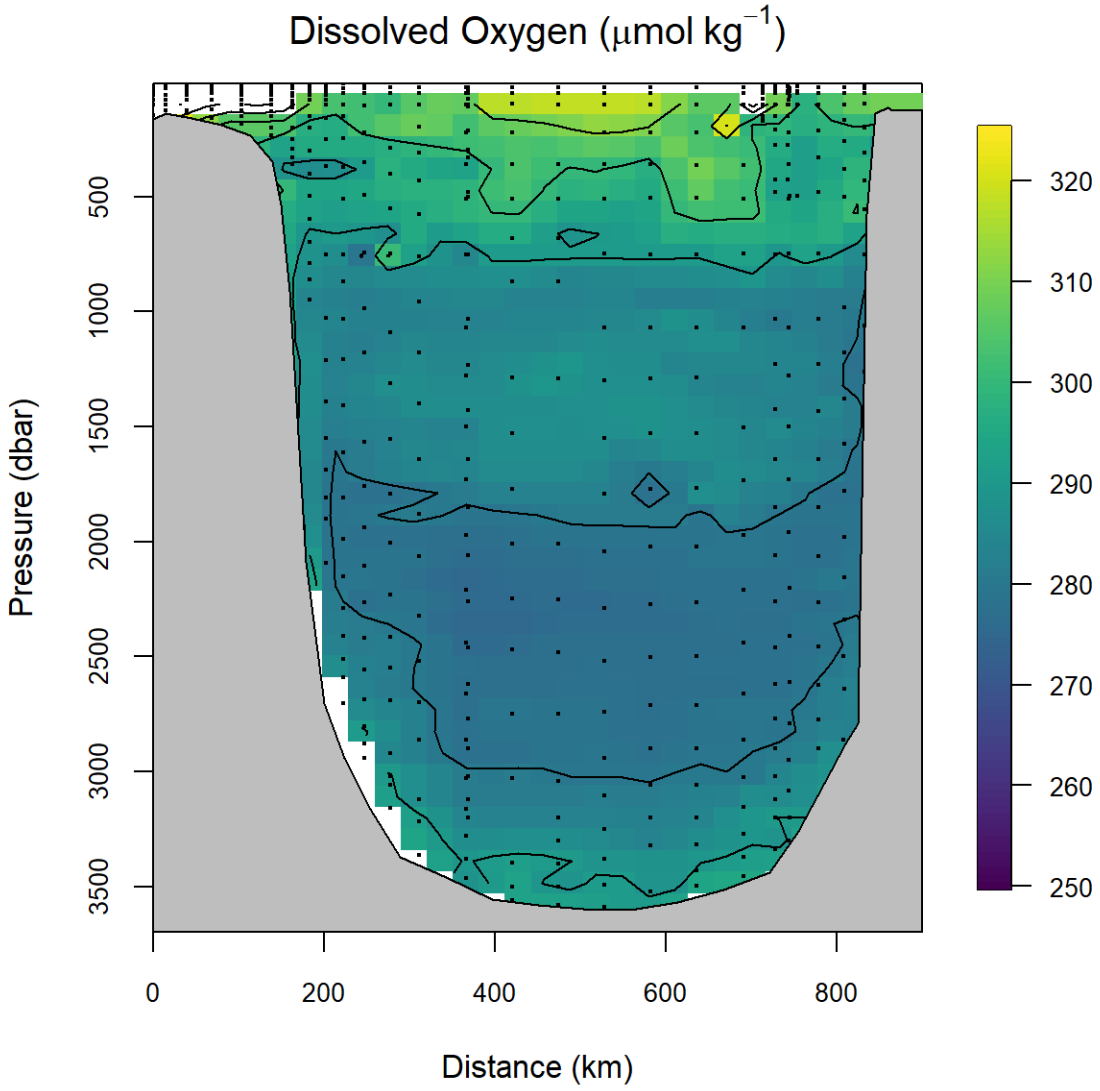


Figure 23. Measurements of dissolved oxygen along the AR7W line in 2025 using the Winkler titration method. Dots indicate sampling locations.

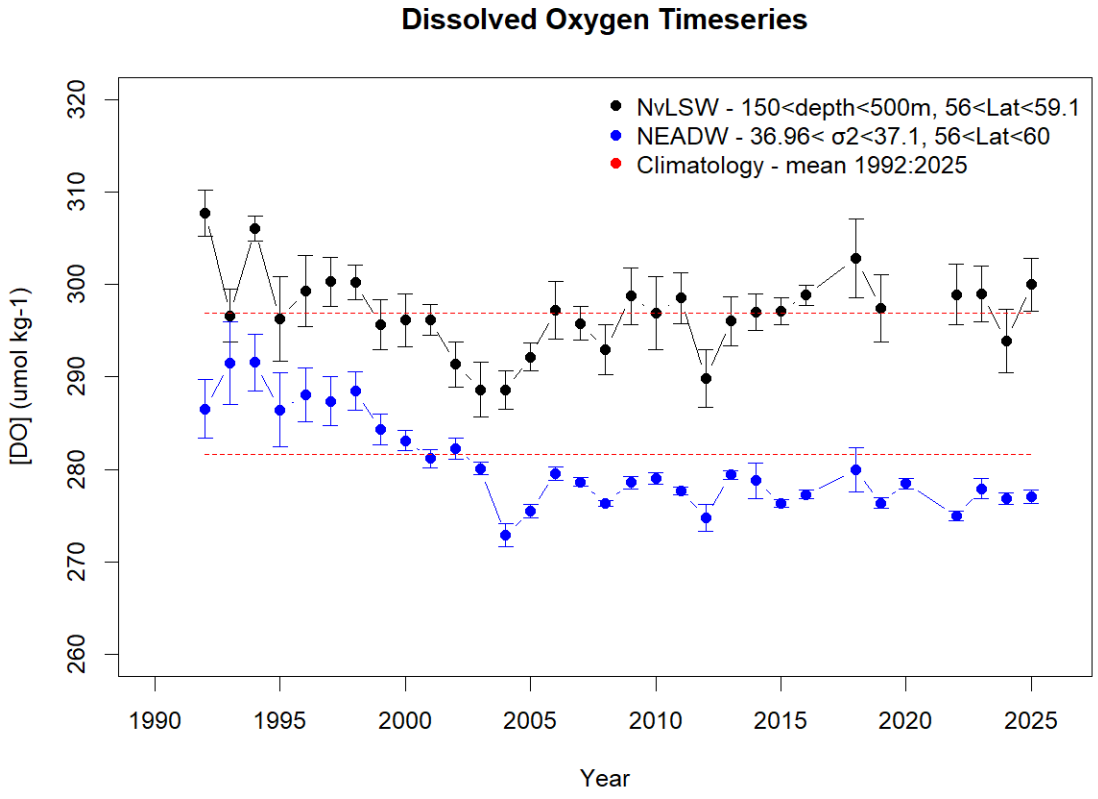


Figure 24. Timeseries of Winkler dissolved oxygen measurements in the Newly Ventilated Labrador Sea Water (NV-LSW) and the Northeast Atlantic Deep Water (NEADW) masses.

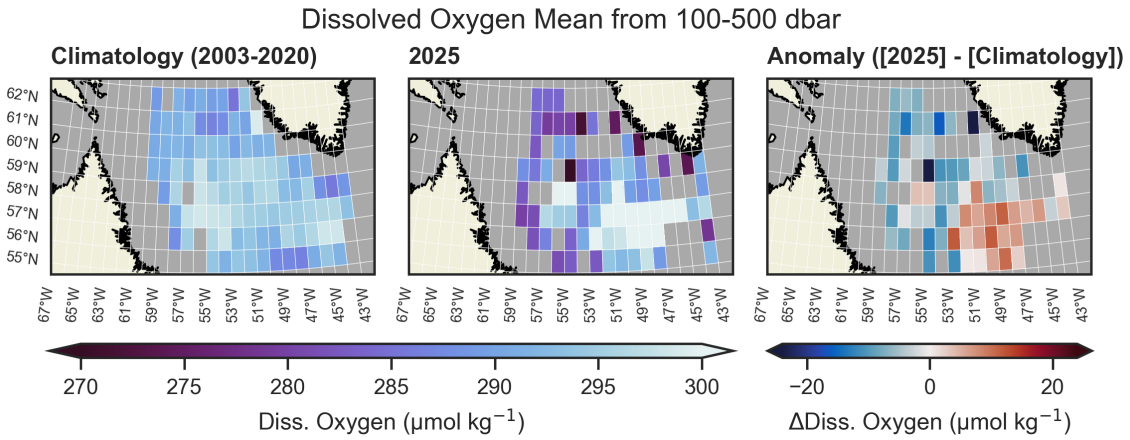


Figure 25. Mean adjusted dissolved oxygen from 100-500 dbar measured by biogeochemical Argo floats in each grid cell for the climatology period (left), 2025 (middle), and the anomalies (right).

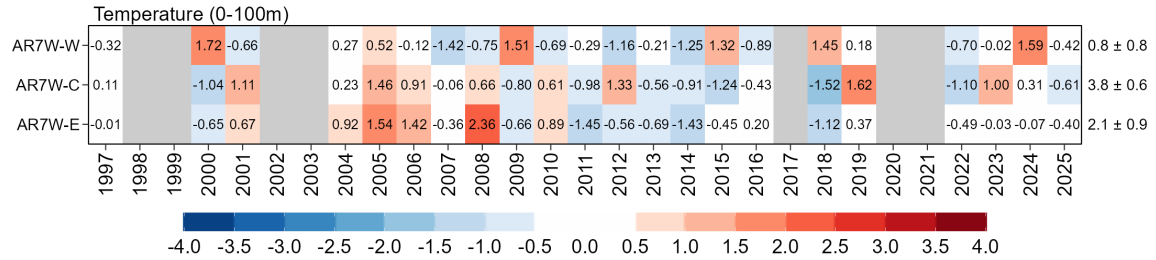


Figure 26. Scorecard for average temperature in the water column (surface to 100 m) measured from the CTD during each bottle firing, from 1997 to 2025 for the AR7W-West (AR7W-W), AR7W-Central (AR7W-C), and AR7W-East (AR7W-E) polygons. Grey boxes indicate no data or late sampling years (not included in the reference period average). Numbers in the scorecard cells represent the annual standardized anomalies. Numbers on the right side indicate the mean values 1999–2025 (i.e., reference, °C) for a given region as well as the standard deviation (i.e., mean ± standard deviation).

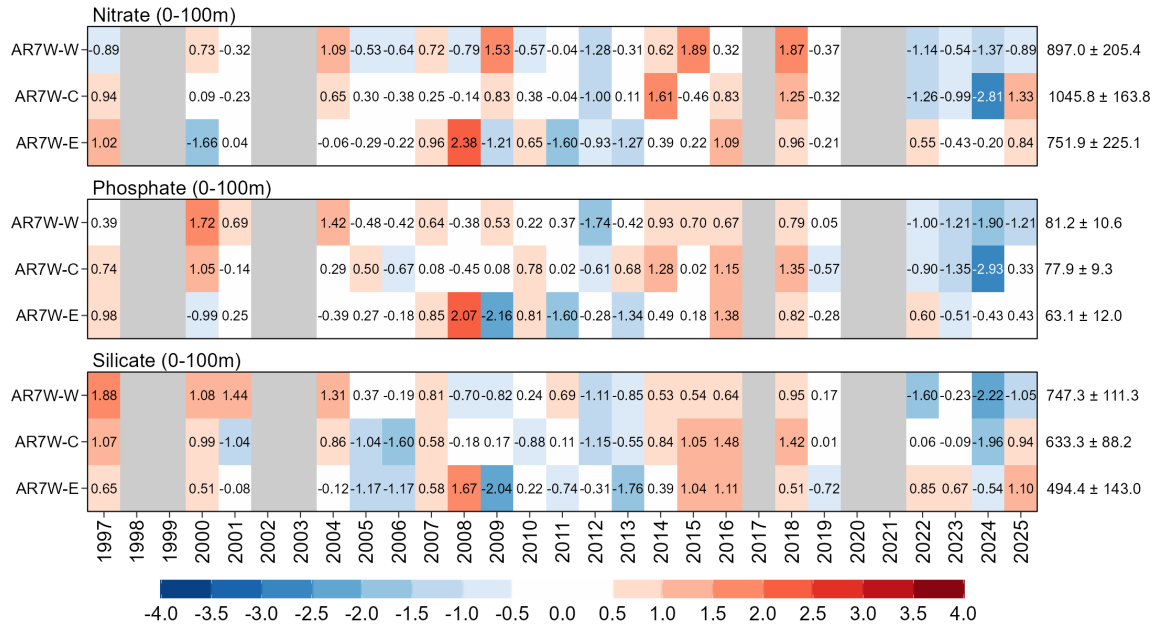


Figure 27. Scorecards for surface nutrients from 1997 to 2025 for the AR7W-West (AR7W-W), AR7W-Central (AR7W-C), and AR7W-East (AR7W-E) polygons. Grey boxes indicate no data or late sampling years (not included in the reference period average). Numbers in the scorecard cells represent the annual standardized anomalies. Numbers on the right side indicate the mean values 1999–2025 (i.e., reference, $mmol\ m^{-2}$) for a given region as well as the standard deviation (i.e., mean ± standard deviation).

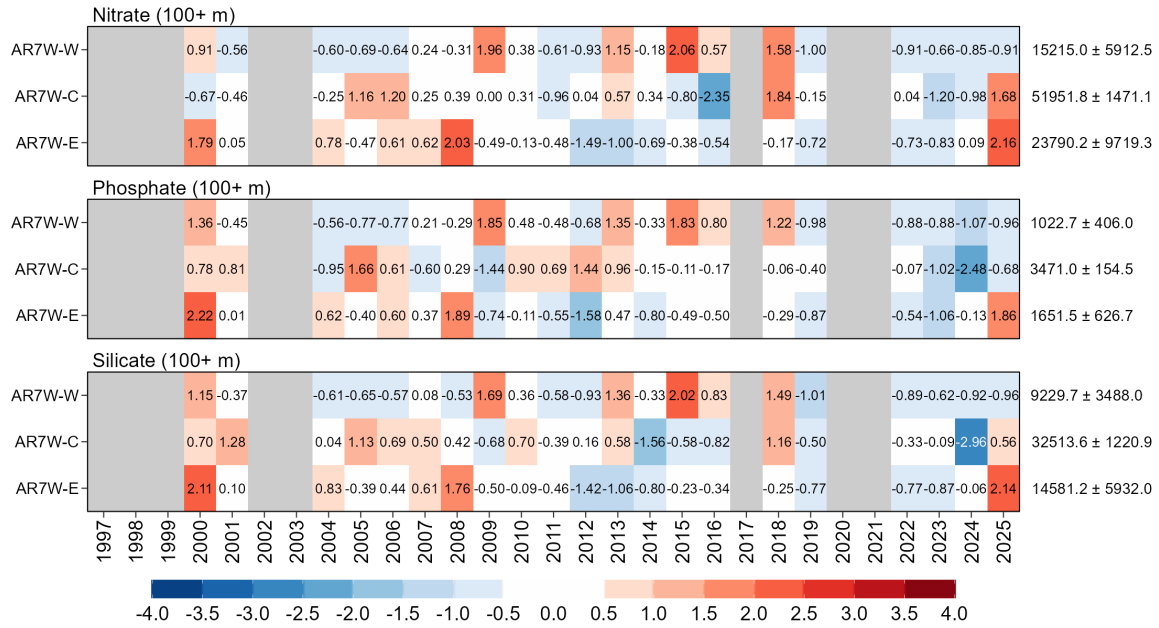


Figure 28. Scorecards for deep nutrients from 1997 to 2025 for the AR7W-West (AR7W-W), AR7W-Central (AR7W-C), and AR7W-East (AR7W-E) polygons. Grey boxes indicate no data or late sampling years (not included in the reference period average). Numbers in the scorecard cells represent the annual standardized anomalies. Numbers on the right side indicate the mean values 1999–2025 (i.e., reference, $mmol\ m^{-2}$) for a given region as well as the standard deviation (i.e., mean ± standard deviation).

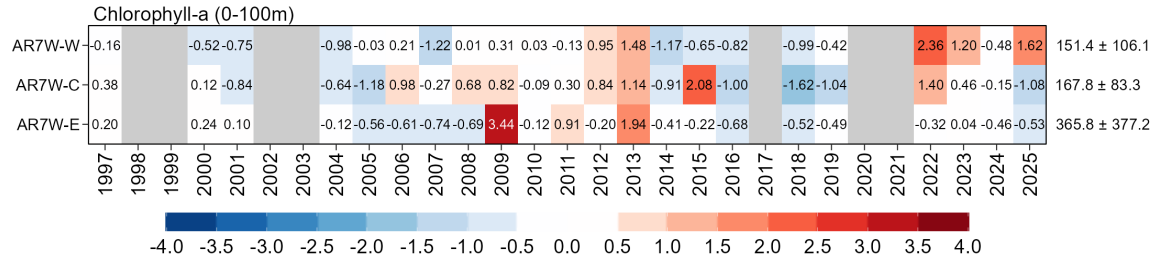


Figure 29. Scorecard for in situ chl-a from 1997 to 2025 for the AR7W-West (AR7W-W), AR7W-Central (AR7W-C), and AR7W-East (AR7W-E) polygons. Grey boxes indicate no data or late sampling years (not included in the reference period average). Numbers within cells represent the annual standardized anomalies. Numbers on the right side indicate the mean values 1999–2025 (i.e., reference, $mg\ m^{-2}$) for a given region as well as the standard deviation (i.e., mean ± standard deviation).

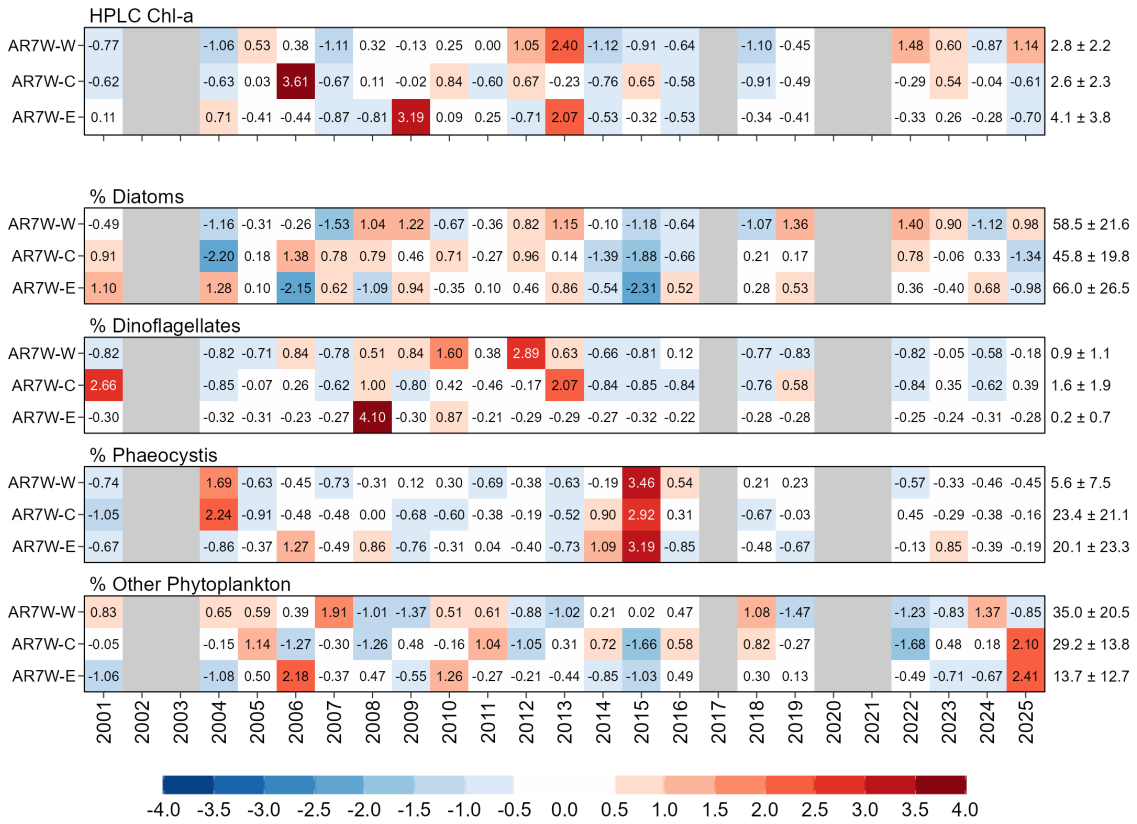


Figure 30. Scorecards for total biomass (chl-a, units of $mg\ m^{-3}$) and the percentage contribution of taxonomic groups to total biomass in the surface layer (i.e. <20 m), derived from HPLC measurements from 2001 to 2025 for the AR7W-West (AR7W-W), AR7W-Central (AR7W-C), and AR7W-East (AR7W-E) polygons. Grey boxes indicate no data. Numbers within cells represent the annual standardized anomalies. Numbers on the right side indicate the mean values 2001–2025 (i.e., reference) for a given region as well as the standard deviation (i.e., mean ± standard deviation).

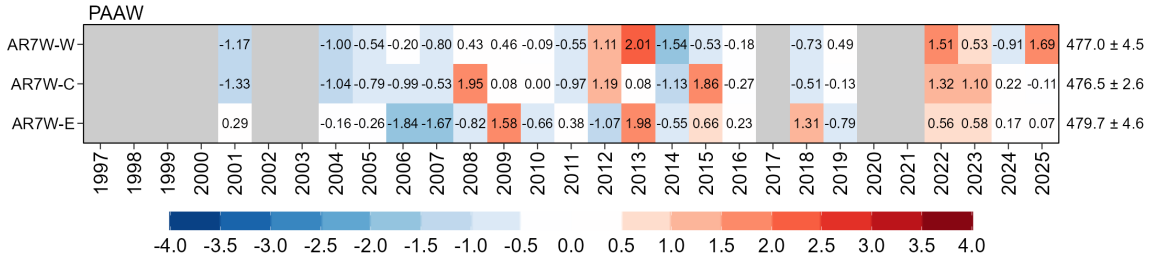


Figure 31. Scorecard for PAAW metric derived from surface phytoplankton absorption measurements from 1997 to 2025 for the AR7W-West (AR7W-W), AR7W-Central (AR7W-C), and AR7W-East (AR7W-E) polygons. Grey boxes indicate no data. Numbers within cells represent the annual standardized anomalies. Numbers on the right side indicate the mean values 1999–2025 (i.e., reference) for a given region as well as the standard deviation (i.e., mean ± standard deviation).

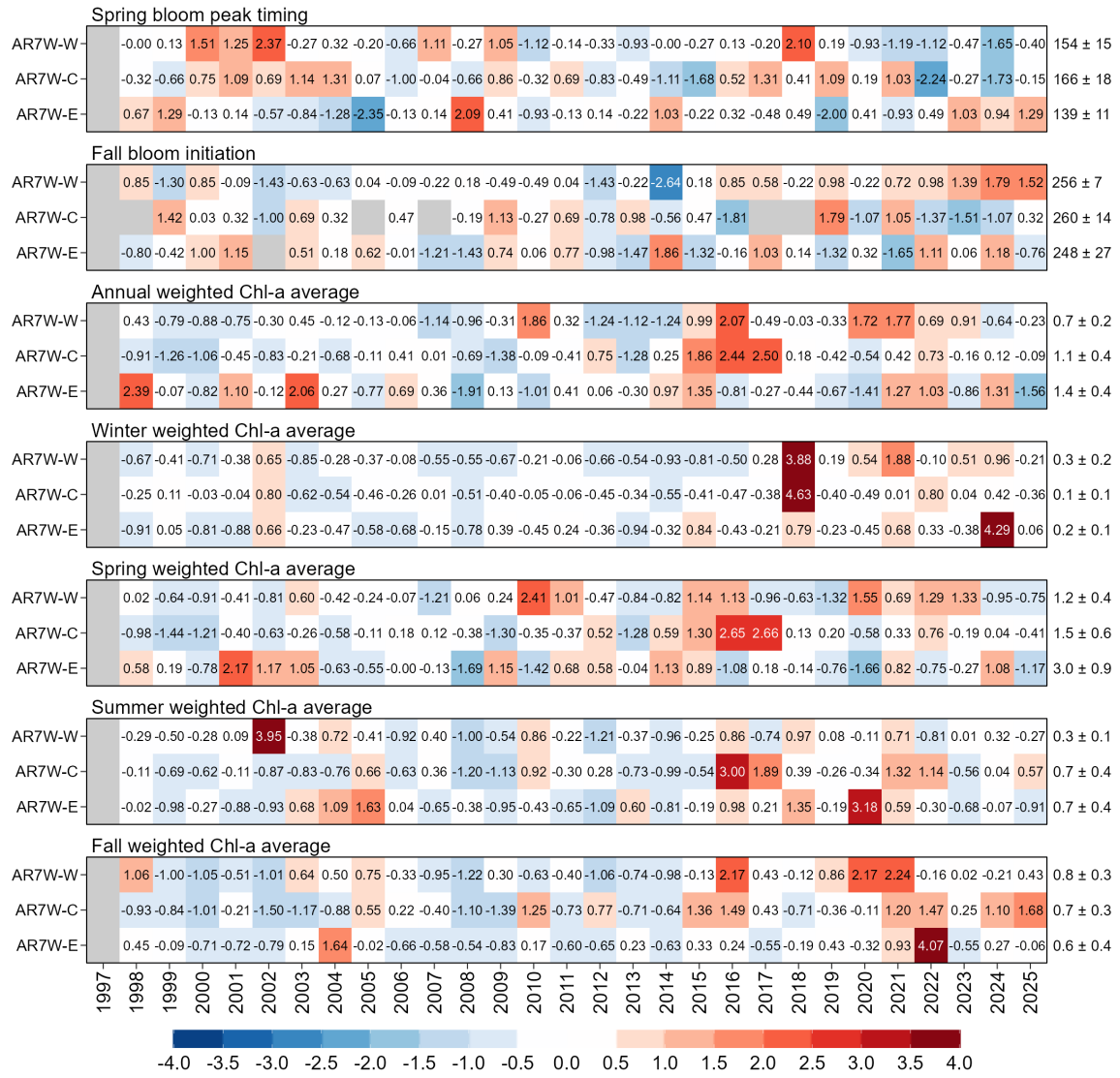


Figure 32. Scorecards for seasonal surface chl-a metrics derived from the OC-CCI multi satellite sensor product (timing is the day of year, and averages are measured in $mg\ m^{-3}$) from 1998 to 2025 for the AR7W-West (AR7W-W), AR7W-Central (AR7W-C), and AR7W-East (AR7W-E) polygons. Grey boxes indicate no data. Numbers within cells represent the annual standardized anomalies. Numbers on the right side indicate the mean values 1999–2025 (i.e., reference) for a given region as well as the standard deviation (i.e., mean ± standard deviation).

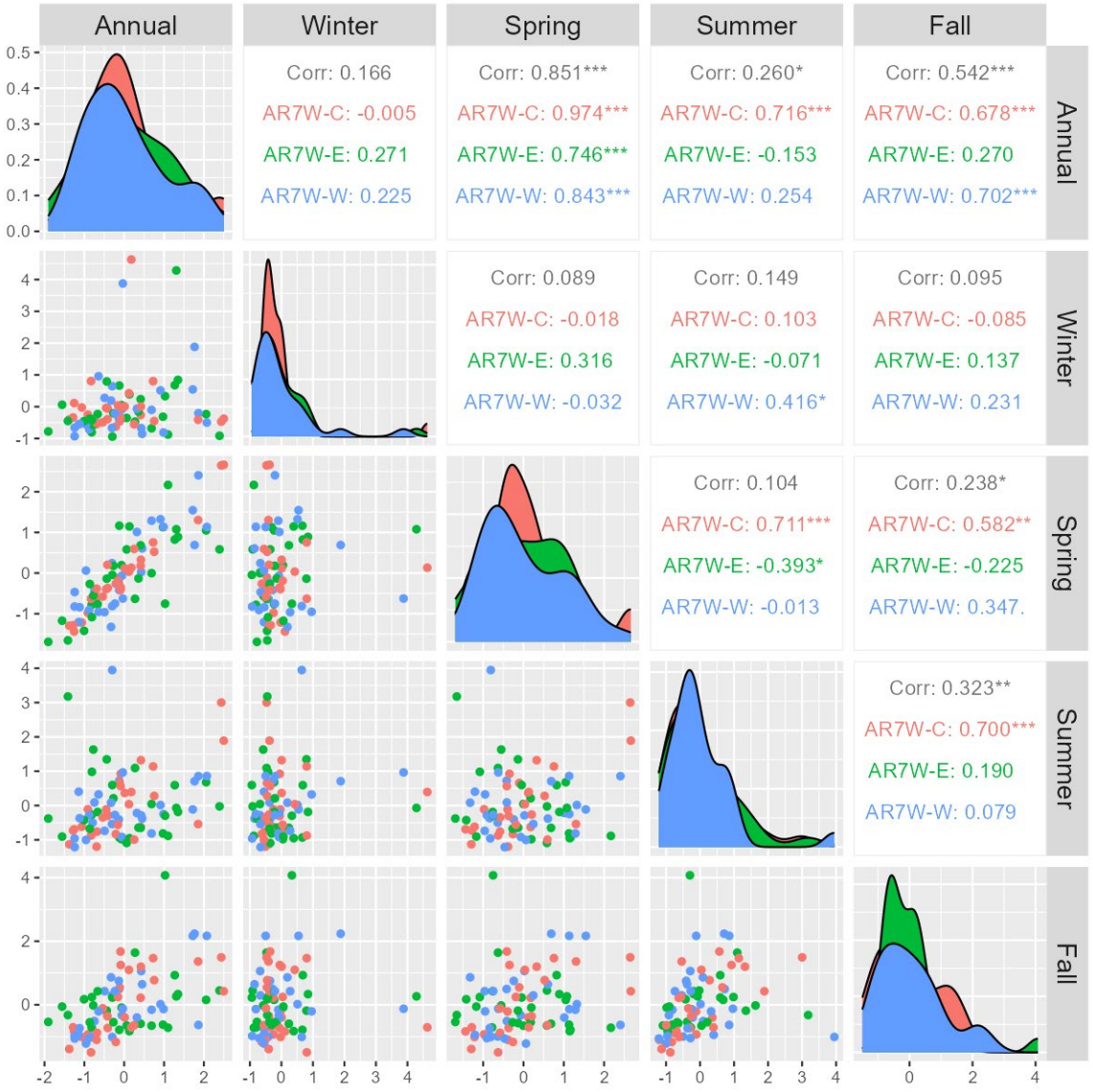


Figure 33. Scatterplot matrix showing the relationships between satellite-derived seasonal and annual chl-a average anomalies in each region of interest, indicated by color (red = AR7W-Central, green = AR7W-East, and blue = AR7W-West). Pearson's correlation coefficients for each relationship between seasonal anomalies are given in the top right corner of the triangle, with asterisks indicating their statistical significance level.

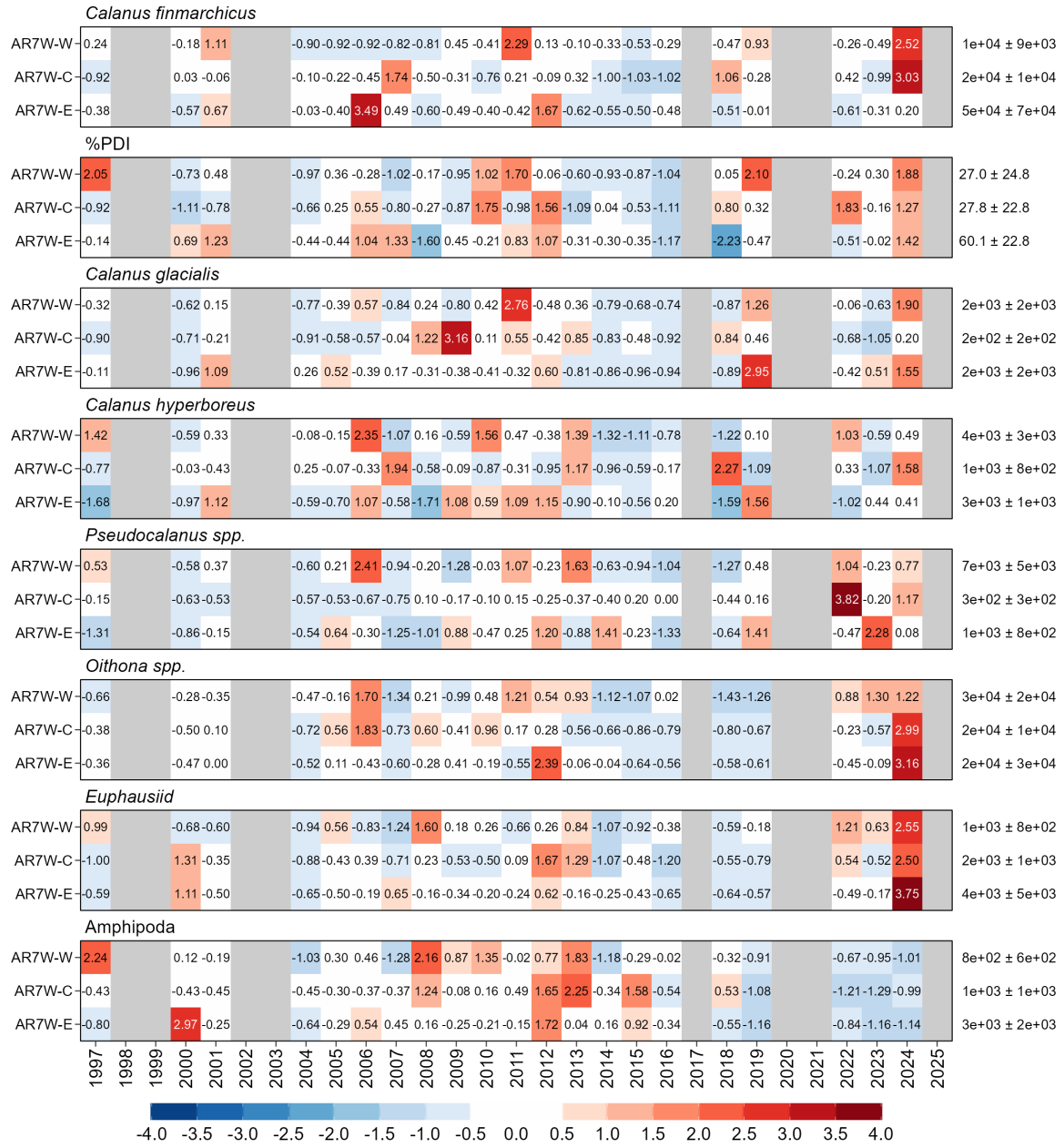


*Figure 34. Scorecards for mesozooplankton abundances from 1997 to 2025 for AR7W-West (AR7W-W), AR7W-Central (AR7W-C), and AR7W-East (AR7W-E) expressed as normalized anomalies (dimensionless) based on 1999–2025 reference period. The second panel from the top shows the Population Development Index (%PDI) calculated as the sum abundance of C. finmarchicus copepodite CI-CIII * 100 and divided by the sum of all developmental stages. Numbers on the right side indicate the mean values 1999–2020 (i.e., reference period) for a given region as well as the standard deviation (i.e., mean number of individuals per m^2 ± standard deviation). Grey cells indicate anomalies were omitted due to late sampling or that no sampling occurred that year due to lack of vessel (2017, 2021).*

9 APPENDIX

10 OCEAN COLOUR POLYGON SEASONS

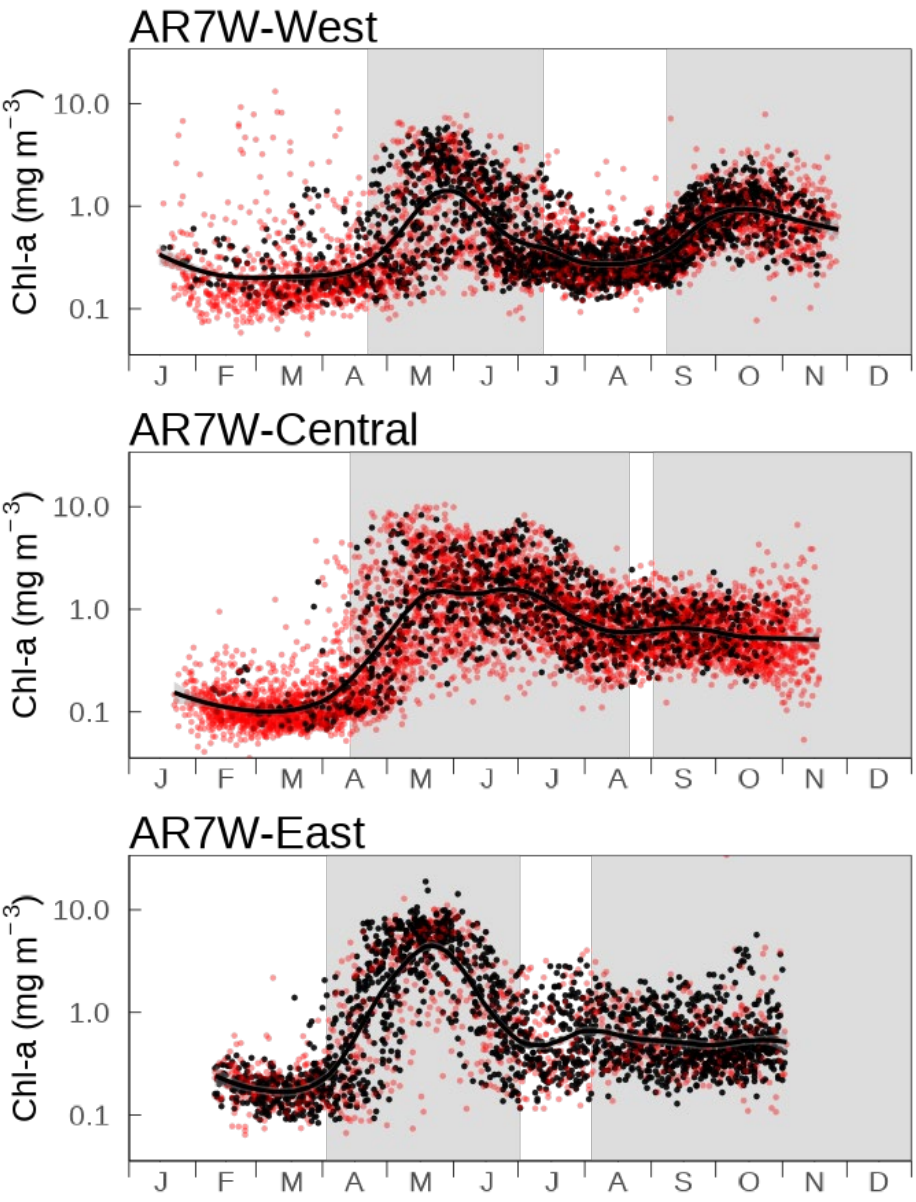


Figure 35. Time series of daily average concentrations within each Labrador Sea polygon over the climatological period (1999-2025). Grey shaded areas indicate the spring and fall bloom periods (i.e., region-specific 'seasons'). White areas indicate the winter and summer 'seasons'. Red circles corresponds to daily data coverage of less than 20% of a polygon. Days of the year marking the transition from winter to spring, spring to summer, and summer to fall are 112, 194, and 251 (AR7W-West), 104, 234, and 245 (AR7W-Central), and 93, 183, and 216 (AR7W-East).